UC Berkeley
UC Berkeley Electronic Theses and Dissertations

Title

TOMM40: Bridging mitochondrial and lipid metabolism

Permalink

https://escholarship.org/uc/item/92h8x4gf

Author

Yang, Neil Victor

Publication Date

2024

Peer reviewed|Thesis/dissertation

eScholarship.org Powered by the California Digital Library
University of California

“TOMM40: Bridging mitochondrial and lipid metabolism”

By

Neil Victor Yang

A dissertation submitted in partial satisfaction of the

requirements for the degree of

Doctor of Philosophy

in

Comparative Biochemistry

in the

Graduate Division

of the

University of California, Berkeley

Committee in Charge:

Professor Ronald Krauss, Co-Chair
Professor Andreas Stahl, Co-Chair
Professor Denis Titov
Professor Fenyong Liu

Summer 2024

Abstract

“TOMM40: Bridging mitochondrial and lipid metabolism”

By

Neil Victor Yang

Doctor of Philosophy in Comparative Biochemistry

University of California, Berkeley

Professor Ronald Krauss, Co-Chair

Professor Andreas Stahl, Co-Chair

Translocase of outer mitochondrial membrane 40 (TOMM40, aka TOM40) is the major channel-forming subunit of the translocase of outer mitochondrial membrane (TOM) complex that regulate mitochondrial function by importing nuclear-encoded proteins. TOMM40 is located at mitochondria-endoplasmic reticulum contact sites (MERCs), which play a key role in cellular signaling, with known effects on mitochondria bioenergetics and lipid synthesis. Furthermore, we have used RNA-seq to assess global transcriptional response to statin exposure in immortalized lymphoblastoid cell lines (LCLs) derived from participants in a clinical trial who were treated with 40mg/day of simvastatin for 6 weeks. Our previous studies using this model system identified a number of novel genes affecting cholesterol metabolism and *in vivo* statin LDL (low-density lipoprotein) cholesterol response, including TOMM40.

Statins are the drugs most commonly used for lowering plasma LDL cholesterol and cardiovascular disease risk. Although generally well tolerated, statins can induce myopathy, a major cause of non-adherence to treatment. Cellular studies have identified statin-induced myopathy to be associated with impaired mitochondrial function and morphology. In Chapter 2, we show that TOMM40 and TOMM22 play a key role in mediating statin-induced mitochondrial dysfunction as well as disruption of mitochondrial dynamics in skeletal myotubes. These findings suggest a novel mechanism by which adverse effects of statin treatment on mitochondrial dynamics that may contribute to the development of statin-induced myopathy are mediated by reduced *TOMM40* and *TOMM22* gene expression.

Beyond the mitochondria, we explore the role of TOMM40 on regulation of lipid metabolism via MERCs. Fundamentally, the gene encoding TOMM40 is adjacent to that for APOE, a protein with central functions in lipid and lipoprotein transport. Recent GWAS studies have shown that a number of SNPs in linkage disequilibrium between

these two genes are significantly associated with plasma lipid levels. While these associations have generally been attributed to *APOE*, no previous studies have addressed the possibility that TOMM40 has an independent effect on lipid metabolism. In Chapter 3, our investigation of molecular mechanisms underlying the effects of *TOMM40* knockdown on lipid metabolism has revealed a number of novel findings, including a key role for the LXR transcription factor due both to transcriptional upregulation and increased activation by oxysterols that are generated by mitochondria-induced reactive oxygen species. Interestingly, the increased LXR activity also results in reduced intracellular cholesterol via both upregulation of the membrane cholesterol transporter ABCA1 and increased production and secretion of oxysterol-derived cholic acid. Finally, and importantly, we have shown using a number of experimental approaches that the LXR-mediated effects described above result from disruption of mitochondria-ER contact sites (MERCs), where TOMM40 plays a key role, and that lipid droplet contact sites are consequently shifted from the ER to mitochondria.

Overall, these findings demonstrate TOMM40 plays a key role in connecting mitochondrial function and lipid metabolism.

TABLE OF CONTENTS

ABSTRACT……………………………………………………………………………………1

TABLE OF CONTENTS…………………………………………………………………..i

TABLE OF FIGURES………………………………………………………………………iv

DEDICATION………………………………………………………………………………vi

ACKNOWLEDGEMENTS………………………………………………………………...vii

CHAPTER 1: LITERATURE REVIEW ………………………………………………………1
    1.1 Cholesterol and Cardiovascular Disease Risk…………………………………...1
    1.2 Statin inhibit cholesterol synthesis via activation of the SREBF2 pathway……1
    1.3 Statin-associated Myopathy……………………………………………………….1
    1.4 Simvastatin treatment of LCLs decreases expression of TOMM40 and other genes encoding mitochondrial proteins……………………………………………..2
    1.5 *TOMM40-APOE* Connection…………………………………………………...2
    1.6 Mitochondrial Cholesterol……………………………………………………...3
    1.7 Mitochondria-ER Contact Sites…………………………………………………3
    1.8 Bridging mitochondria to cholesterol and lipid metabolism…………………4
    TRANSITION……………………………………………………………………………5

CHAPTER 2: TOMM40 rescues statin-impaired mitochondrial function, dynamics, and mitophagy via interaction with BCAP31 in skeletal myotubes……………………………..6
    2.1 Summary…………………………………………………………………………..7
    2.2 Introduction………………………………………………………………………7
    2.3 Results……………………………………………………………………………..8
        2.3.1 Simvastatin downregulates key subunits of the TOM complex in mammalian skeletal muscle cells…………………………………………...8
        2.3.2 *TOMM40* and *TOMM22* knockdown impair mitochondrial function in skeletal myotubes…………………………………………………………9
        2.3.3 *Tomm40* and *Tomm22* KD reduces cholesterol and CoQ levels in mitochondria of C2C12 myotubes *in vitro*…………………………………...9
        2.3.4 *TOMM40* and *TOMM22* KD promote mitochondrial fission and upregulate mitophagy in response to mitochondrial damage…………..10
        2.3.5 Overexpression of TOMM40 and BCAP31 rescue statin-induced mitochondrial dysfunction………………………………………………...11
        2.3.6 *TOMM40* and *TOMM22* rescue statin-induced mitochondrial fusion and fission events………………………………………………………...12
    2.4 Discussion & Conclusion…...……………………………………………………13
    2.5 Methods……………………………………………………………………………16
        2.5.1 Cell culture………………………………………………………………16

2.5.2 siRNA reverse transfections……16
2.5.3 Overexpression plasmids……17
2.5.4 Animal studies……17
2.5.5 Mitochondrial respiration measurements……17
2.5.6 Fluorescence quantification……18
2.5.7 Isolation of mitochondria by subcellular fractionation……18
2.5.8 Lipid extraction for LC-MS/MS……18
2.5.9 Measurement of CoQ_9 by LC-MS/MS lipidomics……19
2.5.10 Lipid extraction and intracellular cholesterol quantification……19
2.5.11 Sample preparation for electron microscopy……19
2.5.12 Transmission electron microscopy……20
2.5.13 Immunoblotting……20
2.5.14 RT-qPCR and mtDNA copy number……20
2.5.15 Statistical analysis……21
2.6 Figures……22
TRANSITION……41

CHAPTER 3: TOMM40 regulates hepatocellular and plasma lipid metabolism via an LXR-dependent pathway……42
3.1 Summary……43
3.2 Introduction……43
3.3 Results……44
3.3.1 Loss of hepatic *TOMM40* disrupts mitochondrial function and mitochondria-ER contact sites (MERCs)……44
3.3.2 *TOMM40* KD promotes production of oxysterols and upregulation of LXR gene targets……44
3.3.3 *TOMM40* KD increases LDLR gene expression and receptor-mediated LDL hepatic uptake……45
3.3.4 Loss of *TOMM40* expression promotes the classic bile acid synthesis pathway, while inhibiting the alternative pathway via STAR……46
3.3.5 Effects of *TOMM40* KD on hepatic triglyceride metabolism……47
3.3.6 Plasma cholesterol and triglyceride levels are reduced in AAV8-*Tomm40* shRNA C57BL/6J mice……48
3.3.7 *TOMM40* KD induces lipid droplet accumulation and metabolic-dysfunction associated steatotic liver disease (MASLD)……48
3.4 Discussion & Conclusion……49
3.5 Methods……53
3.5.1 Mice studies……53
3.5.2 Primary mouse hepatocytes……53
3.5.3 HepG2 cell culture……53
3.5.4 Mitochondrial respiration measurements……54
3.5.5 Mitochondrial assays……54
3.5.6 Calcium imaging……54
3.5.7 TEM sample preparation……54

3.5.8 Transmission electron microscopy……………………………………55
3.5.9 Volume imaging processing for liver tissue…………………………55
3.5.10 Focused ion beam scanning electron microscopy (FIB-SEM) imaging………………………………………………………………………55
3.5.11 Image processing…………………………………………………..55
3.5.12 Enzyme-linked immunosorbent assay (ELISA)…………………….56
3.5.13 Fluorescence imaging……………………………………………..56
3.5.14 Lipid extraction and quantification…………………………………57
3.5.15 Isolation of mitochondria and mitochondria-associated membranes………………………………………………………………57
3.5.16 Immunoblotting……………………………………………………57
3.5.17 RT-qPCR…………………………………………………………...58
3.5.18 Dual luciferase reporter assay……………………………………..58
3.5.19 Plasma lipid and lipoprotein analyses………………………………59
3.5.20 Histological analyses……………………………………………….59
3.5.21 Statistical analysis…………………………………………………...59
3.6 Figures……………………………………………………………………...60

CHAPTER 4: FINAL CONCLUSION……………………………..……………………...82

REFERENCES……………………......……………………………………………………84

TABLE OF FIGURES

Figure 2-0. Graphical Abstract……………………………………………………………...5
Figure 2-1. Simvastatin downregulates *TOMM40* and *TOMM22* in both C2C12 and hSkMC skeletal muscle……………………………………………………………………….21
Figure 2-2. *TOMM40* and *TOMM22* knock-down decrease mitochondrial oxygen consumption rate and promote mitochondrial superoxide production……………….22
Figure 2-3. *Tomm40* and *Tomm22* regulate mitochondrial cholesterol content and CoQ levels in C2C12 myotubes……………………………………………………………..24
Figure 2-4. *TOMM40* and *TOMM22* knock-down, singly and in combination, impair mitochondrial dynamics in skeletal myotubes…………………………………………….26
Figure 2-5. *TOMM40* and *TOMM22* knock-down, singly and in combination, promote mitochondrial damage and mitophagy in skeletal muscle *in vitro* and *in vivo*………..28
Figure 2-6. *TOMM40* and *BCAP31* overexpression rescues mitochondrial respiration, ATP production, and proton leak after simvastatin treatment of skeletal muscle cells……………………………………………………………………………………...30
Figure 2-7. Overexpressing *TOMM40* and *TOMM22, singly and in combination,* suppresses statin-induced mitochondrial fission and promotes fusion in skeletal muscle cells……………………………………………………………………………………32
Figure 2-8. Overexpression of *TOMM40* and *TOMM22*, but not *TOMM20*, rescues simvastatin-induced mitophagy leading to reduced mitochondrial damage………...34
Figure 2-S1. Simvastatin treatment of C2C12 myotubes upregulates *Ldlr* and *Hmgcr* mRNA transcripts in a dose-dependent manner…………………………………………35
Figure 2-S2. Dose-dependent cell apoptosis identified in C2C12 myotubes………...35
Figure S3. Effects of *Tomm40* and *Tomm22* knockdown on CoQ levels in C2C12 whole cell lysates……………………………………………………………………...36
Figure 2-S4. Simvastatin treatment further decreases CoQ levels in *Tomm40* and *Tomm22* KD C2C12 mitochondria………………………………………………………….36
Figure 2-S5. Female C57BL/6J mice injected with AAV8-*Tomm40* shRNA do not show knockdown of *Tomm40* or differences in mitochondrial number and morphology, compared to scrambled shRNA control……………………………………………………37
Figure 2-S6. *BCAP31* and *TOMM40* or *TOMM22* overexpression does not rescue intracellular cholesterol levels in simvastatin-treated hSkMC myotubes………………38
Figure 2-S7. Overexpression of *BCAP31* recues *FIS1* gene expression in simvastatin-treated skeletal myotubes………………………………………………………………38
Figure 2-S8. *TOMM40* knockdown downregulates *BCAP31* gene expression in hSkMC myotubes…………………………………………………………………………………39
Figure 3-0. Graphical Abstract…………………………………………………………….40
Figure 3-1. TOMM40 is essential for maintaining mitochondrial function and MERCs in hepatocytes…………………………………………………………………………………58
Figure 3-2. *TOMM40* KD upregulates LXRB and downstream gene targets by promoting oxysterol production……………………………………………………………60

Figure 3-3. *TOMM40* KD promotes LDL uptake via an LXR-mediated pathway………62
Figure 3-4. *TOMM40* KD in hepatocytes promotes classic bile acid synthesis pathway while inhibiting alternative pathway via interaction with STAR at MERCs……………...64
Figure 3-5. *TOMM40* KD promotes VLDL uptake and triglyceride accumulation via LDLR upregulation……………………………………………………………………66
Figure 3-6. AAV8-T*omm40* shRNA injected C57BL/6J mice show reduced plasma cholesterol and triglyceride levels………………………………………………………68
Figure 3-7. *TOMM40/Tomm40* KD induces lipid droplet accumulation and hepatic steatosis *in vivo*……………………………………………………………………...70
Figure 3-S1. LXRA and LXRB isoforms reciprocally maintain LXR expression and regulate downstream gene targets…………………………………………………………………..72
Figure 3-S2. *MFN2* KD does not affect enzymatic-derived oxysterols in HepG2 cells………...72
Figure 3-S3. *TOMM40* KD does not affects *SREBF2* or *HMGCR* mRNA transcript levels in HepG2 cells……………………………………………………………………………………...73
Figure 3-S4. *MFN2* KD reduces 27-OHC levels in HepG2 cells………………………………..73
Figure 3-S5. Body weight and food intake measurements of AAV8-*Tomm40* shRNA C57BL/6J mice………………………………………………………………………………………………74
Figure 3-S6. Analysis of distance (nm) between MERCs in AAV8-*Tomm40* shRNA C57BL/6J female mice liver……………………………………………………………………………..75
Figure 3-S7. Measurements of lipoprotein particle concentrations on mouse plasma………..76
Figure 3-S8. Representative Oil Red O and Hematoxylin-Eosin stained liver samples of female mice………………………………………………………………………………………………77
Figure 3-S9. Analysis of TEM micrographs indicating no differences in lipid droplet-ER and lipid-droplet mitochondria contact sites in female mice…………………………………………..77
Figure 3-S10. Quantification of *Bscl2*/BSCL2 expression in mouse hepatic tissues…………...78
Figure 3-S11. mRNA transcript levels of *BSCL2* in HepG2 cells…………………………………..79
Figure 3-S12. *CYP27A1* mRNA transcript levels…………………………………………………79

DEDICATION

This doctoral thesis serves as a testament to God's goodness and love, for only through His guidance and providence, has He made this all possible.

Special thanks to my academic mentors, Ron Krauss and Beth Theusch. Beth, thank you for your candidness and personable nature. Through your meticulousness and attention to statistical details, you have taught me to do science the right way. Ron, thank you for all that you have taught and invested in me, not only in scientific but also in personal development. By example I have learnt perseverance and humility are key traits of a scientist, as you once said, "you can never know everything". I also thank the Krauss lab for being the best team I can ever ask for! Sarah, Joe, Justin Chao, Tommy, Jacob, Justin Kim, and Andy, thank you for all the memories and help!

To my Vinewood community, thank you for being my family away from home. I will always treasure the friendships and memories. Honorary mention to those who have encouraged and supported me on this journey: Esther and the BOTAs, Vince, Riley and the Canto Club, and Theo & Dorothy. You guys are the BEST.

To my family at home, Mom, Dad, Gorgor, thank you for being by my side when times were tough. First year was definitely not easy, so thank you for the weekly pep talks and the wisdom you always pass onto us. Thank you for teaching me and Gorgor to always seek after God's own heart in everything we do.

Lastly, I thank God for walking alongside me through all these years of my life. I thank You for never giving up on me and showering me with infinite grace time after time. Thank you for allowing me to witness and discover more of you through what you've created and for bringing me to Berkeley so that I can grow in my career, character, and faith.

"[10] And the God of all grace, who called you to his eternal glory in Christ, after you have suffered a little while, will himself restore you and make you strong, firm and steadfast. [11] To him be the power for ever and ever. Amen."

- 1 Peter 5:10

ACKNOWLEDGEMENTS

Chapter 2 adapted with permission from bioRxiv,

bioRxiv 2023.06.24.546411; doi: https://doi.org/10.1101/2023.06.24.546411

TOMM40 and TOMM22 of the Translocase Outer Mitochondrial Membrane Complex rescue statin-impaired mitochondrial dynamics, morphology, and mitophagy in skeletal myotubes

Neil V Yang, Sean Rogers, Rachel Guerra, David J Pagliarini, Elizabeth Theusch, Ronald M Krauss

Chapter 3 adapted with permission from bioRxiv,

bioRxiv 2024.06.27.600910; doi: https://doi.org/10.1101/2024.06.27.600910

TOMM40 regulates hepatocellular and plasma lipid metabolism via an LXR-dependent pathway

Neil V Yang, Justin Y Chao, Kelly A Garton, Tommy Tran, Sarah M King, Joseph Orr, Jacob H Oei, Alexandra Crawford, Misun Kang, Reena Zalpuri, Danielle Jorgens, Pranav Konchadi, John S Chorba, Elizabeth Theusch, Ronald M Krauss

CHAPTER 1: LITERATURE REVIEW

1.1 Cholesterol and Cardiovascular Disease Risk

Cardiovascular diseases (CVDs) are the leading causes of death worldwide[1]. Lipids and lipoproteins are a major risk factor in the development of CVDs. In particular, plasma low density lipoprotein cholesterol (LDL-C) increases risk of CVDs by development of atherosclerotic plaques, as discovered by the Framingham Heart Study[2]. Thus, reducing plasma cholesterol levels is critical in preventing atherosclerosis and coronary artery disease. From Brown and Goldstein's work, the LDL receptor (LDLR) was discovered in the liver to selectively mediate the uptake of lipoproteins including LDL-C, by recognizing apolipoproteins B100 (ApoB100) and E (ApoE)[3]. By internalization of LDL-C, lipoproteins are degraded by lysosomes and the cholesterol is released. Cholesterol plays a key role in maintaining cell membrane integrity, fluidity, and regulation of signaling pathways[4]. At the cellular level, cholesterol homeostasis is maintained via cholesterol esterification to promote formation of lipid droplets (LDs) for storage, released intracellularly via cholesterol efflux or is synthesized into bile acids and steroid hormones[5]. In addition to uptake of cholesterol via LDLR, cholesterol can also be synthesized via the mevalonate pathway in the liver.

1.2 Statins inhibit cholesterol synthesis via activation of the SREBF2 pathway

Statins are the most commonly prescribed drugs used for reducing plasma cholesterol levels and CVD risk. They act by inhibiting 3-hydroxy-3-methylglutaryl coenzyme A (HMGC-CoA) reductase (HMGCR), the rate limiting step of cholesterol biosynthesis[6]. In turn, statin-induced cholesterol depletion results in the translocation of SREBF2 (aka SREBP2) from the ER into the nucleus. This results in the transcription of multiple SRE-regulated genes, including LDLR, HMGCR, and PCSK9 (proprotein convertase subtilisin/kexin type 9)[7]. Thus, the effects of statin on blood cholesterol levels are two-fold by: inhibition of the mevalonate synthesis pathway and upregulation of LDLR transcription.

1.3 Statin-associated Myopathy

Although statins are highly effective drugs and are generally well-tolerated, they can have adverse side effects, the most common being statin-associated muscle symptoms (SAMS)[8]. Clinical and observational studies have reported 10-30% of statin users to experience SAMS[9,10]. These skeletal muscle-associated, dose-dependent adverse reactions range from myopathy, myalgia, and myositis to rhabdomyolysis.

Disruption of mitochondrial function by statins has been proposed as a likely mechanism contributing to statin-induced myopathy[11]. Many studies have shown phenotypic effects of statins in muscle mitochondria in vitro and in vivo, including altered levels of electron transport chain proteins and generators of reactive oxygen species (ROS)[12]. Specifically, increased ROS, decreased peroxisome proliferator-activated receptor gamma co-activator (PGC-1α), altered protein prenylation[13], decreased Coenzyme Q10 (CoQ10)[14], decreased intracellular ATP[15], decreased oxygen consumption[16], and increased fragmentation of mtDNA[17], have been observed in various in vitro skeletal muscle cell, animal in vivo models, and clinical studies. However, little is known of the molecular basis for these statin effects.

1.4 Simvastatin treatment of LCLs decreases expression of TOMM40 and other genes encoding mitochondrial proteins

In a recent study utilizing genome-wide RNA-seq analysis[18] our lab demonstrated that exposure of a panel of 426 subject-derived LCLs to simvastatin (2µM) significantly downregulated expression of multiple genes encoding mitochondrial proteins, including several major subunits of the translocase of the outer membrane (TOM) complex: TOMM40, TOMM22, and TOMM20[19]. Consistent with this, simvastatin has been reported to reduce TOMM40 gene expression by 50% in primary human myotubes[20]. TOMM40 is essential for maintaining mitochondrial function through its role in transporting precursor proteins into the mitochondria[19]. Loss or knockdown of TOMM40 interferes with uptake of mitochondria-targeted proteins, disrupts the mitochondrial membrane potential, and induces mitochondrial stress responses[21,22]. Thus, with this finding of statin-induced suppression of TOMM40, in Chapter 2 we explored whether TOMM40 is a key mediator in statin-induced myotoxicity in skeletal muscle.

1.5 *TOMM40-APOE* Connection

Within the chromosome 19 locus, TOMM40 is located within a cluster of genes that regulates lipid metabolism. Of these, APOE, a key regulator of lipid transport, is directly downstream of TOMM40. APOE acts as a ligand for LDLR to promote the import of LDL, VLDL (very-low density lipoprotein), and IDL (intermediate-density lipoprotein) cholesterol containing lipoproteins into the liver. More importantly, multiple genome-wide association studies (GWAS) have reported single-nucleotide polymorphisms (SNPs) within these two genes to be in strong linkage disequilibrium, in relation to plasma LDL-C[23,24]. In the context of Alzheimer's disease (AD), populations with SNPs in both TOMM40 and APOE has been identified to be at greater risk of developing ADs, as well as carrying the APOE4 allele, a proxy for ADs[23,25]. Albeit the genetic association between TOMM40 and APOE, little is known regarding the involvement of TOMM40 in cellular cholesterol homeostasis, and, more generally, the impact of mitochondrial proteins on cholesterol metabolism. In chapter 3, our data supports strong evidence of a molecular association between TOMM40 and APOE in regulating cholesterol and lipid metabolism in the liver, via mitochondria-ER contact sites (MERCs).

1.6 Mitochondrial Cholesterol

Mitochondrial cholesterol represents about 2-4% of the total cholesterol pool in cells, yet fluctuations in mitochondrial cholesterol results in hepatic steatosis, carcinogenesis, and neurodegeneration[26]. This is largely due to the need for mitochondrial cholesterol in maintaining the mitochondrial membranes and assembly of the electron transport chain complexes, where cholesterol loading in both outer and inner mitochondrial membranes has been shown to not only alter mitochondrial membrane and morphology, but also suppress mitochondrial respiration by disrupting the assembly of complex 1 in the electron transport chain[27,28]. Additionally, mitochondrial cholesterol is essential for the synthesis of oxysterols, specifically 27-hydroxycholesterol, steroid hormones, and hepatic bile acids generated via the alternative bile acid synthesis pathway[29-31].

The transport of mitochondrial cholesterol from the ER, where it is synthesized, to the mitochondrial interior occurs through non-vesicular transport by steroidogenic acute regulatory protein 1 (STARD1, also known as STAR)[32]. This family of proteins transports cholesterol, as well as oxysterols, phospholipids, sphingolipids, and fatty acids. Once cholesterol is delivered through the inner mitochondrial membrane, it is converted for use into oxysterols and steroid hormone precursors via cytochrome P450 family of enzymes[33]. Thus, suppressing STAR prevents cholesterol trafficking into the mitochondria at MERCs, resulting in the development of congenital adrenal hyperplasia and hepatic steatosis in vivo. Global deletion of all STAR genes is lethal in mice and die after 7-10 days post-birth[34].

1.7 Mitochondria-ER Contact Sites

Increasing evidence indicates that mitochondria-ER contact sites (MERCs) serve an important role in cellular signaling, including cholesterol trafficking, lipid biogenesis, mitochondrial fission, calcium storage, and induction of autophagy within hepatocytes and neuronal cells[35]. In addition, MERCs are a hot spot for the transfer of stress signals between the ER and mitochondria, thus modulating ER stress[36]. MERCs are defined as tight contacts with a distance shorter than 50 nm between the ER and the mitochondria, where 10-15% of all mitochondrial membranes are in contact with the ER[37.38]. It has been shown that genetic manipulation of proteins at MERCs, including MFN2, disrupts both mitochondrial and ER homeostasis and induces stress in both organelles. At these MERCs, TOMM40 has been shown to interact with key regulators of mitochondrial function[39], cholesterol transport[33,40], and calcium signaling[41-43] on the ER membrane. Most notably, these include ER membrane proteins such as B cell receptor-associated protein 31 (BAP31)[39]. Knockout of this gene in U2OS cells (bone osteosarcoma) disrupts the BAP31-TOMM40 complex and decreases mitochondrial complex I activity, mitochondria oxygen consumption, and ATP production, and this has also been shown to elicit ER stress[44]. As mentioned previously, STARD1 (aka steroidogenic acute regulatory protein) interacts with TOMM40 at MERCs to promote cholesterol trafficking into the mitochondria[45]. Deletion of this gene results in lethal adrenal lipoid hyperplasia in mice as well as increased cholesterol saturation at the ER membrane, triggering the UPR stress response[34,46]. TOMM40 also interacts with voltage-dependent anion channel 1 (VDAC1) located on the outer mitochondrial membrane at MERCs to regulate Ca^{2+} influx into the mitochondria. VDAC1 deficiency results in the build-up of Ca^{2+} at the MERCs, which induces ROS in murine neuronal and liver cells[36,39,40]. Additionally, it has been shown that increased VDAC1 expression correlated with increased MERCs in hippocampal neurons[47]. Other major subunits of the TOM complex, including TOMM22, have been shown to couple with Bcl-2 associated X-protein (BAX) at MERCs to regulate ER stress-mediated apoptosis of cancer cells[48], as well as mitofusin-1 (Mfn1), a key tethering protein that maintains mitochondria-ER communication[49]. These findings suggest that TOMM40, in conjunction with other subunits of the TOM complex associated with ER surface and outer mitochondrial membrane proteins at MERCs, may play a key role in regulating lipid metabolism directly and indirectly via mitochondrial function & dynamics, ER stress, and cholesterol & lipid trafficking between the mitochondria and ER.

1.8 Bridging mitochondria to cholesterol and lipid metabolism

With surmounting genetic evidence of a linkage between TOMM40, a vital mitochondrial protein, and APOE, a key cholesterol modulator, in addition to our previous LCLs data showing its downregulation upon statin treatment, suggests possible involvement of TOMM40 in cholesterol and lipid metabolic pathways. Recent studies have identified mitochondrial abnormalities to be associated with cardiovascular diseases including metabolic-dysfunction associated steatotic liver disease (MASLD) and atherosclerosis[50]. These phenotypes include impaired mitochondrial morphology, disrupted mitochondrial membrane potential, oxidative stress, and cellular senescence[51,52]. In addition, it has been well documented that defect in fatty acid oxidation from the mitochondria underutilizing fat as ATP, leads to mitochondrial hepatopathies[53]. More recently, mitochondrial dysfunction has been shown to increase lipid droplet accumulation in enterocytes and impair plasma lipid levels[53]. With these new evidence of a link between mitochondrial and lipid metabolism, this thesis aims to further explore the molecular association between mitochondrial function and cholesterol metabolism through the role of TOMM40 in skeletal muscle and the liver. In chapter 2, we investigate TOMM40 as a mediator of statin-induced myotoxicity in skeletal muscle, and in chapter 3, we seek to determine the role of TOMM40 in regulating cholesterol and lipid metabolism in the liver.

TRANSITION

Our previous LCLs data from the Cholesterol and Pharmacogenetics (CAP) trial showed statin treatment to downregulate a subset of mitochondria protein-encoding genes,. Among these genes, *TOMM40* and *TOMM22* were most significantly downregulated by simvastatin treatment. This led us to hypothesize TOMM40, and TOMM22, of the TOM complex may play a key role in mediating statin-associated myopathy.

Supported by previous findings that have shown knock-down of TOMM40 in skeletal muscle induced mitochondrial dysfunction, we wanted to first determine whether TOMM40 and TOMM22 are key mediators of statin-induced mitochondrial dysfunction. In Chapter 2, we confirmed simvastatin to significantly downregulate *TOMM40* and *TOMM22* in mouse and human skeletal myotubes and compared their mitochondrial phenotypes to *TOMM40* and *TOMM22* knock-down, singly and in combination. Lastly, we showed that overexpressing TOMM40 or TOMM22 were both able to rescue the disruption in mitochondrial dynamics due to simvastatin treatment. However, in rescuing statin-induced mitochondrial dysfunction, TOMM40 required BCAP31, a binding partner at MERCs, thus highlighting the importance of these mitochondria-ER contact sites which will be further explored in Chapter 3.

CHAPTER 2: TOMM40 rescues statin-impaired mitochondrial function, dynamics, and mitophagy via interaction with BCAP31 in skeletal myotubes

Neil V Yang*, Sean Rogers, Rachel Guerra, Justin Y Chao, David J Pagliarini, Elizabeth Theusch, Ronald M Krauss

Published in bioRxiv, doi: https://doi.org/10.1101/2023.06.24.546411

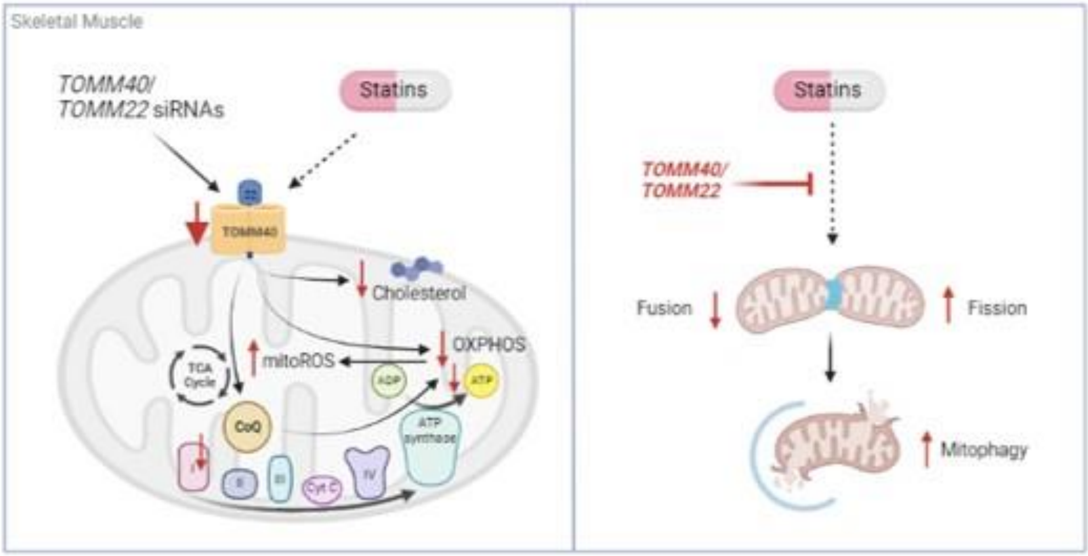

Figure 2-0. Graphical Abstract

2.1 Summary

Statins are the drugs most commonly used for lowering plasma low-density lipoprotein (LDL) cholesterol levels and reducing cardiovascular disease risk. Although generally well tolerated, statins can induce myopathy, a major cause of non-adherence to treatment. Impaired mitochondrial function has been implicated in the development of statin-induced myopathy, but the underlying mechanism remains unclear. We have shown that simvastatin downregulates transcription of *TOMM40* and *TOMM22*, genes that encode major subunits of the translocase of outer mitochondrial membrane (TOM) complex. Mitochondrial effects of knockdown of *TOMM40* and *TOMM22* in mouse C2C12 and primary human skeletal cell myotubes included impaired oxidative function, increased superoxide production, reduced cholesterol and CoQ levels, and disruption of mitochondrial dynamics and morphology, as well as increased mitophagy, with similar effects resulting from simvastatin exposure. Overexpression of *TOMM40* and *TOMM22* in simvastatin-treated mouse and human skeletal muscle cells rescued effects on mitochondrial dynamics and morphology, but not oxidative function or cholesterol and CoQ levels. However, overexpression of both *TOMM40* and *BCAP31*, a gene encoding a mitochondria-associated membrane protein that binds with TOMM40 and whose transcription is also suppressed by statin, resulted in the rescue of mitochondrial function independent of intracellular cholesterol content. These results show that TOMM40 and BCAP31 have key roles in maintaining both mitochondrial dynamics and function and indicate that their downregulation by statin treatment results in mitochondrial effects that may contribute to statin-induced myopathy.

2.2 Introduction

Statins, the most widely used class of drugs for reducing plasma LDL-cholesterol levels and cardiovascular disease risk, act by inhibiting 3-hydroxy-3-methyglutaryl coenzyme A reductase (HMGCR), the rate-limiting enzyme for cholesterol synthesis[1,54]. Although statins are highly effective and generally well-tolerated, they can have adverse side effects, the most common being statin-associated muscle symptoms (SAMS)[8,10] ranging from myalgia and myositis to rhabdomyolysis[55]. Among the currently used statins, simvastatin has been associated with the greatest incidence of SAMS[9].

Disruption of mitochondrial function has been proposed as a major mechanism contributing to SAMS[11]. Effects of statins on skeletal muscle mitochondria phenotypes have been demonstrated in cellular, animal, and clinical studies[56,57]. These include increased reactive oxygen species (ROS)[12], decreased mitochondrial biogenesis[13], altered protein prenylation, decreased intracellular ATP levels[15,58], altered electron transport chain protein expression, increased fragmentation of mtDNA[17], and elevated plasma creatine kinase (CK) levels[59]. Additionally, statin-induced inhibition of synthesis of coenzyme Q (CoQ_{10}), an essential cofactor of the electron transport chain, has been proposed as a major contributing factor to skeletal muscle mitochondrial dysfunction[14]. Despite these findings, little is known of the molecular basis for these statin effects.

Recently, Grunwald et al. reported that simvastatin exposure of myotubes derived from primary human myoblasts resulted in a significant 50% reduction in expression of *TOMM40* and *TOMM22*[20], two broadly expressed and highly conserved genes encoding components of the translocase of the outer mitochondrial membrane (TOM) complex[19]. We have observed a similar effect of simvastatin in a panel of human lymphoblastoid cell lines[18]. The mammalian TOM complex consists of 7 subunits that work together to recognize and import proteins from the cytoplasm into the mitochondrial interior to maintain mitochondrial function[60,61] (**Fig. 2-1A**). Among these subunits, TOMM40 is the main channel-forming subunit that is stably associated with TOMM22, the central receptor of the complex[62]. Together, they are actively involved in protein translocation across the mitochondrial outer membrane[63]. In addition, TOMM40 is known to interact with several ER membrane proteins at mitochondria-ER contact sites (MERCs) including B cell receptor-associated protein 31 (BCAP31) which has been shown to regulate cell death and crosstalk signaling between ER and mitochondria[33,39], while TOMM22 binds with PINK1 for eliminating damaged mitochondria via mitophagy[64].

In the present study, we have performed detailed mitochondrial phenotyping to compare the effects of *TOMM40* and *TOMM22* knockdown with the effects of simvastatin treatment in two mammalian skeletal muscle cell models – mouse C2C12 cells, which are known to display cellular phenotypes with statin treatment similar to those seen with statin-induced myotoxicity in humans[65], and primary human skeletal muscle cells (hSkMC). We also tested the role of *TOMM40* and *TOMM22* downregulation in mediating statin's mitochondrial effects by determining whether these effects were rescued by overexpressing these genes. Finally, we showed that transcription of *BCAP31* is reduced by both statin treatment and *TOMM40* knockdown, and therefore tested whether reduced *TOMM40* expression may play a role in mediating mitochondrial effects of statin in skeletal muscle cells.

2.3 Results

2.3.1 Simvastatin downregulates key subunits of the TOM complex in mammalian skeletal muscle cells

We first aimed to confirm previous findings in primary human myotubes[63] that expression of *TOMM40* and *TOMM22* are downregulated by simvastatin exposure. Differentiated C2C12 and primary hSkMC myotubes were treated with 2 μM simvastatin for 24 hrs. This dose was chosen based on simvastatin dose response experiments that showed significant induction of *Hmgcr* and *Ldlr* mRNA at 2 μM in C2C12 cells (**Fig. 2-S1**). Additionally, we performed a simvastatin dose response experiment in C2C12 cells to assess apoptosis using EarlyTox Caspase-3/7 and found no significant increase with simvastatin 2 μM vs. baseline **(Fig. 2-S2**). In both cell types, mRNA transcript levels of *TOMM40* and *TOMM22* were significantly reduced by exposure to 2 μM simvastatin as assessed by qRT-PCR **(Fig. 2-1B, C).** Transcript levels of two other subunits of the TOM complex, *Tomm20* and *Tomm5*, were also significantly reduced by simvastatin in C2C12 myotubes but not primary hSkMC myotubes **(Fig. 2-1B, C).** These results confirm and extend evidence that simvastatin downregulates expression of the major subunits of the TOM complex.

2.3.2 *TOMM40* and *TOMM22* knockdown impair mitochondrial function in skeletal myotubes

We next sought to assess the potential role of *TOMM40* and *TOMM22* downregulation by statin in mediating mitochondrial dysfunction by studying the effects of *TOMM40* and *TOMM22* knockdown (KD) in C2C12 and hSkMC myotubes. KD of *Tomm40* and *Tomm22* singly and in combination was performed by a two-step siRNA transfection (**Fig. 2-2A**), resulting in greater than ~80% knockdown efficiency (**Fig. 2-2B**). In both C2C12 and hSkMC myotubes, basal and maximal oxygen consumption rate (OCR), as well as ATP production, were significantly reduced by each condition compared with a non-targeting control (NTC), indicating impaired electron transport chain and mitochondrial function (**Fig. 2-2C-F**).

To confirm a decrease in mitochondrial respiration due to suppression of *TOMM40* and *TOMM22* gene expression, we measured mitochondrial superoxide (mitochondrial reactive oxygen species, a.k.a. mitoROS) production using a fluorescence indicator (MitoSOX™) in C2C12 myotubes. This showed increased mitochondrial superoxide production in C2C12 cells transfected with both *Tomm40* and *Tomm22* siRNAs, compared to NTC (**Fig. 2-2G**). Though there was an increased trend observed in cells transfected with *Tomm40* siRNA individually (p=0.171), no significant differences were observed in *Tomm22* KD cells alone. These results demonstrate that KD of either *TOMM40* or *TOMM22* in skeletal myotubes impairs mitochondrial respiration and that their combined KD promotes the generation of mitoROS.

2.3.3 *Tomm40* and *Tomm22* KD reduce cholesterol and CoQ levels in mitochondria of C2C12 myotubes *in vitro*

Since mitochondria require cholesterol for maintenance of membrane integrity and proper respiratory function[66], we tested whether suppression of *Tomm40* and *Tomm22* expression reduces mitochondrial cholesterol content, and if such an effect contributes to impaired mitochondrial respiration. Consistent with our hypothesis, a reduction in mitochondrial cholesterol content was observed in both *Tomm40* and *Tomm22* siRNA-transfected cells, singly and in combination, compared to NTC (**Fig. 2-3B**). To assess whether reduced cholesterol alone is responsible for the disruption of mitochondrial function by *Tomm40* and *Tomm22* KD, we performed a cholesterol addback experiment. The addition of LDL isolated from human plasma rescued mitochondrial cholesterol content of *Tomm22* KD but not *Tomm40* KD myotubes (**Fig. 2-3C, D**). However, cholesterol repletion in *Tomm*22 KD myotubes did not restore reduced mitochondrial ATP production and basal respiration (**Fig. 2-3E, F**).

Given that CoQ, a product of the CoQ biosynthesis pathway, plays a central role in the mitochondrial electron transport chain, we next tested the effects of *Tomm40* and *Tomm22* KD on mitochondrial CoQ levels. Since mice, unlike humans, predominantly synthesize CoQ_9 (9 prenyl units), we analyzed CoQ_9 levels in our murine C2C12 cell model[67]. While *Tomm40* and *Tomm22* KD, singly and in combination, resulted in no differences in levels of CoQ (**Fig. 2-S3**) in whole cell lysates, there were significant reductions in CoQ_9 in isolated mitochondria (**Fig. 2-3G**). Together, these results indicate that TOMM40 and TOMM22 of the TOM complex may impact mitochondrial function in skeletal myotubes at least in part by its effect on the CoQ biosynthesis pathway.

2.3.4 *TOMM40* and *TOMM22* KD promote mitochondrial fission and upregulate mitophagy in response to mitochondrial damage

Having observed mitochondrial dysfunction with the suppression of *TOMM40* and *TOMM22*, we next investigated mitochondrial dynamics, a key process that regulates cellular and mitochondrial metabolism[68]. By transmission electron microscopy (TEM) of C2C12 myotubes transfected with *Tomm22* and *Tomm40* siRNAs compared to NTC, we observed an increase in constriction events within individual mitochondria, indicative of increased fission events (**Fig. 2-4A**), along with a significant decrease in average mitochondrial length (**Fig. 2-4B**). This change in mitochondrial morphology led us to hypothesize that *Tomm40* and *Tomm22* KD affect mitochondrial dynamics in skeletal muscle. By qPCR in *TOMM22* and *TOMM40* KD C2C12 and hSkMC cells, we observed upregulated expression of *FIS1* and *DNM1L/DRP1*, genes that encode markers of mitochondrial fission (**Fig. 2-4D, E**). This was accompanied by a decrease in gene expression of the mitochondrial fusion markers *MFN2* and *OPA1*. With a shift towards mitochondrial fission in *TOMM22* and *TOMM40* KD skeletal muscle cells, we observed an increase in mitochondrial density (**Fig. 2-4F**) and mtDNA copy number (**Fig. 2-4G**), which together suggest increased mitochondrial damage and support the excessive mitochondrial fission observed.

We further used TEM for analyzing mitochondrial morphology to assess mitochondrial damage (**Fig. 2-5A**). KD of *Tomm40* and *Tomm22* resulted in a reduced percentage of type 1 (healthy) mitochondria, and an increase in both type 2 and 3 (damaged and ruptured) mitochondria (**Fig. 2-5B, C**)[69]. Collectively, these results indicate that while there is an increase in new mitochondria created from fission events in knock-down cells (as confirmed in **Fig. 2-4F**, **G**), the majority are damaged. Furthermore, we noticed a significant increase in percentage of mitophagosomes in *Tomm40* and *Tomm22* KD C2C12 cells (**Fig. 2-5D**). This observation was confirmed by an increase in gene and protein expression of the mitophagy markers *PINK1* and *PRKN* in hSkMCs (**Fig. 2-5E,**

F). Accordingly, these results support a compensatory mechanism due to the mitochondrial damage induced by *TOMM40* and *TOMM22* KD in which mitochondrial fission is upregulated leading to increased mitophagy that removes damaged mitochondria and maintains mitochondrial homeostasis.

In vivo, gastrocnemius skeletal muscle isolated from AAV8-*Tomm40* shRNA injected male mice (14-weeks old) showed significant reduction in number of mitochondria (**Fig. 2-5I**). In addition, mitochondria morphology was affected such that length of intermyofibrillar and subsarcolemmal mitochondria were both reduced (**Fig. 2-5J, K**). Consistent with our *in vitro* findings, the percent of ruptured mitochondria increased drastically in *Tomm40* shRNA-induced male mice, indicating phenotypes of myopathy (**Fig. 2-5L**)[70].

2.3.5 Overexpression of *TOMM40* and *BCAP31* rescue statin-induced mitochondrial dysfunction

We next sought to determine whether overexpressing *TOMM40* and *TOMM22*, singly and in combination, can rescue simvastatin-induced effects on mitochondrial function. First, we demonstrated that treatment of C2C12 and hSkMC cells with 2 μM simvastatin for 24 hrs resulted in decreased OCR (both basal and maximal oxygen consumption) and ATP production (**Fig. 2-6A, B)**. Accordingly, mitoROS production was increased by simvastatin in skeletal myotubes (Fig. 6E). Introduction of *TOMM40*- and *TOMM22*-containing lentiviral plasmids, singly and in combination, to these simvastatin-treated cells resulted in no changes in OCR and mitoROS levels (**Fig. 2-6A, B**). Similarly, over-expressing *Tomm20*, another key component of the TOM complex, did not reverse the simvastatin effect on basal respiration, ATP production, and mitoROS levels in C2C12 cells (**Fig. 2-6A-C**).

Since TOMM40 is known to impact mitochondrial function by binding to BCAP31 at MERCs[39] and having shown that 2uM simvastatin decreases *BCAP31* expression (**Fig. 2-6D, E**), we then tested whether TOMM40 and/or TOMM22 require BCAP31 to rescue simvastatin-induced mitochondria dysfunction. We found that overexpressing both *TOMM40* and *BCAP31* in simvastatin-treated C2C12 and hSkMC myotubes resulted in the rescue of ATP production, basal respiration, maximal respiration, and proton leak (**Fig. 2-6F-M**). However, *TOMM22* in combination with *BCAP31* did not rescue mitochondria function in simvastatin treated cells, consistent with previous evidence of a TOMM40-BCAP31 specific interaction[39].

In accord with inhibition of mevalonate synthesis by statins[1], simvastatin (2 μM for 24 hrs) resulted in reduced levels of two products of the mevalonate/CoQ biosynthesis pathway - cholesterol and CoQ - in mitochondria isolated from C2C12 cells by subcellular fractionation (**Fig. 2-6N, O**). These effects were not reversed by overexpression of *Tomm40* and *Tomm22*, or of *Tomm20*. Nor did overexpression of *Bcap31* with *Tomm40* or *Tomm22* increase mitochondrial cholesterol levels to baseline levels (**Fig. 2-S6**)**.** Together, these results indicate that effects of statin other than downregulation of *Tomm40*, *Tomm22, Tomm20, and Bcap31* are primarily responsible for maintaining cholesterol and CoQ content in mitochondria of skeletal muscle cells.

2.3.6 *TOMM40* and *TOMM22* rescue statin-induced mitochondrial fusion and fission events

As we had observed with *Tomm40* and *Tomm22* KD, TEM image analysis of C2C12 myotubes treated with simvastatin 2 μM for 24 hours (**Fig. 2-7A**) resulted in reduced mitochondria length and increased width (**Fig. 2-7B, C**). The likelihood that this resulted from increased mitochondrial fission events was supported by qPCR analysis showing that simvastatin treatment resulted in increased expression of *FIS1* and *DRP1* and reduced expression of *MFN2* and *OPA1* (**Fig. 2-7D, E**). Furthermore, both mitochondrial density and mtDNA copy number increased in simvastatin-treated C2C12 myotubes compared to control (**Fig. 2-7F, G**). Thus, as with *TOMM40* and *TOMM22* KD, simvastatin treatment of skeletal myotubes increased mitochondrial fission and damage.

We next tested whether overexpressing *TOMM40* and *TOMM22*, singly and in combination, could rescue these effects of simvastatin on mitochondrial dynamics. Notably, there was a reversal of statin effects on mitochondrial length and width after the addition of *Tomm40* and *Tomm22/40* plasmids in C2C12 myotubes (**Fig. 2-7B, C**). Moreover, *TOMM40* and *TOMM22* overexpression in both C2C12 and hSkMC cells resulted in reversal of the statin effects on gene expression of the mitochondrial fission and fusion markers described above (**Fig. 2-7D, E**), while this was not the case for *Tomm20* overexpression in C2C12 myotubes (**Fig. 2-7D**). Although *BCAP31* in conjunction with *TOMM40* or *TOMM22* overexpression rescued gene expression of mitochondrial fission and fusion markers, *BCAP31* alone only rescued *FIS1* gene expression (**Fig. 2-S7**). This suggests that other than BCAP31's known interaction with FIS1, it is not required for rescuing simvastatin-induced mitochondria dynamics.

Interestingly, the addback of *Tomm40* and *Tomm22* plasmids to simvastatin-treated cells resulted in further increases in mtDNA copy number and mitochondrial density (**Fig. 2-7F, G**). Together with the evidence that *TOMM40* and *TOMM22* expression reverse statin effects on mitochondrial dynamics, this suggests that this treatment may suppress statin-induced mitophagy while generating new, healthy mitochondria. Consistent with this hypothesis, we observed by TEM that simvastatin-treated C2C12 cells had a lower percentage of healthy Type 1 mitochondria (sharp cristae and dense matrix) and a higher percentage of Type 2 (dilute cristae and/or dilute matrix) and Type 3 (ruptured) mitochondria, representing abnormal mitochondrial morphology and signs of mitochondrial injury[69]. In addition, there was an increase in the percentage of mitophagosomes per cell in simvastatin-treated skeletal muscle (**Fig. 2-8D**). Consistent with these observations, we demonstrated increased expression of mitophagy biomarkers *PINK1* and *PARKIN* with simvastatin treatment by qPCR (**Fig. 2-8E, F**).

We then showed by TEM that overexpressing *Tomm40* and *Tomm22* in statin-treated C2C12 myotubes resulted in an increase in Type 1 mitochondria and a reduction in Type 2 and Type 3 mitochondria, indicating that *Tomm22* and *Tomm40* are able to rescue, at least in part, simvastatin-induced mitophagy. Consistent with this effect, *TOMM22, TOMM40*, and *TOMM22/40* (but not Tomm20) overexpression reduced *PINK1* and *PARKIN* expression to control levels (**Fig. 2-8E-F**). In summary, these results demonstrate that simvastatin promotes mitochondrial fission and mitophagy, resulting in an increase in damaged mitochondria, while overexpressing *TOMM22* and *TOMM40* can reverse these effects, thus maintaining mitochondrial quality and homeostasis.

2. 4 Discussion & Conclusion

Statin-associated myopathy is the most prevalent adverse effect among statin users, but its mechanism remains unclear. We here report that TOMM40 and TOMM22, key members of the TOM complex whose transcriptional expression is suppressed by simvastatin in skeletal muscle cells, are essential in maintaining mitochondrial function and quality by promoting their oxidative function, retaining CoQ and cholesterol content, and preserving their morphology and dynamics. Consistent with our findings in skeletal muscle, previous studies in epithelial ovarian cancer and HeLa cell lines showed that knockdown of *TOMM40* disrupted mitochondrial membrane potential, ATP, and ROS levels[21,71-73]. It has been suggested that mitochondrial dysfunction due to suppression of *TOMM40* and *TOMM22* is caused by interference with the uptake of mitochondria-targeted proteins[74]. Notably, in the case of *TOMM22*, its suppression or mutation results in inactivation of mitochondrial proteins due to misfolding in yeast[75], as well as apoptosis of human epithelial and endothelial cells and zebrafish hepatocytes[76].

We also found that *TOMM40* and *TOMM22* KD reduced cholesterol content in skeletal muscle cells and isolated mitochondria, suggesting that this effect contributes to the mitochondrial dysfunction observed with KD of these TOM components. Interestingly, adding back LDL cholesterol restored mitochondrial cholesterol levels in *TOMM22* KD skeletal myotubes, but not in *TOMM40* KD cells, suggesting that TOMM40 is necessary for maintaining cholesterol levels in muscle mitochondria[77]. However, neither KD group showed an improvement in mitochondrial OCR after the addition of LDL, indicating that under these conditions, mitochondrial respiration and function are regulated by factors other than cholesterol content, or possibly that the added cholesterol was not effectively introduced into the mitochondrial membrane.

CoQ_{10} (humans) or CoQ_9 (in mice) of the CoQ biosynthesis pathway, essential for regulating the mitochondria electron transport chain and thus mitochondrial function, are dependent on isoprenoids, products of the mevalonate pathway[78]. To date, it is still unclear how CoQ and its precursors are transported across the outer mitochondrial membrane into the mitochondrial matrix of skeletal muscle cells. However recently, Tai et al.,[79] showed in *Saccharomyces cerevisiae* that isopentenyl pyrophosphate (IPP) molecules, precursors of both CoQ and cholesterol, may enter the mitochondrial matrix via an IPP transporter situated on the inner mitochondrial membrane. Together with our results showing *TOMM40* and *TOMM22* KD in C2C12 skeletal myotubes resulted in a significant reduction of mitochondrial CoQ content, we suggest that TOMM40 and TOMM22 may affect the transport of proteins required for CoQ biosynthesis, including those involved in the transport of 4-hydroxybenzoate (4-HB) and isoprenoid pyrophosphates, into the mitochondria[80]. Further studies are necessary to determine which transporters and enzymes of the CoQ biosynthesis pathway are recognized and imported into mitochondria by TOMM40 and TOMM22, thus promoting CoQ synthesis[81].

Mitochondrial dynamics involves coordination of fusion and fission events that define mitochondria number, size, and morphology[82]. Accumulating evidence reveals a strong association between mitochondrial function and dynamics[83,84]. In addition, genes regulating mitochondrial dynamics, including *MSTO1*, have been shown to impact other cellular functions including oxidative stress, apoptosis, and mitophagy, as well as to induce myopathy and ataxia[85-89,39]. We show here for the first time, using both TEM and expression of biomarkers, that KD of TOMM40 and *TOMM22* in skeletal myotubes causes a shift in mitochondrial dynamics towards increased fission events, with a resulting increase in mitophagy as a means of eliminating damaged mitochondria and maintaining mitochondria quality[90,91]. It is plausible that TOMM40 regulates mitochondrial fusion and fission by directly or indirectly interacting with known markers of fission and fusion localized at MERCs, such as FIS1, DRP1, and MFN2[92]. Additionally, studies in yeast have shown TOMM22 to interact with PINK1, a key regulator of mitochondrial quality and mitophagy[93-95]. In mammalian cells, dephosphorylation of TOMM22 impairs PINK1 import into the mitochondria, promoting mitophagy[96]. The effect on mitophagy may be mediated, at least in part, by increased mitoROS as a consequence of mitochondrial dysfunction[97,98]. Consistent with this mechanism, we observed that both mitoROS levels and the mitophagy markers *PINK1* and *PRKN* are upregulated with *TOMM40* and *TOMM22* KD. Thus, our results indicate *TOMM40* and *TOMM22* to be key genes in regulating mitochondrial function, dynamics, and mitophagy.

Based on these findings and the evidence that simvastatin downregulates *TOMM40* and *TOMM22* gene expression, we compared the effects of simvastatin exposure with those of *TOMM40* and *TOMM22* knockdown on mitochondrial function and dynamics and tested whether overexpression of these genes could reverse the statin effects. We showed that simvastatin treatment exerted effects on mitochondrial dynamics and morphology in skeletal muscle cells similar to those observed with both *TOMM40* and *TOMM22* KD. Previous studies in yeast cells reported that statins impair mitochondrial morphology, represented by an increase in aggregated mitochondria, due to disruption of mitochondrial function and membrane potential[99-101]. However, we are the first to show that the reduction in mitochondrial length and increased mitochondrial fragmentation in C2C12 cells exposed to simvastatin can be explained by an increase in mitochondrial fission and decrease in fusion events. As with *TOMM40* and *TOMM22* KD, the shift towards mitochondrial fission resulted in increased mitophagy (e.g. via *PINK1* and *PRKN*) to promote the removal of damaged mitochondria[102,103]. We also showed in our *in vivo* model that KD of *TOMM40* in mice presented signs of myopathy in gastrocnemius skeletal muscle, similar to phenotypes observed with statin treatment in previous rodent studies[104,105]. Notably, overexpression of *TOMM40* and *TOMM22* rescued the changes in mitochondrial dynamics and morphology, and mitophagy, caused by simvastatin treatment of C2C12 myotubes.

Consistent with previous studies[11,12,57], we showed that simvastatin treatment of C2C12 myotubes resulted in reduction of ATP production and mitochondrial respiration, together with an increase in mitoROS production. We also observed that simvastatin reduced free cholesterol content in whole cells as well as in isolated mitochondria[65], an effect that might be linked to impaired mitochondrial structure and membrane potential, rather than mitochondrial function. Moreover, as also expected from statin inhibition of the mevalonate pathway, we showed that simvastatin treated C2C12 cells exhibited a reduction in mitochondrial CoQ levels, an effect that has been suggested to contribute to SAMS[106]. These results paralleled those observed with *TOMM40* and *TOMM22* KD, raising the question as to whether reduced expression of these genes contributes to these statin effects in muscle, as was the case for statin-induced changes in mitochondrial morphology and dynamics. In the case of CoQ, the effects of simvastatin and *TOMM40* and *TOMM22* KD were additive (**Fig. 2-S4**). However, overexpression of these genes, including *TOMM20,* another major TOM complex subunit encoding gene[107], as well as *BCAP31*, failed to restore statin impairment of mitochondrial CoQ and cholesterol content. Thus, the reduction of mitochondrial cholesterol and CoQ levels by statin may be due primarily to inhibition of the mevalonate pathway and independent of reduced expression of genes encoding components of the TOM complex.

TOMM40 has been shown to bind to several ER membrane proteins at MERCs[33,39]. Among these, BCAP31 has been shown to play a key role in maintaining oxidative phosphorylation, where knockdown of *BCAP31* in U2OS cells showed impaired mitochondrial function and reduced ATP levels[39]. In addition, we have shown that knockdown of TOMM40 in skeletal muscle cells downregulates *BCAP31* expression (**Fig. 2-S8**). Namba further showed using coimmunoprecipitation that BCAP31 directly binds to TOMM40 and NDUFS4 thereby inducing translocation into mitochondria of NADH:ubiquinone oxidoreductase (mitochondrial complex I) core subunit 4 (NDUFS4). In addition to TOMM40, BCAP31 is also known to physically interact with FIS1 at MERCs to regulate mitochondrial fusion/fission dynamics and mitochondrial signaling[39,108,109], Our finding that overexpressing *BCAP31* in simvastatin-treated skeletal myotubes rescues *FIS1* expression is consistent with the possibility that TOMM40 can regulate mitochondria fission through its direct binding to BCAP31. Moreover, we have shown here for the first time that statin exposure of muscle cells reduces *BCAP31* gene expression, and that combined overexpression of *TOMM40* and

BCAP31 in statin-treated C2C12 and hSKMC myotubes is sufficient to rescue impaired mitochondrial oxidative function. This result suggests that statin impairment of mitochondrial respiration can be attributed to disruption of a TOMM40-BCAP1 interaction at MERCs, a mechanism that differs from that responsible for a role of *TOMM40* and *TOMM20* suppression in mediating statin effects on mitochondrial dynamics and structure. Future studies will be required to determine direct and indirect interactions of TOMM40, TOMM22, and BCAP31 with other proteins at MERCs that may impact adverse mitochondrial effects of statin treatment and predispose to the development of SAMS.

2.5 Methods

2.5.1 Cell culture

C2C12 murine myoblasts and primary hSkMCs were purchased from American Type Culture Collection (ATCC; CRL-1772 & PCS-950-010). C2C12 cells were cultured in DMEM containing 4.5 g/L glucose and L-glutamine (Gibco) supplemented with 10% fetal bovine serum (FBS; Thermo Fisher Scientific) and penicillin-streptomycin (Gibco) at 37°C and 5% CO_2. After passaging cells, C2C12 myoblasts were differentiated into myotubes by replacing media with DMEM containing 2% horse serum (Gibco). Fresh medium was replaced every 2 days and cells were incubated for 5-7 days to completely differentiate into myotubes before experimentation. For hSkMCs, cells were cultured in mesenchymal stem cell basal medium (PCS-500-030, ATCC) supplemented with L-glutamine, 5 ng/mL rh EGF, 10 µM dexamethasone, 5 ng/mL rh FGF-b, 25 µg/mL rh insulin, 4% FBS (PCS-950-040, ATCC) and penicillin-streptomycin (Gibco). 24-96 hrs after passaging, hSkMC cells were differentiated into myotubes using skeletal muscle differentiation tool (PCS-950-050, ATCC) for 2 days before experimentation. Cells were routinely tested for mycoplasma using MycoAlert™ PLUS mycoplasma detection kit (Lonza) and only mycoplasma negative cells were used.

2.5.2 siRNA reverse transfections

To achieve knock-down (KD) of *TOMM22* and *TOMM40*, C2C12 and hSkMC cells were seeded at 100,000 cells per well in 6-well plates. Upon seeding, cells were reverse transfected with 10 µM of non-targeting control (NTC), *TOMM22* and/or *TOMM40*-targeted siRNAs using Lipofectamine RNAiMax transfection reagent (Thermo Fisher Scientific) and Opti-MEM 1 (Gibco) for 48hrs. All siRNAs were purchased from Thermo Fisher Scientific – human *TOMM22* siRNA (s32549); human *TOMM40* siRNA (s20449); mouse *Tomm22* siRNA (s104588); mouse *Tomm40* siRNA (s79125); Silencer Select Negative Control siRNA (s79125). For C2C12, cells were transfected twice, at day 0 (myoblasts) and day 3 (myotubes) in differentiation media and then harvested after day 5 for experimentation.

2.5.3 Overexpression plasmids

Human and mouse pCMV-EGFP expressing- *TOMM40/Tomm40* (human: NM_001128916.2, mouse: NM_016871.2), *TOMM22/Tomm22* (human: NM_020243.5, mouse: NM_172609.3), *Tomm20* (mouse: NM_024214.2), *BCAP31/Bcap31* (human: NM_001139457.2, mouse: NM_012060.5), and empty vector (EV; ORF_stuffer) plasmids stored in bacterial glycerol stocks were purchased from VectorBuilder Inc. Expression plasmids were cultured on Luria-Bertani (LB) Agar plates containing ampicillin at 37°C. Single colonies were selected and grown separately in LB broth at 37°C with continuous shaking (225 rpm) overnight. DNA plasmids were then purified and extracted using the ZymoPURE II Plasmid Midiprep Kit (Zymogen) according to manufacturer's protocol. For overexpression studies, both C2C12 and hSkMC cells were first differentiated into myotubes using respective differentiation media. After differentiation, cells were transiently transfected with purified *TOMM40/Tomm40*, *TOMM22/Tomm22,* and *Tomm20* expression plasmids, singly and in combination, or matched empty vector, using Lipofectamine 3000 transfection reagent (Thermo Fisher Scientific). In parallel, 2 µM simvastatin was added to the cell media and cells were collected after 24-48 hrs. Simvastatin was obtained as a gift from Merck and activated as previously described[110].

2.5.4 Animal studies

6-week old C57BL/6J male and female mice (n=6 per group) were purchased from Jackson Laboratory (Bar Harbor, ME) and placed on a high-fat western diet. At 8 weeks of age, mice were intraperitoneal (IP) injected with either 4×10^{11} GC AAV8-*Tomm40* shRNA or AAV8-CMV-null as a control (VectorBuilder). Weekly bodyweight and food intake measurements were recorded. At 14-weeks old, mice were terminated and gastrocnemius muscle tissues were collected and immediately fixed in 2% glutaraldehyde + 2% paraformaldehyde solution for transmission electron microscopy.

2.5.5 Mitochondrial respiration measurements

In vitro oxygen consumption rate was measured in fully differentiated C2C12 and hSkMC skeletal myotubes with the Agilent Seahorse XFe96 Extracellular Flux Analyzer. Cells were seeded at 1,000 per well in 96-well plates, with XF assay medium (Agilent) supplemented with 2 mM sodium pyruvate (Gibco), 2 mM GlutaMAX™ (Gibco), and 10 mM glucose (Sigma), at pH 7.4. During experimentation, 1.5 µM oligomycin, 2 µM FCCP, and 2 µM Antimycin A + Rotenone (Seahorse XF Cell Mito Stress Test Kit, Agilent) was added sequentially via injection ports, to calculate basal and maximum respiration and ATP production. Oxygen consumption rate (OCR) values were presented with non-mitochondrial oxygen consumption deducted and normalized to total protein concentration per well using Bradford assay.

2.5.6 Fluorescence quantification

To detect mitochondria superoxide production in C2C12 cells, myotubes were incubated with 5 µM MitoSOX™ Red (Molecular Probes) for 20 min at 37°C. Cells were then rinsed twice in pre-warmed 1X phosphate-buffered saline (PBS) which was then replaced with phenol red-free DMEM (21063029; Gibco) supplemented with glucose and sodium pyruvate. Fluorescence was detected and quantified at an excitation/emission of 396/610 nm using an Agilent BioTek™ microplate fluorescence spectroscopy reader and BD LSRFortessa™ Cell Analyzer flow cytometer following the protocol of Kauffman et al[111]. To quantify mitochondrial density, MitoTracker™ Deep Red FM (100 nM) was added to C2C12 cells for 30 min at 37°C, washed twice with 1X PBS and replaced with phenol red-free DMEM supplemented with glucose and sodium pyruvate (Gibco). MitoTracker fluorescence was quantified at an excitation/emission of 644/665 nm. All absorbance readings were normalized to total protein concentration by Bradford assay.

2.5.7 Isolation of mitochondria by subcellular fractionation

Mitochondria were isolated from C2C12 and hSkMC cells according to the method of Wettmarshausen and Perocchi[112]. Cells were rinsed in 1X PBS twice, dislodged with 0.25% Trypsin-EDTA (Gibco), washed again in 1X PBS and centrifuged at 600 x g for 5 min at 4°C. Pelleted cells were resuspended in MSHE + BSA buffer (210 mM mannitol, 70 mM sucrose, 5 mM HEPES, 1 mM EGTA, and 0.5% BSA, at 7.2 pH). Samples were transferred to a small glass dounce and homogenized. The homogenate was centrifuged at 600 x g for 10 min at 4°C, and the supernatant was extracted and centrifuged at 8,000 x g for 10 min at 4°C. The isolated pellet containing the purified crude mitochondria was dried down by nitrogen gas and snap frozen in liquid nitrogen for quantification of mitochondrial cholesterol and CoQ levels.

2.5.8 Lipid extraction for LC-MS/MS

C2C12 whole cell lysates and isolated mitochondria pellets were resuspended in 100 µL of 150 mM KCl. Ten percent of the cell suspension was removed from each tube and placed into a new tube. The extra 10% was later used in a bicinchoninic acid (BCA) assay to measure relative protein content in each sample. Protein content derived from the BCA assay was used to normalize CoQ measurements.

The remaining 90% of the cell suspension was mixed with glass beads and 600 µL of cold methanol containing 0.25 µM CoQ_6 (CoQ_6 is used to normalize for total CoQ extracted). Cell suspensions were subjected to lysis on a vortex genie at 4°C for 10 min. Afterward, 400 uL of cold petroleum ether was added to each tube and vortexing was repeated for 3 min. To separate the petroleum ether and methanol phases, the tubes were centrifuged at 1,100 x g for 3 min and the top (petroleum ether) phase was collected into a new tube (Tube B). Again, 400 µL of petroleum ether was added to each tube containing methanol, and the vortexing/centrifuge steps were repeated. The final top layer was collected and added to Tube B. Petroleum ether was dried under a stream of argon gas, and dried lipids were resuspended in 50 µL of mobile phase (78:20:2 methanol:isopropanol:ammonium acetate).

2.5.9 Measurement of CoQ_9 by LC-MS/MS lipidomics

LC-MS/MS Lipidomics Data Acquisition. A Vanquish Horizon UHPLC system (Thermo Scientific) connected to an Exploris 240 Orbitrap mass spectrometer (Thermo Scientific) was used for targeted LC-MS analysis. A Waters Acquity CSH C18 column (100 mm × 2.1 mm, 1.7 µm) was held at 35°C with the flow rate of 0.3 mL/min for lipid separation. A Vanquish binary pump system was employed to deliver mobile phase A consisting of 5 mM ammonium acetate in ACN/H2O558(70/30, v/v) containing 125 µL/L acetic acid, and mobile phase B consisting of 5 mM ammonium acetate in IPA/ACN (90/10, v/v) containing 125 µL/L acetic acid. The gradient was set as follows: B was at 2% for 2 min and increased to 30% over the next 3 min, then further ramped up to 50% within 1 min and to 85% over the next 14 min, and then raised to 99% over 1 min and held for 4 min, before being re-equilibrated for 5 min at 2% B. Samples were ionized by a heated ESI source with a vaporizer temperature of 350°C. Sheath gas was set to 50 units, auxiliary gas was set to 8 units, sweep gas was set to 1 unit. The ion transfer tube temperature was kept at 325°C with 70% RF lens. Spray voltage was set to 3,500 V for positive mode. The targeted acquisition was performed with tMS2(targeted MS2) mode: tMS2 mode was for measuring CoQ_6(m/z 591.4408, internal standard) and CoQ_9(m/z 795.6286) in positive polarity at the resolution of 15,000, isolation window of 2m/z, normalized HCD collision energy of either 40% or stepped HCD energies of 30% and 50%, standard AGC target and auto maximum ion injection time.

Data Analysis. Targeted quantitative analysis of all acquired compounds was processed using TraceFinder 5.1 (Thermo Scientific) with the mass accuracy of 5 ppm. The result of peak integration was manually examined.

2.5.10 Lipid extraction and intracellular cholesterol quantification

Cholesterol was extracted from cells with hexane-isopropanol (3:2, v/v), dried under nitrogen gas and reconstituted with buffer (0.5 M potassium phosphate, pH 7.4, 0.25 M NaCl, 25 mM cholic acid, 0.5% Triton X-100). Intracellular cholesterol levels were then quantified with the Amplex Red Cholesterol Assay Kit (Life Technologies) according to the manufacturer's protocol.

2.5.11 Sample preparation for electron microscopy

C2C12 cells were grown on MatTek glass bottom dishes (P35G-1.5-14-C, MatTek) and fixed in 2% glutaraldehyde + 2% paraformaldehyde solution (prepared by Electron

Microscopy Lab, UC Berkeley) for 24 hrs. After fixation, cells and tissues were washed 3-times for 5 min in 0.1 M sodium cacodylate buffer, pH 7.4. Samples were then post-fixed in 1% osmium tetroxide + 1.6% potassium ferricyanide (KFECn) in 0.1 M sodium cacodylate buffer for 30 min, before undergoing 3 washes at 15 min each. Cells were then dehydrated in a serial diluted ethanol solution of 30, 50, 70, 90, and 100%, for 10 min each. Samples were infiltrated with 50% Epon-Araldite resin (containing benzyldimethylamine (BDMA) accelerator), followed by 100% resin for 1 hr each. Excess resin was removed from the MatTek dishes containing cells and polymerized at 60°C for 48 hrs.

2.5.12 Transmission electron microscopy

Using a dissecting blade, cells embedded in resin were removed from MatTek dishes and mounted on resin-embedded blocks for sectioning. Serial sections of 70-150 nm thickness were cut on a Reichert-Jung Ultracut E microtome and set on 1 x 2-mm slot grids covered with 0.6% Formvar film. Sections were then post-stained with 1% aqueous uranyl acetate for 7 min and lead citrate for 4 min[113]. Images of cell samples were taken on an FEI Tecnai 12 transmission electron microscope equipped with a 2k x 2k CCD camera with a 40 Megapixel/sec readout mode. Images were analyzed using ImageJ software according to the method by Lam et al[114]. Types of mitochondria were evaluated using the method described by Shults et al[115].

2.5.13 Immunoblotting

Cells were washed with PBS and lysed in M Cellytic Lysis Buffer containing 1% protease inhibitor (Halt ™ Protease Inhibitor Cocktail; Thermo Scientific) for 15 min with gentle vortexing. The cell lysate was centrifuged at 14,000 x g for 15 min, the supernatant was collected, and the protein concentration was measured by Bradford assay. Proteins were separated on a 4-20% Tris-polyacrylamide gradient gel (Bio-Rad) and transferred onto a nitrocellulose membrane using the iBlot™ 2 Gel Transfer Device (Thermo Fisher Scientific). Membranes were blocked in Tris-buffered saline with 0.1% tween (TBST) + 5% milk for 2 hrs to minimize non-specific antibody binding. Membranes were then incubated with primary antibodies, PARKIN (Prk8) mouse monoclonal antibody and GAPDH (14C10) rabbit monoclonal antibody (Cell Signal) diluted 1:1000 (v/v) in TBST overnight on a rotating platform at 4°C. After washing in TBST, membranes were incubated with secondary antibodies, anti-rabbit IgG (7074) and anti-mouse IgG (7076), HRP-linked antibodies (Cell Signal) at 1:2500 (v/v) dilution, for 30 min before a last series of washes. SuperSignal™ West Pico PLUS Chemmiluminescent Substrate (Thermo Fisher Scientific) was added to the membrane to visualize proteins[30].

2.5.14 RT-qPCR and mtDNA copy number

RNA was extracted from cells using RNeasy Mini Qiacube Kit (Qiagen) with the Qiacube Connect (Qiagen) according to manufacturer's protocol. cDNA synthesis from total

RNA was performed using High Capacity cDNA Reverse Transcription Kits (Applied Biosystems). Primers obtained from Elim Biopharmaceuticals were run with SYBR™ Green qPCR Master Mix (Thermo Fisher Scientific) on an ABI PRISM 7900 Sequence Detection System to quantify mRNA transcript levels. RT-qPCR primers used in this study are listed in **Table S1**. The mean value of triplicates for each sample was normalized to GAPDH as the housekeeping gene.

Total DNA was isolated from C2C12 cells using DNeasy Blood and Tissue Kit (Qiagen). qPCR was performed with SYBR™ Green qPCR Master Mix (Thermo Fisher Scientific) on an ABI PRISM 7900 Sequence Detection System according to the protocol outlined by Quiros et al[116]. Primers for mouse mtDNA (mMitoF1: *5′-CTAGAAACCCCGAAACCAAA-3′*, mMitoR1: *5′-CCAGCTATCACCAAGCTCGT-3′*) and mouse B2M (mB2MF1: *5′-ATGGGAAGCCGAACATACTG-3′*, mB2MR1: *5′CAGTCTCAGTGGGGGTGAAT-3′*) were used to amplify mtDNA and nuclear DNA, respectively. mtDNA copy number was determined by normalizing mtDNA to nuclear DNA. The delta delta Ct method was used to calculate fold change in mtDNA copy number.

2.5.15 Statistical analysis

All data are presented as the mean ± standard error of mean (SEM). *N*-values in the figures refer to biological replicates and at least 3 replicates were conducted per condition and experiment. *P*-values were calculated using Student's t-tests for two groups. To compare more than two groups, one-way analysis of variance (ANOVA) or Welch and Brown-Forsythe ANOVA with Tukey's post hoc test were used. Analyses were performed using GraphPad Prism 9 software (GraphPad Software, Inc.). $P<0.05$ was considered statistically significant.

2.6 Figures

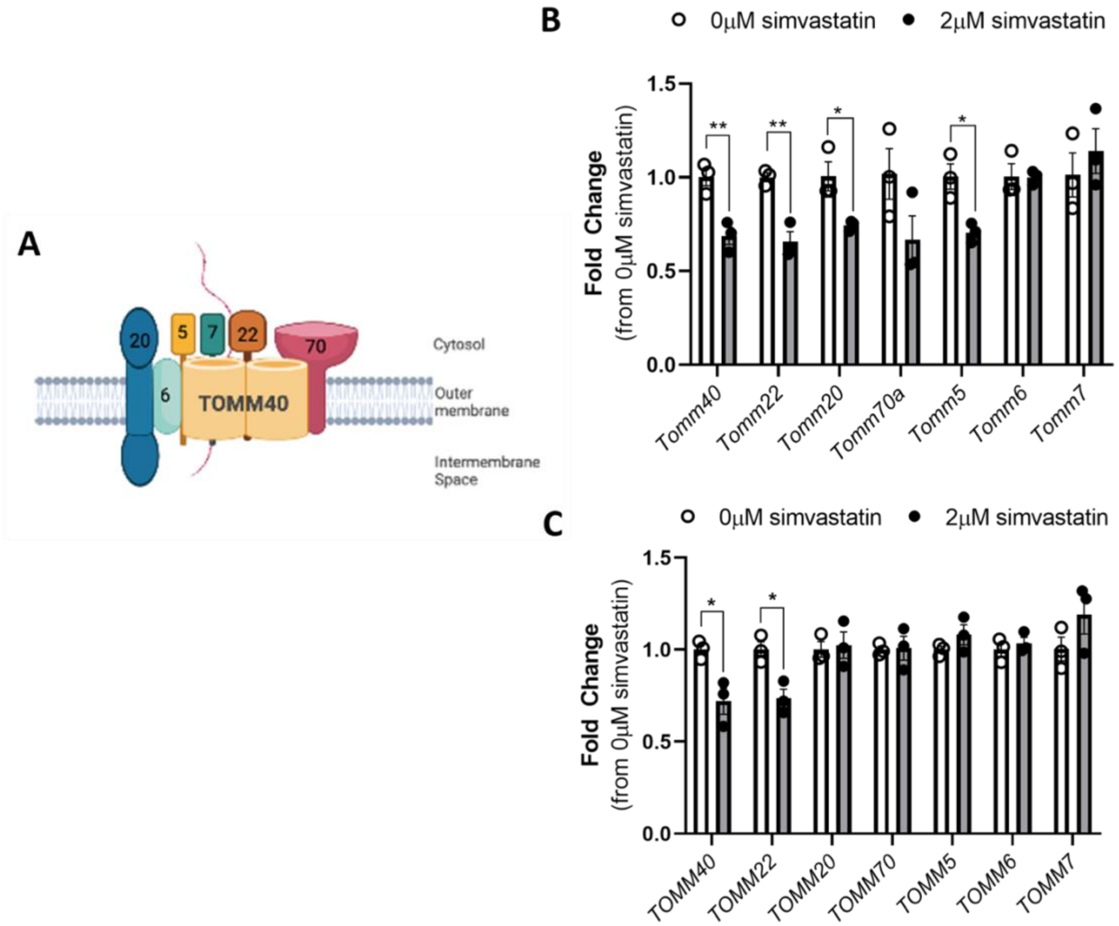

Figure 2-1. Simvastatin downregulates *TOMM40* and *TOMM22* in both C2C12 and hSkMC skeletal muscle. Differentiated C2C12 and primary hSkMC myotubes were treated with 2 μM simvastatin for 24 hrs. (A) A schematic diagram of the mammalian TOM complex, consisting of 7 subunits, located in the outer mitochondrial membrane. (B) Simvastatin treatment (2 μM) downregulates *Tomm40, Tomm22, Tomm20,* and *Tomm5* in differentiated C2C12 myotubes. (C) Simvastatin treatment (2 μM) downregulates *TOMM40 and TOMM22* in hSkMC myotubes. Numeric data represent mean ± SEM. *$p<0.05$, **$p<0.01$, ***$p<0.001$, ****$p<0.0001$ vs. 0 μM simvastatin by Student's t-test. ($n = 3$ biological replicates).

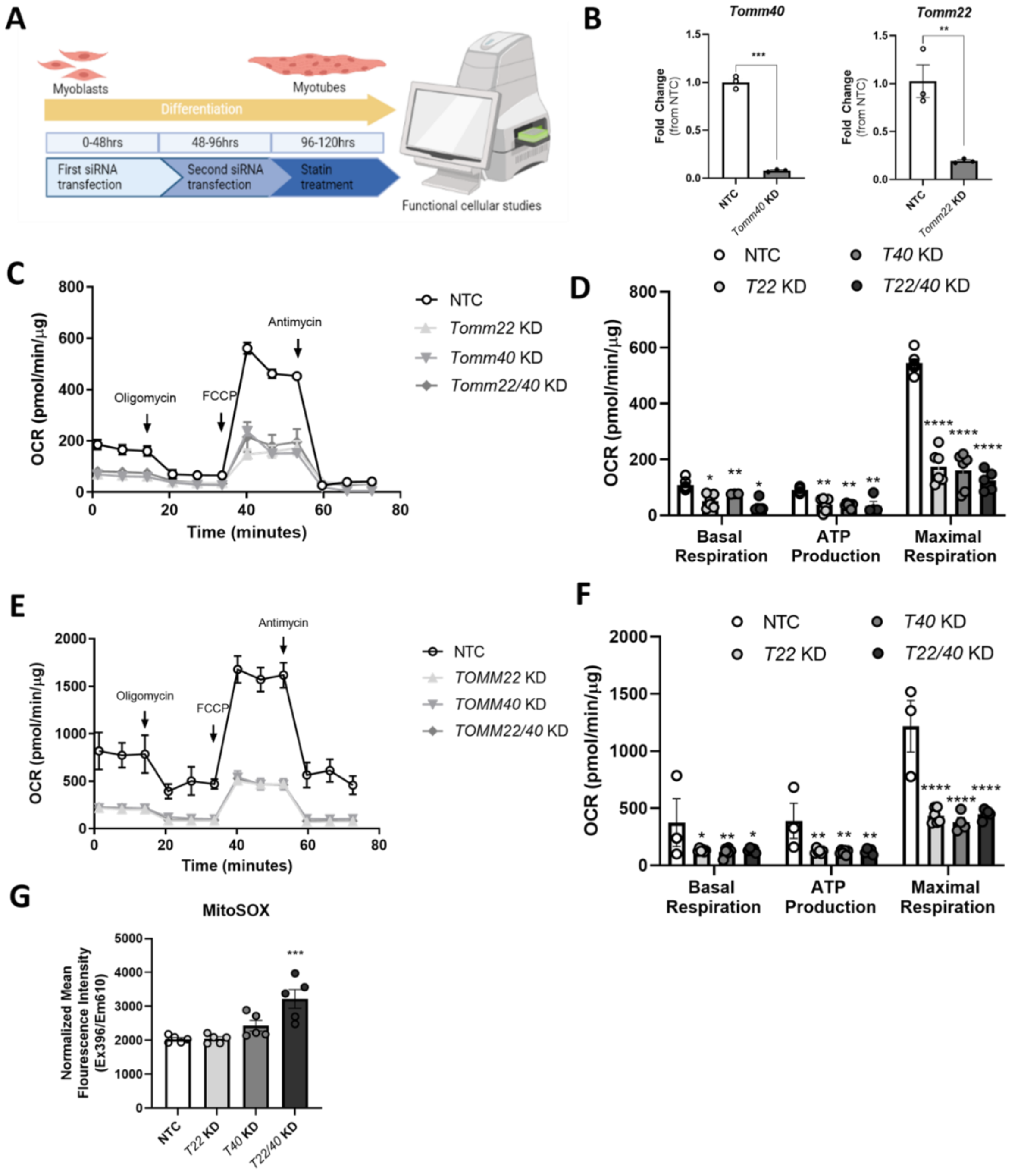

Figure 2-2. *TOMM40* and *TOMM22* knock-down decrease mitochondrial oxygen consumption rate and promote mitochondrial superoxide production. (A) Schematic illustration of the two-step transfection and differentiation experiment in C2C12 cells, *in vitro*. (B) Confirmation of *Tomm40* (T40) and *Tomm22* (T22) KD in C2C12 myotubes by ~92% and ~85%, respectively, measured with qPCR. (C) Oxygen consumption rates of C2C12 myotubes transfected with Tomm40 and Tomm22 siRNAs vs. NTC were quantified using the Seahorse 96e Extracellular Flux Analyzer.

With the addition of oligomycin, FCCP, and Antimycin A + Rotenone, basal respiration, ATP production, and maximal respiration were quantified. (D-F) The same experiment done in C2C12 cells (C-D) was conducted in primary hSkMC cells. (G) Mitochondrial superoxide production with *Tomm40* and *Tomm22* KD in C2C12 cells was quantified by MitoSOX fluorescence probe. All values were normalized to protein concentration by Bradford assay. All graphical and numeric data represent mean ± SEM. *$p<0.05$, **$p<0.01$, ***$p<0.001$, ****$p<0.0001$ vs. NTC by Student's t-test. ($n = 3$-12 biological replicates).

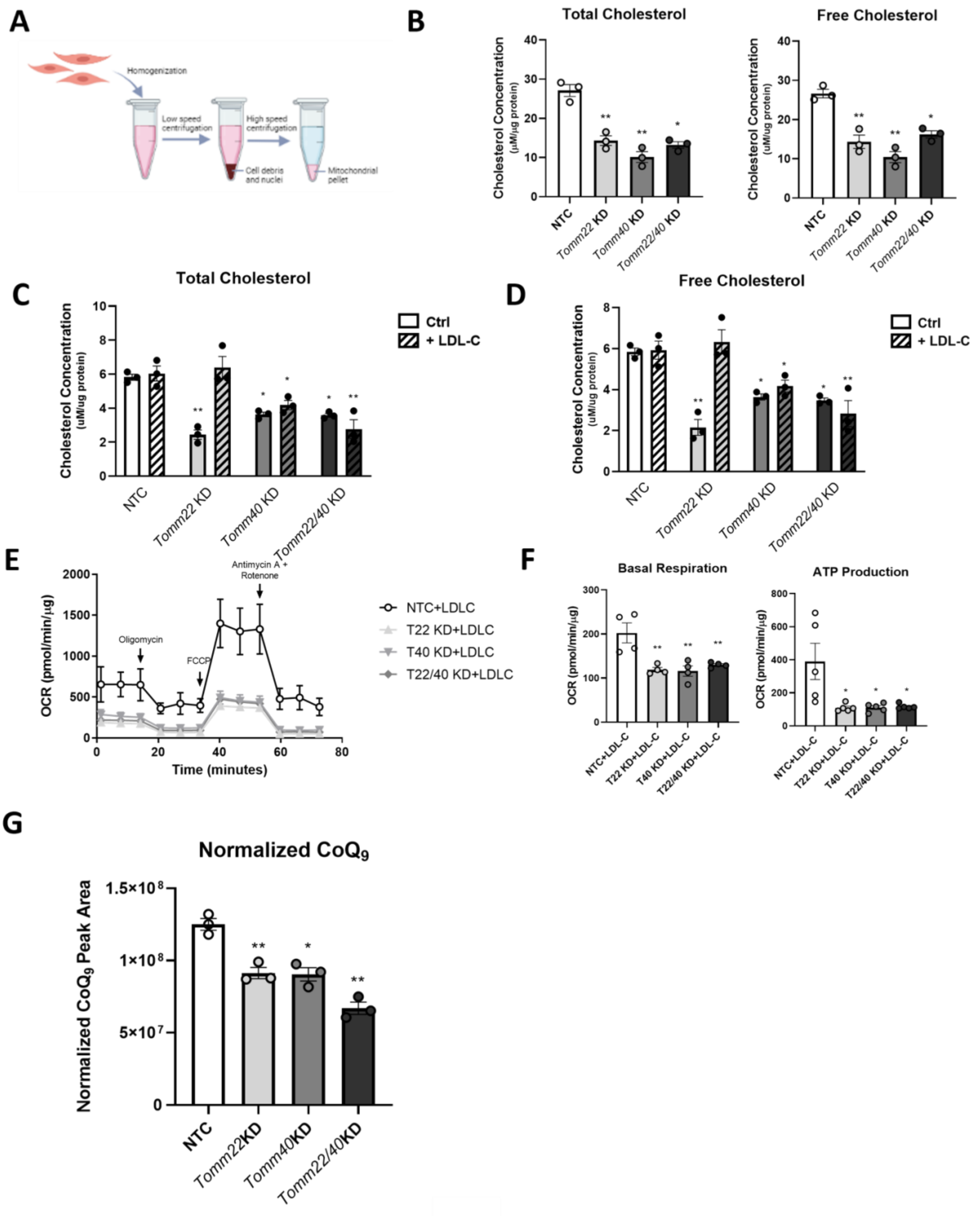

Figure 2-3. *Tomm40* and *Tomm22* regulate mitochondrial cholesterol content and CoQ levels in C2C12 myotubes. (A) Subcellular fractionation was performed to isolate crude mitochondria from whole cells. (B) Total and free cholesterol levels in mitochondria isolated from C2C12 myotubes transfected with NTC, *Tomm40*, and *Tomm22* siRNAs, singly and in combination. (C-D) In a separate experiment, after cells

were transfected with siRNAs, 50 µg/mL LDL-C was added to cell media for 24 hrs. Total and free cholesterol were quantified in the mitochondria using Amplex Red Cholesterol Assay. (E) OCR levels were assessed in C2C12 cells after the LDL-C addback and (F) basal respiration and ATP production were quantified using Wave software (*n = 10-12* biological replicates). (G) Total CoQ from isolated mitochondria of NTC, *Tomm40*, *Tomm22*, and *Tomm22/40* KD C2C12 cells were quantified by LC-MS/MS. All values were normalized to protein concentration, measured by BCA. All graphical and numeric data represent mean ± SEM *$p<0.05$, **$p<0.01$, ***$p<0.001$, ****$p<0.0001$ vs. NTC (without LDL-C addback) by Welch and Brown-Forsythe ANOVA or Student's t-test. (*n = 3-6* biological replicates).

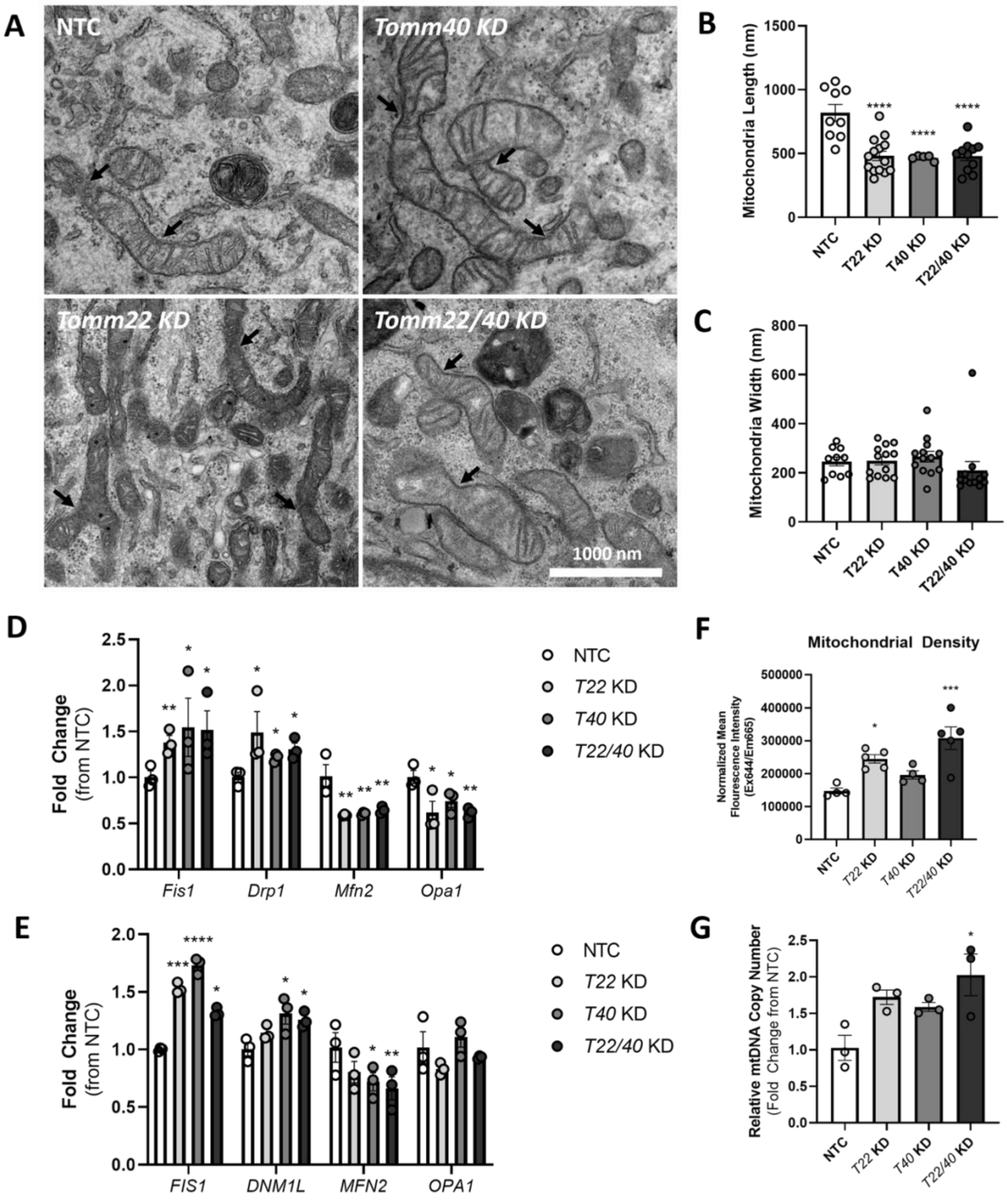

Figure 2-4. *TOMM40* and *TOMM22* knock-down, singly and in combination, impair mitochondrial dynamics in skeletal myotubes. (A) TEM micrographs of NTC, Tomm40, Tomm22, and Tomm22/40 KD in C2C12 cells. Arrowheads indicate mitochondrial fission events. Analysis of mitochondrial morphology using ImageJ software: (B) average mitochondrial length (nm) and (C) average mitochondrial width (nm). *n = 10-15* cells. (D) Mitochondrial fission (*Fis1/FIS1, Drp1/DNM1L*) and fusion

(*Mfn2/MFN2, Opa1/OPA1*) markers were quantified by qPCR in NTC, Tomm22, Tomm40, and Tomm22/40 KD C2C12 cells. (E) The experiment was conducted as in (D) but with hSkMC cells. (*n=3* biological replicates) (F) Mitochondrial density was quantified using MitoTracker™ Deep Red FM fluorescence probe to measure average fluorescence intensity and normalized to protein concentration by Bradford assay (n=10-12 biological replicates). (G) Relative mtDNA copy number levels were quantified and normalized to *B2m* transcript levels (nuclear DNA) by qPCR in siRNA transfected C2C12 cells ($n = 3$ biological replicates). All graphical and numeric data represent mean ± SEM. *$p<0.05$, **$p<0.01$, ***$p<0.001$, ****$p<0.0001$ vs. NTC by Student's t-test.

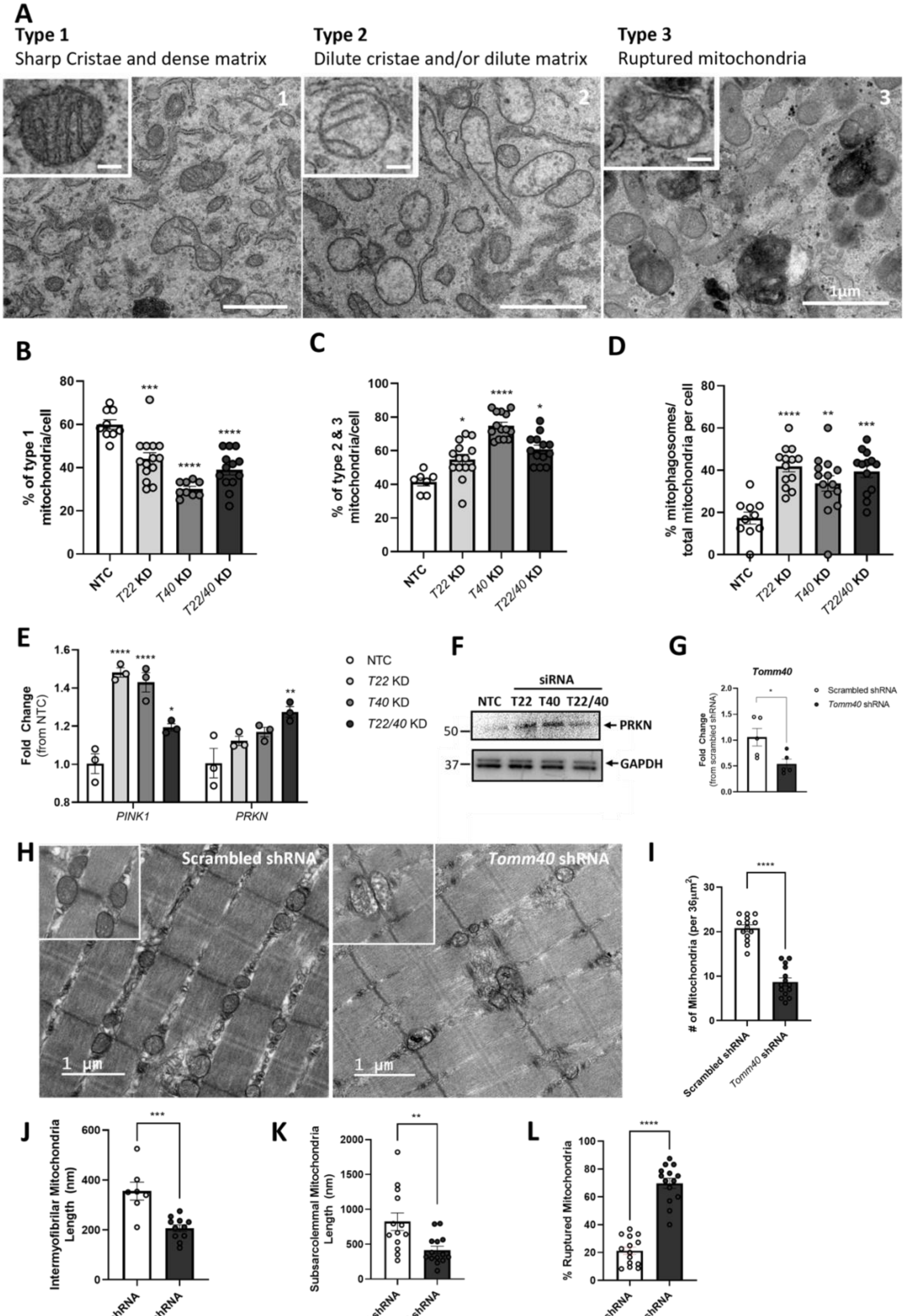
A
Type 1
Sharp Cristae and dense matrix
Type 2
Dilute cristae and/or dilute matrix
Type 3
Ruptured mitochondria
1
2
3
1μm
B
% of type 1 mitochondria/cell
NTC
T22 KD
T40 KD
T22/40 KD
***
****
****
C
% of type 2 & 3 mitochondria/cell
*
****
*
D
% mitophagosomes/ total mitochondria per cell
****
**
***
E
Fold Change (from NTC)
PINK1
PRKN
****
****
*
**
NTC
T22 KD
T40 KD
T22/40 KD
F
siRNA
NTC T22 T40 T22/40
50
37
PRKN
GAPDH
G
Tomm40
Fold Change (from scrambled shRNA)
Scrambled shRNA
Tomm40 shRNA
*
H
Scrambled shRNA
Tomm40 shRNA
1 μm
1 μm
I
# of Mitochondria (per 36μm²)
****
Scrambled shRNA
Tomm40 shRNA
J
Intermyofibrilar Mitochondria Length (nm)
***
K
Subsarcolemmal Mitochondria Length (nm)
**
L
% Ruptured Mitochondria
****

Figure 2-5. *TOMM40* and *TOMM22* knock-down, singly and in combination, promote mitochondrial damage and mitophagy in skeletal muscle *in vitro* and *in vivo*. (A) TEM micrographs of C2C12 myotubes representing Type 1 (healthy; A1 image of NTC), 2 (unhealthy; A2 image of *Tomm40* KD), and 3 (damaged/ruptured; A3 image of *Tomm22/40* KD) mitochondria (scale bars = 1μm; inset scale bars = 200nm). (B) Analysis of mitochondrial morphology and damage in NTC vs. KD C2C12 cells. Bar graph represents percent of cells exhibiting type 1 mitochondria. (C) Bar graph represents percent of type 2 and 3 mitochondria in NTC vs. KD C2C12 cells (*n = 10-15* cells). (D) Percent of mitophagosomes per total number of mitochondria per cell, identified from TEM images (*n = 10-15* cells). (E) mRNA transcript levels of *PINK1* and *PRKN* (mitophagy), were quantified using qPCR in NTC vs. KD hSkMC cells (*n = 3* biological replicates). (F) Representative western blot of PRKN protein expression in hSkMC compared to GAPDH control. (G) mRNA transcript levels of *Tomm40* (~50% knockdown) were quantified in gastrocnemius skeletal muscle of male mice injected with AAV8 scrambled vs. *Tomm40* shRNA (*n = 6*/group). (H) Representative TEM images of gastrocnemius muscle samples from scrambled vs. *Tomm40* shRNA (*n = 6*/group) male mice. (I) Bar graph represents average number of mitochondria within a surface area of 36 μm^2, (J) length of intermyofibrillar mitochondria (as seen in the TEM images), (K) length of sarcolemnal mitochondria (not shown), and (L) percent of ruptured mitochondria per 36 μm^2. All graphical and numeric data represent mean ± SEM. *$p<0.05$, **$p<0.01$, ***$p<0.001$, ****$p<0.0001$ vs. NTC or scrambled shRNA by Student's t-test.

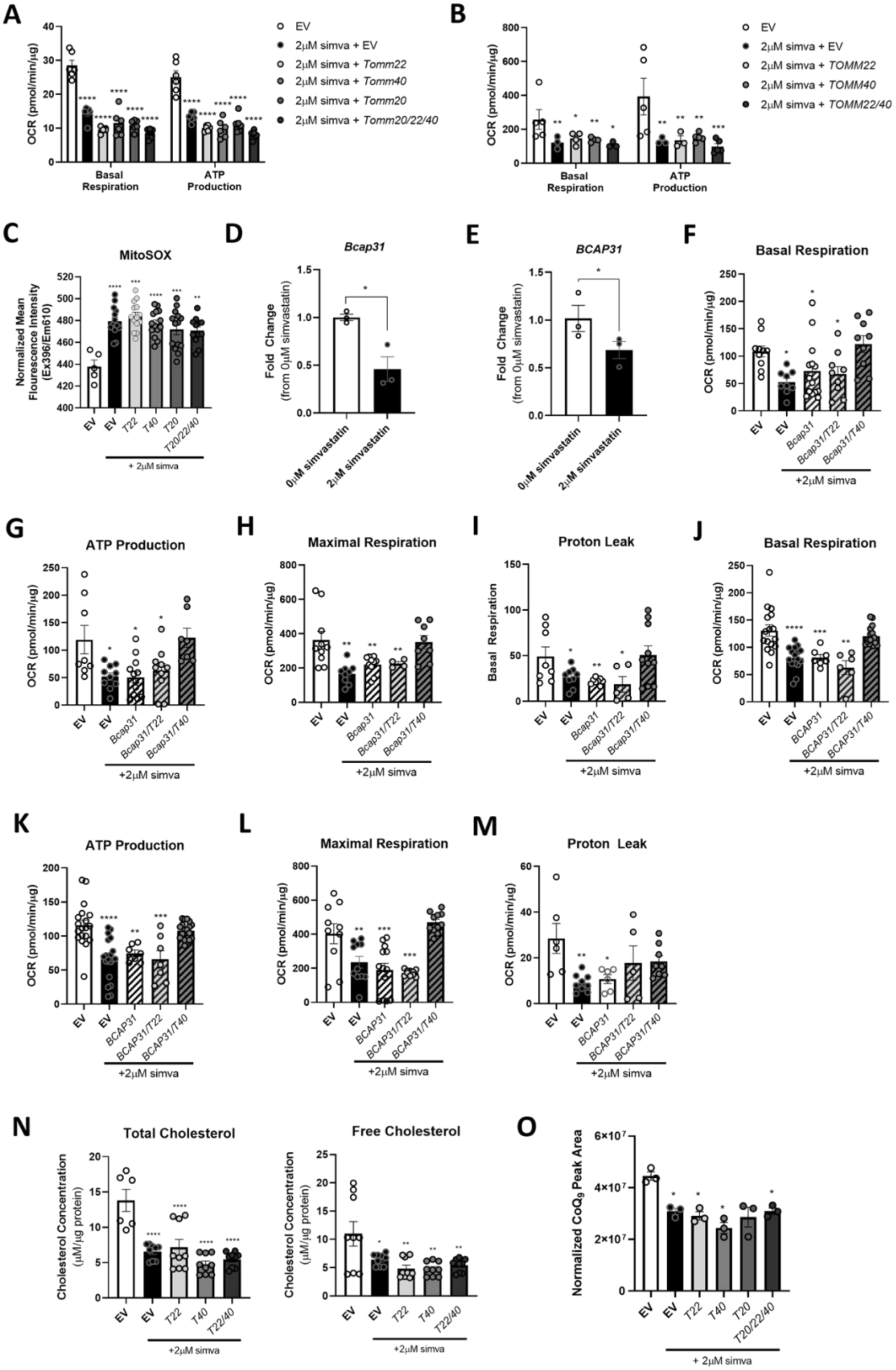
A
OCR (pmol/min/μg)
Basal Respiration
ATP Production
EV
2μM simva + EV
2μM simva + Tomm22
2μM simva + Tomm40
2μM simva + Tomm20
2μM simva + Tomm20/22/40
B
OCR (pmol/min/μg)
Basal Respiration
ATP Production
EV
2μM simva + EV
2μM simva + TOMM22
2μM simva + TOMM40
2μM simva + TOMM22/40
C
MitoSOX
Normalized Mean Flourescence Intensity (Ex396/Em610)
EV
EV
T22
T40
T20
T20/22/40
+ 2μM simva
D
Bcap31
Fold Change (from 0μM simvastatin)
0μM simvastatin
2μM simvastatin
E
BCAP31
Fold Change (from 0μM simvastatin)
0μM simvastatin
2μM simvastatin
F
Basal Respiration
OCR (pmol/min/μg)
EV
EV
Bcap31
Bcap31/T22
Bcap31/T40
+2μM simva
G
ATP Production
OCR (pmol/min/μg)
EV
EV
Bcap31
Bcap31/T22
Bcap31/T40
+2μM simva
H
Maximal Respiration
OCR (pmol/min/μg)
EV
EV
Bcap31
Bcap31/T22
Bcap31/T40
+2μM simva
I
Proton Leak
Basal Respiration
EV
EV
Bcap31
Bcap31/T22
Bcap31/T40
+2μM simva
J
Basal Respiration
OCR (pmol/min/μg)
EV
EV
BCAP31
BCAP31/T22
BCAP31/T40
+2μM simva
K
ATP Production
OCR (pmol/min/μg)
EV
EV
BCAP31
BCAP31/T22
BCAP31/T40
+2μM simva
L
Maximal Respiration
OCR (pmol/min/μg)
EV
EV
BCAP31
BCAP31/T22
BCAP31/T40
+2μM simva
M
Proton Leak
OCR (pmol/min/μg)
EV
EV
BCAP31
BCAP31/T22
BCAP31/T40
+2μM simva
N
Total Cholesterol
Cholesterol Concentration (μM/μg protein)
EV
EV
T22
T40
T22/40
+2μM simva
Free Cholesterol
Cholesterol Concentration (μM/μg protein)
EV
EV
T22
T40
T22/40
+2μM simva
O
Normalized CoQ9 Peak Area
6×10^7
4×10^7
2×10^7
EV
EV
T22
T40
T20
T20/22/40
+ 2μM simva

Figure 2-6. *TOMM40* and *BCAP31* overexpression rescues mitochondrial respiration, ATP production, and proton leak after simvastatin treatment of skeletal muscle cells. (A) OCR was measured in C2C12 cells treated with 2 µM simvastatin + empty vector or *Tomm22*, *Tomm40*, *Tomm20* (*T20*), or *Tomm20/22/40* expressing plasmids for 24-48 hrs. Basal respiration and ATP production determined from OCR analysis. (B) The same experiment was conducted in hSkMC cells treated with 2 µM simvastatin + empty vector or *TOMM22*, *TOMM40*, *TOMM22/40* expressing plasmids for 24-48 hrs. (*n = 10-15* biological replicate) (C) mitoROS was determined in C2C12 cells by quantifying mean mitoSOX™ fluorescence intensity and normalizing to total protein concentration using Bradford assay (*n = 10-12* biological replicates). mRNA transcripts of (D) *Bcap31* in C2C12 and (E) *BCAP31* in hSkMC myotubes without and with 2 µM simvastatin was quantified by qPCR. (F-I) Basal respiration, ATP production, maximal respiration, and proton leak was analyzed from OCR recordings in C2C12 cells treated with 2 µM simvastatin + empty vector or *Bcap31, Bcap31/Tomm22*, or *Bcap31/Tomm40* expressing plasmids for 24-48 hrs. (J-M) Basal respiration, ATP production, maximal respiration, and proton leak was analyzed from OCR recordings in hSkMC cells treated with 2 µM simvastatin + empty vector or *BCAP31, BCAP31/TOMM22*, or *BCAP31/TOMM40* expressing plasmids for 24-48 hrs. (N) Total and free cholesterol were quantified in mitochondria of C2C12 myotubes using Amplex Red Cholesterol Assay (*n = 3-6* biological replicates). (O) Total CoQ_9 was quantified from mitochondria isolated from C2C12 cells transfected with empty vector (control), 2 µM simvastatin + empty vector, *Tomm22*, *Tomm40*, *Tomm20*, or *Tomm20/22/40* expressing plasmids (*n* = 3 biological replicates). All values were normalized to protein concentration by BCA. All graphical and numeric data represent mean ± SEM. *$p<0.05$, **$p<0.01$, ***$p<0.001$, ****$p<0.0001$ vs. EV by Welch and Brown-Forsythe or one-way ANOVA, with post-hoc Student's t-test to identify differences between groups.

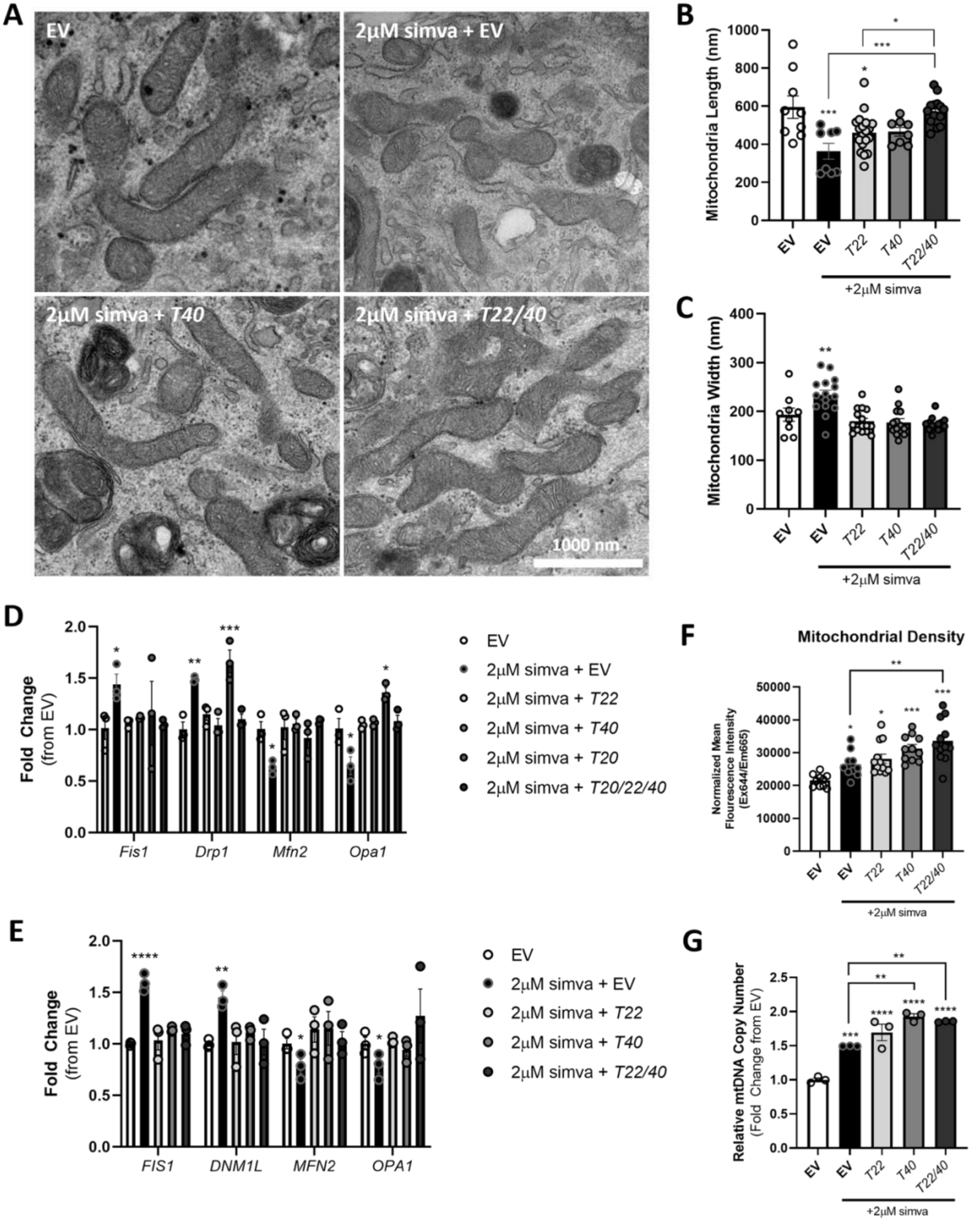

Figure 2-7. Overexpressing *TOMM40* and *TOMM22, singly and in combination,* suppresses statin-induced mitochondrial fission and promotes fusion in skeletal muscle cells. (A) Representative TEM images of mitochondrial morphology in C2C12 cells transfected with empty vector (EV), 2 μM simvastatin + EV, and *Tomm22, Tomm40*,

or *Tomm22/40* expressing plasmids. (B and C) Using ImageJ software analysis in conjunction with the TEM images in (A), average mitochondrial length and width (nm) were measured (*n = 10-15* cells). (D) Mitochondrial fission (*Fis1/FIS1, Drp1/DNM1L*) and fusion (*Mfn2/MFN2, Opa1/OPA1*) markers were quantified by qPCR in EV and 2 µM simvastatin + EV, *Tomm22, Tomm40*, *Tomm20*, and *Tomm20/22/40 (T20/22/40)* overexpressing C2C12 cells. (E) The same experiment was conducted as in (D) but with hSkMC cells. (*n=3* biological replicates) (F) Mitochondrial density was quantified using MitoTracker™ Deep Red FM fluorescence probe to measure average fluorescence intensity and normalized to protein concentration by Bradford assay (n=10-12 biological replicates). (G) Relative mtDNA copy number levels were quantified and normalized to *B2m* transcript levels (nuclear DNA) by qPCR in siRNA transfected C2C12 cells (*n = 3* biological replicates). All graphical and numeric data represent mean ± SEM. **$p<0.05$*, ***$p<0.01$*, ****$p<0.001$*, *****$p<0.0001$*. One-way ANOVA, with post-hoc Student's t-test to identify differences between groups was performed.

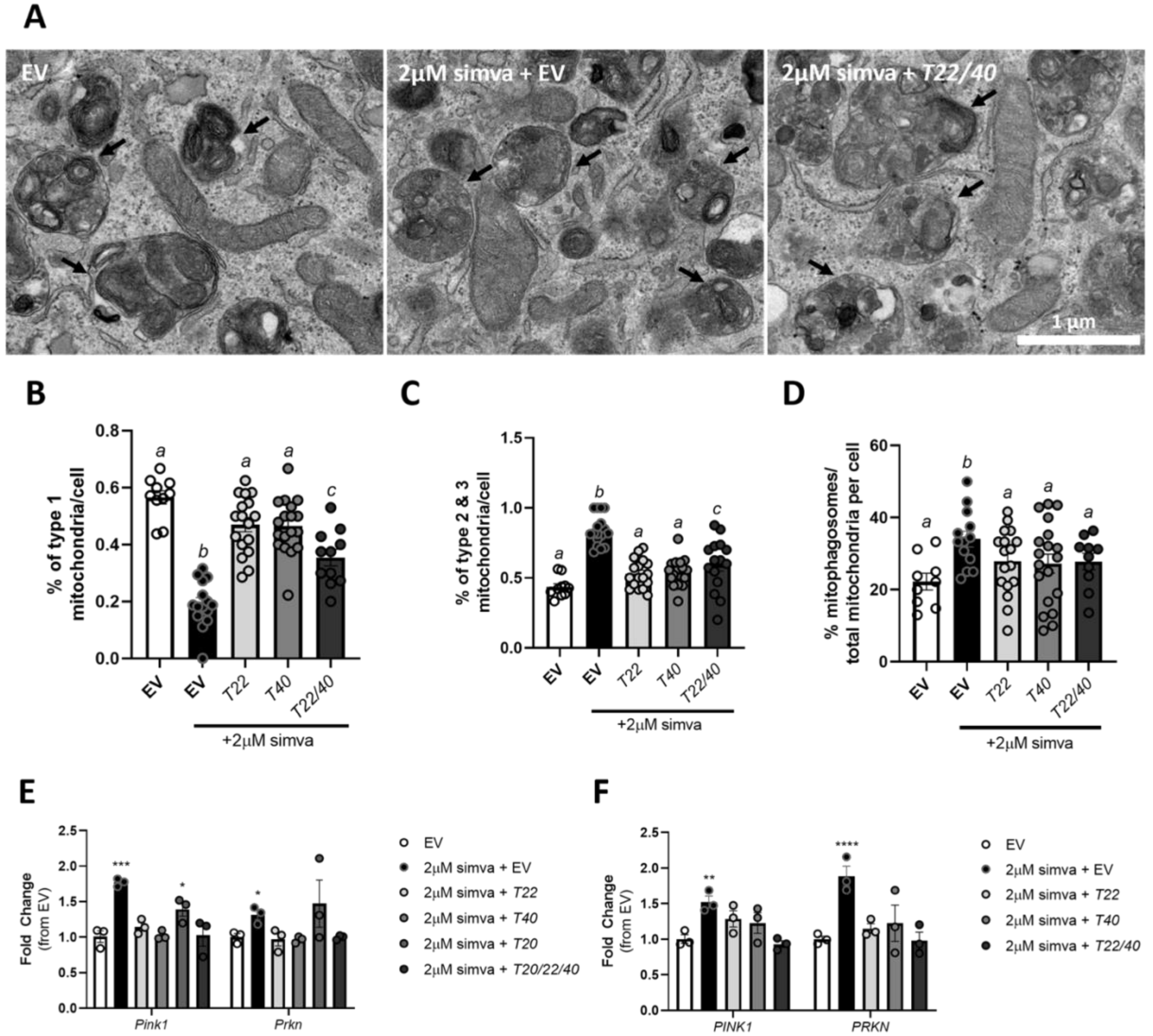

Figure 2-8. Overexpression of *TOMM40* and *TOMM22*, but not *TOMM20*, rescues simvastatin-induced mitophagy leading to reduced mitochondrial damage. (A) TEM micrographs of mitophagosomes found in EV, 2 µM simvastatin + EV, and 2 µM simvastatin + *Tomm22/Tomm40* overexpressing C2C12 cells. Arrowheads indicate mitophagosomes. (B) Analysis of mitochondrial morphology and damage in EV or 2 µM simvastatin + EV, *T22, T40*, or *T22/40* overexpression in C2C12 cells. Bar graph represents percent of cells exhibiting type 1 mitochondria. (C) Bar graph represents percent of type 2 and 3 mitochondria in EV or 2 µM simvastatin + EV, *T22, T40*, or *T22/40* overexpression in C2C12 cells (*n = 10-15* cells). (D) Percent of mitophagosomes per total number of mitochondria per cell, identified from TEM images (*n = 10-15* cells). (E-F) mRNA transcript levels of *Pink1/PINK1* and *Prkn/PRKN* (mitophagy), were quantified using qPCR in EV vs. 2 µM simvastatin + EV, *TOMM22, TOMM40, TOMM20*, or *TOMM20/22/40* in (E) C2C12 and (F) hSkMC myotubes (*n = 3* biological replicates). All graphical and numeric data represent mean ± SEM. *$p<0.05$, **$p<0.01$, ***$p<0.001$,

****$p<0.0001$ vs. EV by one-way ANOVA, with post-hoc Student's t-test to identify differences between groups.

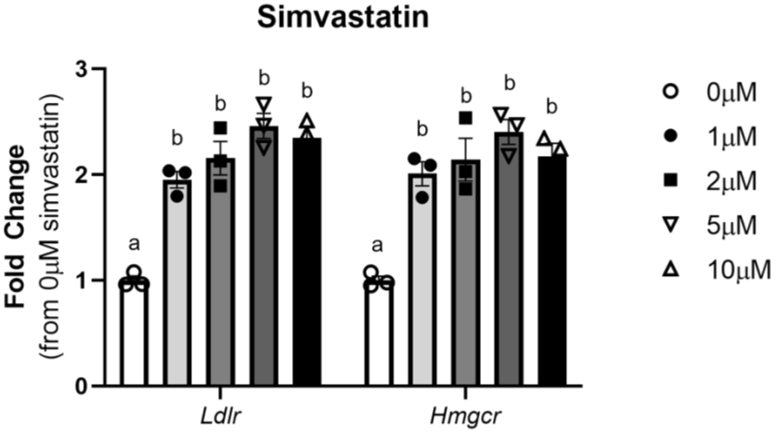

Figure 2-S1. Simvastatin treatment of C2C12 myotubes upregulates *Ldlr* and *Hmgcr* mRNA transcripts in a dose-dependent manner. Differentiated C2C12 myotubes were treated with 0, 1, 2, 5 or 10 μM simvastatin for 48 hrs. All numeric data represent mean ± SEM. *$p<0.05$, **$p<0.01$, ***$p<0.001$, ****$p<0.0001$ vs. NTC by Student's t-test. ($n = 3$ biological replicates)

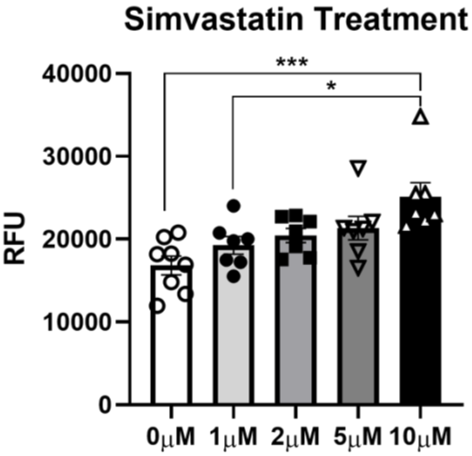

Figure 2-S2. Dose-dependent cell apoptosis identified in C2C12 myotubes. Differentiated C2C12 myotubes were treated with 0, 1, 2, 5 or 10 μM simvastatin for 48 hrs and apoptosis was assessed using an EarlyTox Caspase-3/7 colorimetric detection kit with a spectrophotometer. RFU = relative fluorescence units. All numeric data represent mean ± SEM. *$p<0.05$, ***$p<0.001$ vs. NTC by Student's t-test. ($n = 6\text{-}12$ biological replicates)

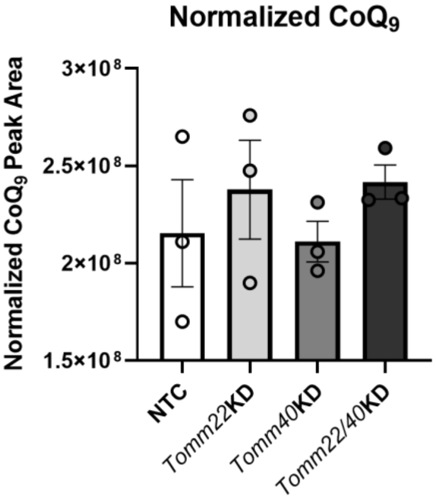

Figure S3. Effects of *Tomm40* and *Tomm22* knockdown on CoQ levels in C2C12 whole cell lysates. CoQ9 from whole cell lysates of NTC, *Tomm40, Tomm22*, and *Tomm22/40* KD C2C12 skeletal myotubes. All values were normalized to protein concentration. All numeric data represent mean ± SEM. Welch and Brown-Forsythe ANOVA was performed. (*n = 3* biological replicates)

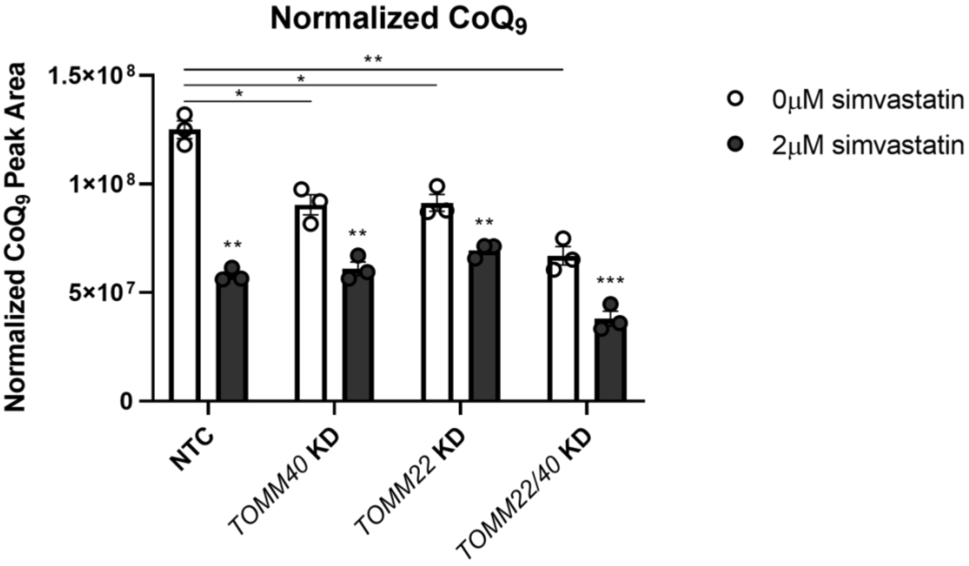

Figure S4. Simvastatin treatment further decreases CoQ levels in *Tomm40* and *Tomm22* KD C2C12 mitochondria. (A)Total CoQ$_9$ from isolated mitochondria of NTC, *Tomm40, Tomm22*, and *Tomm22/40* KD C2C12 skeletal myotubes treated with simvastatin (2 μM). All values were normalized to protein concentration. All numeric data represent mean ± SEM. *$p<0.05$, **$p<0.01$, ***$p<0.001$, ****$p<0.0001$ vs. 0μM simvastatin by Welch and Brown-Forsythe ANOVA. (*n = 3* biological replicates)

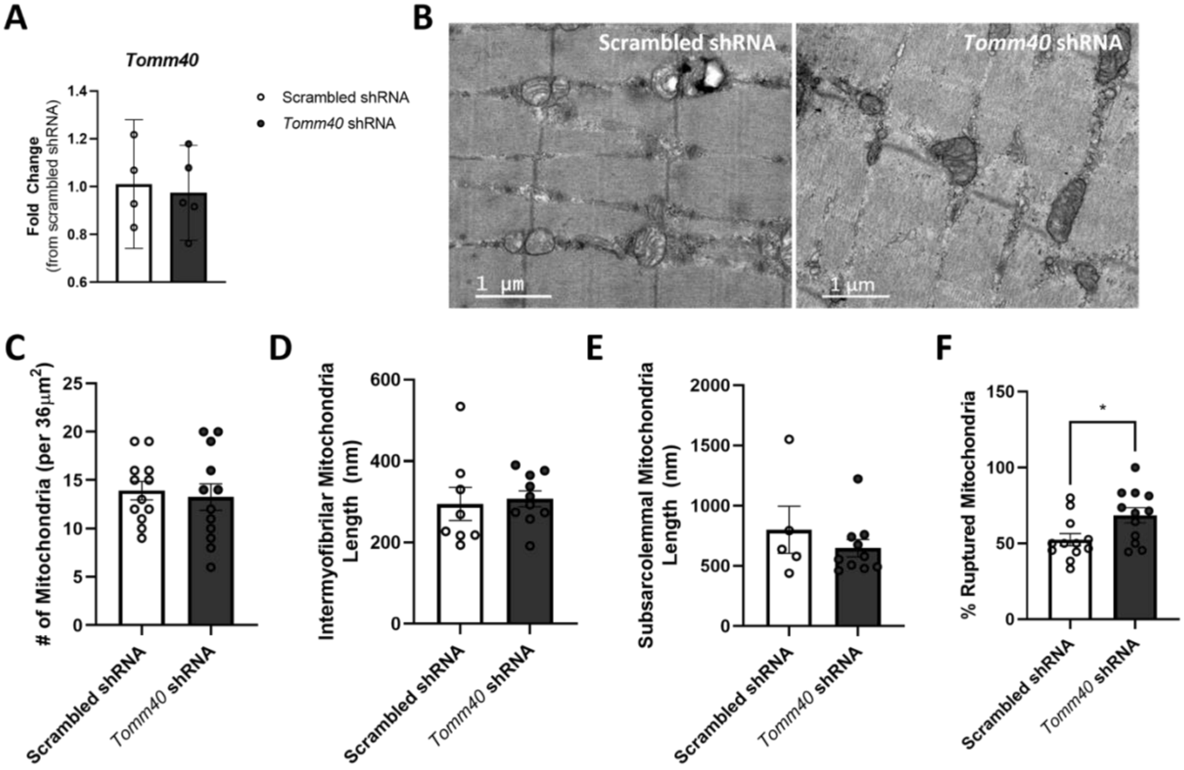

Figure S5. Female C57BL/6J mice injected with AAV8-*Tomm40* shRNA do not show knockdown of *Tomm40* or differences in mitochondrial number and morphology, compared to scrambled shRNA control. (A) Female mice IP injected with AAV8 scrambled vs. *Tomm40* shRNA do not show difference in *Tomm40* mRNA transcripts in gastrocnemius muscle tissues by qPCR ($n = 6$/group). (B) Representative TEM images of gastrocnemius muscle samples from scrambled vs. *Tomm40* shRNA ($n = 6$/group) female mice. (C) Bar graph represents average number of mitochondria within a surface area of 36 μm^2, (D) length of intermyofibrillar mitochondria (as seen in the TEM images), (E) length of sarcolemnal mitochondria (not shown), and (F) percent of ruptured mitochondria per 36 μm^2. All numeric data represent mean ± SEM. *$p<0.05$ vs. scrambled shRNA by Welch and Brown-Forsythe ANOVA.

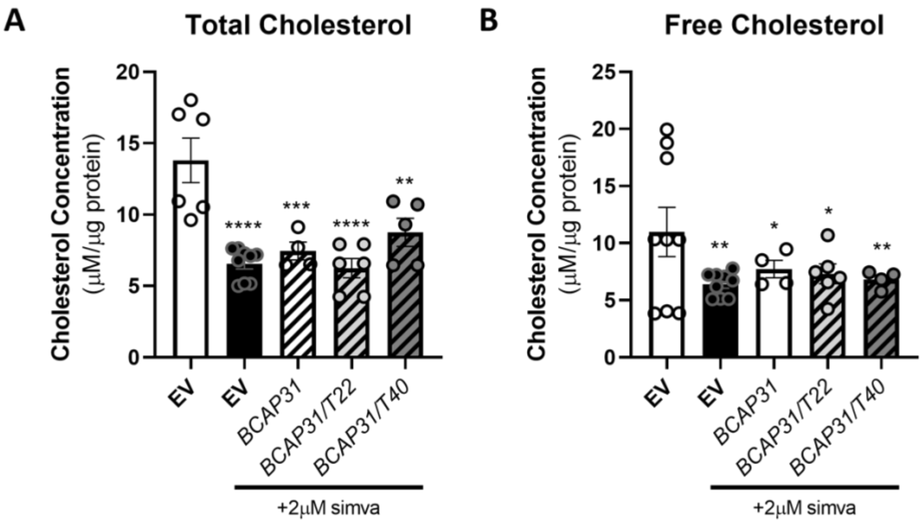

Figure S6. *BCAP31* and *TOMM40* or *TOMM22* overexpression does not rescue intracellular cholesterol levels in simvastatin-treated hSkMC myotubes. (A) Total and (B) free cholesterol were quantified in mitochondria of C2C12 myotubes using Amplex Red Cholesterol Assay (*n = 6-12* biological replicates). All numeric data represent mean ± SEM. **p<0.05, **p<0.01, ***p<0.001, ****p<0.0001* vs. EV (without statin) by Welch and Brown-Forsythe ANOVA.

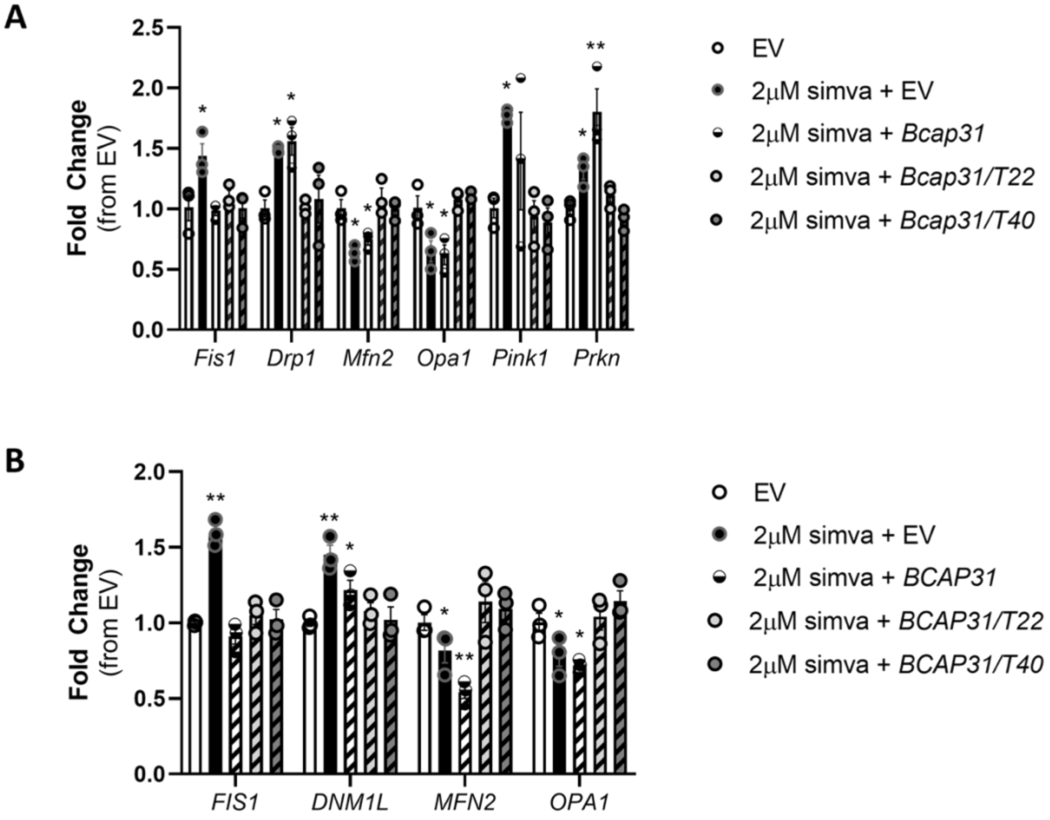

Figure S7. Overexpression of *BCAP31* recues *FIS1* gene expression in simvastatin-treated skeletal myotubes. (A) Mitochondrial fission (*Fis1/FIS1, Drp1/DNM1L*) and fusion (*Mfn2/MFN2, Opa1/OPA1*) markers were quantified by qPCR in EV and 2 µM simvastatin + EV, *Bcap31*, Bcap31/*T22,* and *Bcap31/T40* overexpressing C2C12 cells. (B) The same experiment was conducted as in (A) but with hSkMC cells. (*n=3* biological replicates). All graphical and numeric data represent mean ± SEM. **p<0.05*, ***p<0.01* vs. EV (without statin) by one-way ANOVA, with post-hoc Student's t-test to identify differences between groups.

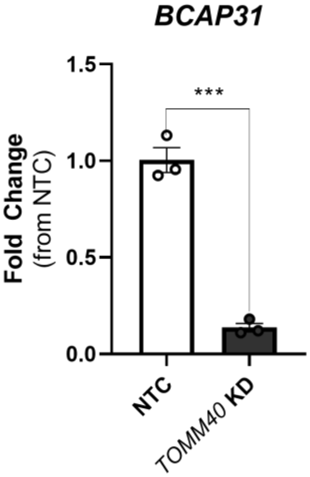

Figure S8. *TOMM40* knockdown downregulates *BCAP31* gene expression in hSkMC myotubes. mRNA transcripts show a reduction by ~85% by qPCR of *BCAP31* in differentiated hSkMC myotubes transfected with *TOMM40* siRNA for 48 hrs. (*n=3* biological replicates) Graphical data represent mean ± SEM. ****p<0.001* vs. NTC by one-way ANOVA, with post-hoc Student's t-test to identify differences between groups.

TRANSITION

In the previous chapter, we established TOMM40 and TOMM22 as mediators of statin-disrupted mitochondrial function and dynamics in differentiated skeletal myotubes. Interestingly, we also found *TOMM40* knock-down to alter intracellular cholesterol levels in skeletal myotubes. Furthermore, previous studies have revealed SNPs within TOMM40 and APOE in linkage disequilibrium to be associated to plasma lipid levels. Thus, beyond the scope of statins and the mitochondria, we were next interested in whether TOMM40 may affect cholesterol and lipid metabolism.

In Chapter 3, we explored the role of TOMM40 in regulating cholesterol and lipid metabolism in the liver, *in vitro* and *in vivo*. We identified the changes in hepatocellular cholesterol and triglyceride content, and plasma lipid levels, were due primarily to *TOMM40* KD-induced disruption of MERCs, leading to upregulation of LXR activity and increased *APOE* and *LDLR* expression.

CHAPTER 3: TOMM40 regulates hepatocellular and plasma lipid metabolism via an LXR-dependent pathway

Neil V Yang*, Justin Y Chao, Kelly A Garton, Tommy Tran, Sarah M King, Joseph Orr, Jacob H Oei, Alexandra Crawford, Misun Kang, Reena Zalpuri, Danielle Jorgens, Pranav Konchadi, John S Chorba, Elizabeth Theusch, Ronald M Krauss

Published in bioRxiv, doi: https://doi.org/10.1101/2024.06.27.600910

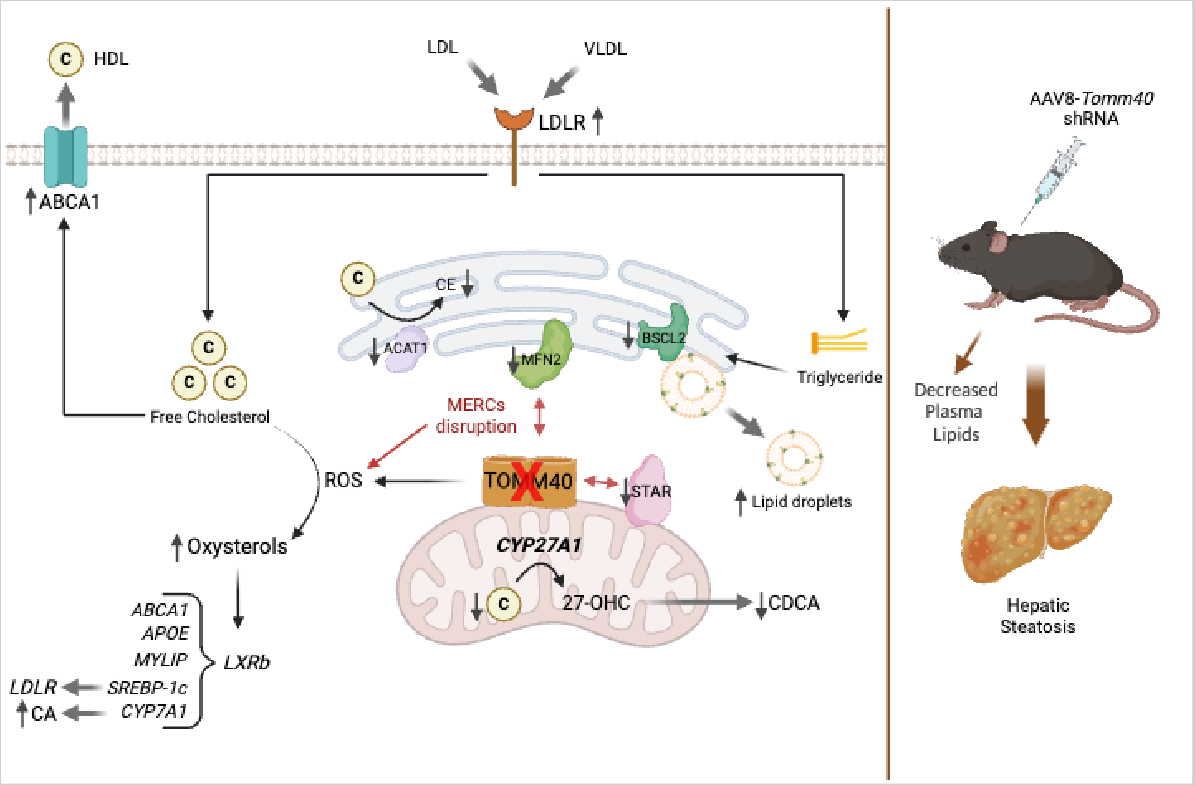

Figure 3.0 Graphical Abstract

3.1 Summary

The gene encoding TOMM40 (Transporter of Outer Mitochondrial Membrane 40) is adjacent to that encoding APOE, which has a central role in lipid and lipoprotein metabolism. Human genetic variants near *APOE* and *TOMM40* are strongly associated with plasma lipid levels, but a specific role for TOMM40 in lipid metabolism has not been established. Investigating this, we show that suppression of *TOMM40* in human hepatoma cells upregulates expression of *APOE* and *LDLR* in part via activation of LXRB (NR1H2) by oxysterols, with consequent increased uptake of VLDL and LDL. This is in part due to disruption of mitochondria-endoplasmic reticulum contact sites, with resulting accrual of reactive oxygen species and non-enzymatically derived oxysterols. With *TOMM40* knockdown, cellular triglyceride and lipid droplet content are increased, effects attributable in part to receptor-mediated VLDL uptake, since lipid staining is significantly reduced by concomitant suppression of either *LDLR* or *APOE*. In contrast, cellular cholesterol content is reduced due to LXRB-mediated upregulation of the ABCA1 transporter as well as increased production and secretion of oxysterol-derived cholic acid. Consistent with the findings in hepatoma cells, *in vivo* knockdown of *TOMM40* in mice results in significant reductions of plasma triglyceride and cholesterol concentrations, reduced hepatic cholesterol and increased triglyceride content, and accumulation of lipid droplets leading to development of steatosis. These findings demonstrate a role for TOMM40 in regulating hepatic lipid and plasma lipoprotein levels and identify mechanisms linking mitochondrial function with lipid metabolism.

3.2 Introduction

TOMM40 (translocase of outer mitochondrial membrane 40) is the main channel-forming subunit of the translocase of the outer mitochondrial membrane (TOM) complex (**Fig 1A**). This complex is required for the transport of precursor proteins into the mitochondria to maintain mitochondrial function[19]. Furthermore, TOMM40 has been shown to interact with key regulators of mitochondrial function such as BAP31[39], affect calcium signalling via its interaction with VDAC channels (voltage dependent anion channels)[41-43], and have effects at mitochondria-ER contact sites (MERCs) that impact mitochondrial cholesterol transport via steroidogenic acute regulatory protein (STAR aka STARD1)[33,40]. In mouse Leydig cells, the absence of TOMM40 causes STAR to lose its ability as a cholesterol transporter, depleting mitochondrial cholesterol content[117].

The *TOMM40* gene shares the same locus on chromosome 19q as *APOE,* a gene with a key role in cholesterol and lipoprotein metabolism[118,119]. Importantly, APOE acts as a key ligand for low-density lipoprotein receptor (LDLR) to transport lipoproteins into the liver[120]. Genome-wide association studies have revealed multiple genetic variants in a haplotype block encompassing *TOMM40* and *APOE* that are associated with plasma lipid levels[121,122]. However, a specific role for TOMM40 in regulation of hepatic lipid and plasma lipoprotein metabolism has not previously been determined, and the present study was aimed at testing this possibility.

3.3 Results

3.3.1 Loss of hepatic *TOMM40* disrupts mitochondrial function and mitochondria-ER contact sites (MERCs)

Consistent with prior studies in HeLa cells and *C. Elegans*[21,22], knockdown (KD) of *TOMM40* in human hepatoma HepG2 cells (**Fig 1B**) resulted in reduction of basal and maximal respiration and ATP production as well as proton leak (**Fig 1D-H**) compared to non-targeting control (NTC). The impact of *TOMM40* KD on mitochondrial function was also manifested by an increase in cellular reactive oxygen species (ROS) (**Fig 1I**), consistent with effects reported in epithelial ovarian cancer cells[72].

Notably, there was an increase of calcium ions (Ca^{2+}) in the ER lumen with *TOMM40* KD, suggesting a block in the transfer of Ca^{2+} ions from ER to mitochondria (**Fig 1J**), likely due to a reduction in expression of VDACs (voltage-dependent anion channels) that import Ca^{2+} into mitochondria[123] (**Fig 1K**). This finding, in conjunction with previous evidence that TOMM40 interacts directly with BAP31 at mitochondria-ER contact sites (MERCs) in U2OS osteosarcoma cells[39], led us to test the effect of *TOMM40* on MERCs in HepG2 cells. Transmission electron microscopy (TEM; **Fig 1L**) revealed disruption of MERCs through a significant increase in ER-mitochondria distance (**Fig 1M**), decrease in length of MERCs (**Fig 1N**), and percentage of mitochondria with ER contacts (**Fig 1O**). Consistent with these effects, *TOMM40 KD* resulted in decreased protein expression of mitofusin 1 and 2 (MFN1 and MFN2) which play roles in tethering ER to mitochondria and maintaining MERCs[124], as well as reduced *MFN2* gene expression (**Fig 1P-Q**). Many studies have shown suppression of *MFN2* to result in disruption of MERCs as assessed by electron microscopy in various human cell lines[125-127]. Thus, we further demonstrated that disruption of MERCs by KD of *MFN2*, with a knock-down efficiency of ~90% (**Fig 1C**), reduced mitochondrial oxidative phosphorylation (**Fig 1E-H**) and increased cellular ROS to a similar extent as seen with *TOMM40* KD, and that with their combined KD, no further increase occurred (**Fig 1I**). Taken together, these results show that TOMM40 is a key regulator of mitochondrial function and MERCs and suggest that MERC disruption mediates the reduction in mitochondrial function and the increase in cellular ROS by *TOMM40* KD.

3.3.2 *TOMM40* KD promotes production of oxysterols and upregulation of LXR gene targets

In addition to the increase in ROS induced by *TOMM40* KD in HepG2 cells, we observed increased levels of several cholesterol oxidation products. While oxysterols generated from ROS, such as 7-ketocholesterol, were elevated (**Fig 2A**), we also saw an increase in those produced by enzymatic reactions, namely 25- and 24(S)-

hydroxycholesterol (OHC; **Fig 2B-C**). In addition, gene expression of *CYP3A4*, which encodes the rate limiting enzyme for generating 4β-hydroxycholesterol, also increased in the *TOMM40* KD cells (**Fig 2D**). Oxysterols are potent activators of the LXRA and LXRB transcription factors[128], and therefore we next tested whether *TOMM40* KD in HepG2 cells resulted in increased expression of the LXRs and their downstream gene targets. We observed that *TOMM40* KD induced a significant increase in gene expression of *LXRB* (aka *NR1H2*)**,** but not *LXRA* (aka *NR1H3*) (**Fig 2E**), suggesting *TOMM40* KD and its downstream ligands favor the LXRB isoform. Consistent with both LXR activation and increased *LXRB* expression, we found that transcripts of five LXR-regulated genes involved in lipid metabolism (*APOE, ABCA1, CYP7A1*, *F2BF1c,* and *MYLIP*) were significantly upregulated by *TOMM40* KD (**Fig 2F-J)**. Moreover, addition of exogenous 25-OHC to NTC-treated cells to induce LXR activation yielded effects consistent with those of *TOMM40* KD, implying an oxysterol-dependent mechanism (**Fig 2K-L**). Interestingly, double KD of *TOMM40* together with either *LXRA* or *LXRB* resulted in a reciprocal increase of the other isoform, thus maintaining relatively constant total *LXR* gene expression (**Fig S1**). Such a compensatory mechanism between the two isoforms has been reported previously[129]. We therefore tested the effects of *TOMM40* KD on expression of the five LXR target genes in conjunction with inhibition of both *LXRA* and *LXRB* by GSK2033, an LXR antagonist with high binding affinity for LXRA and LXRB, and found that all were reduced to levels similar to those seen with NTC (**Fig 2F-J**). Together, these results indicate that suppression of *TOMM40* upregulates expression of LXR target genes both by oxysterol activation of LXR and upregulation of *LXRB* to a greater extent than *LXRA*.

Moreover, we found that *MFN2* KD also upregulated expression of *LXRB* (**Fig 2M**) and LXR target genes (**Fig 2N**) similar to *TOMM40* KD, and increased cellular concentration of 7-ketocholesterol (**Fig 2A**) and *CYP3A4* expression (**Fig 2D**), but not enzymatic-derived oxysterols (**Fig S2**). This suggests that ROS-derived 7-ketocholesterol is a key ligand driving LXR activity via disruption of MERCs in both *MFN2* KD and *TOMM40* KD HepG2 cells.

3.3.3 *TOMM40* KD increases LDLR gene expression and receptor-mediated LDL hepatic uptake

Notably, we found that in addition to the known LXR transcriptional targets, *LDLR* gene expression in HepG2 cells was also increased by *TOMM40* KD (**Fig 3A**), as were cellular LDLR protein content (**Fig 3B**), and cell surface LDLR (**Fig 3C**). Furthermore, the increase of *LDLR* was reversed by addition of GSK2033, indicating a role for LXRs in *LDLR* regulation (**Fig 3A**). Expression of *SREBF2*, the canonical transcriptional regulator of *LDLR*, was unaffected by *TOMM40* KD, consistent with unaffected transcript levels of *HMGCR* (**Fig S3**), another downstream target of SREBF2. However, we found that *TOMM40* KD-induced upregulation of *LDLR* gene expression was suppressed by concurrent KD of *SREBF1c*, a known transcriptional target of LXR[130] and splice variant of *SREBF1*(**Fig 3D**). Moreover, gene expression of *LDLR* (but not *HMGCR*) was suppressed by *SREBF1c* KD alone **(Fig 3D).**

To further assess the transcriptional relationship between *SREBF1c* and *LDLR* expression with *TOMM40* KD, we transiently expressed luciferase constructs containing the native *LDLR* promoter with and without the *LDLR* 3'UTR in *TOMM40* KD HepG2 cells (**Fig 3E**). While *TOMM40* KD alone increased LDLR promoter activity, this returned to normal in the presence of GSK2033 or *SREBF1c* KD (**Fig 3F**). No differences in activity were observed between constructs fused to the LDLR promoter + 3'UTR coding sequence vs. the LDLR promoter alone. Furthermore, we showed no effect of *TOMM40* KD on *LDLR* mRNA decay rate and stability after 4 hrs treatment with 1μg/mL of Actinomycin D (**Fig 3G**). Taken together, these results indicate thar the upregulation of *LDLR* transcript by *TOMM40* KD is mediated by LXR-driven expression of *SREBF1c* targeting the *LDLR* promoter region.

We next demonstrated that *TOMM40* KD increased LDL uptake in HepG2 cells (**Fig 3H**), and that this effect was blocked by KD of either *LDLR* or *APOE*, indicating that it is likely due to increased expression of these genes via LXR activation. Moreover, we showed that KD of *SREBF1c* inhibited the increase in LDL uptake by *TOMM40* KD to an extent similar to that of its reduction by *LDLR* KD, adding evidence for an LXR – SREBF1c – *LDLR* mechanism (**Fig 3I**). Unexpectedly however, *TOMM40* KD markedly decreased content of intracellular cholesterol (free and esterified) (**Fig 3L-N**). Notably, KD of *ABCA1*, which encodes a transporter responsible for cellular cholesterol efflux and is a transcriptional target of LXR, (**Fig 3K)** resulted in restoration of cellular (total and free) cholesterol content in *ABCA1/TOMM40* KD HepG2 cells (**Fig 3L-N**). Moreover, with *TOMM40* KD there was reduced gene expression of *ACAT1* (**Fig 3J**) which encodes the enzyme required for esterification of free cholesterol[131]. Therefore, through LXR activation and upregulation of LXRB, *TOMM40* KD promotes LDL uptake, but in parallel increases cholesterol efflux via ABCA1 and reduces ACAT1-mediated cholesterol esterification, resulting in reduced intracellular cholesterol levels.

3.3.4 Loss of *TOMM40* expression promotes the classic bile acid synthesis pathway, while inhibiting the alternative pathway via STAR

Since oxysterols serve as precursors of bile acid synthesis, we tested whether *TOMM40* KD-induced increases in oxysterol levels resulted in increased total bile acid secretion in HepG2 cells[132]. While we found a greater amount in the media of *TOMM40* KD vs. NTC cells (**Fig 4A**), there was no change in intracellular levels (**Fig 4B**). We then measured cellular content of the two major bile acids: cholic acid (CA) and chenodeoxycholic acid (CDCA) of the classical and alternative bile synthesis pathways, respectively[133], and found that *TOMM40* KD increased the level of CA in both cells (**Fig 4C**) and media (**Fig 4D**), whereas it decreased intracellular CDCA (**Fig 4E,F**), and this was primarily responsible for no net change in total intracellular bile acids. The effect on CA is consistent with our finding that *TOMM40* KD upregulates LXR-mediated expression of *CYP7A1*, which encodes the rate-limiting enzyme in the classic bile acid synthesis pathway[134]. These results indicate that the increase in total bile acid synthesis and secretion with *TOMM40* KD is driven at least in part by CYP7A1 of the classic bile acid synthesis pathway.

To assess the basis for reduced cellular CDCA content with *TOMM40* KD, we measured expression of *CYP27A1*, which encodes 27-cholesterol hydroxylase, the first enzyme in the alternative bile acid pathway that converts cholesterol into 27-OHC in the inner mitochondrial membrane[135]. Surprisingly, we found that its mRNA expression was increased by *TOMM40* KD (**Fig 4H**) whereas both mitochondrial cholesterol content (**Fig 4I,J**) and 27-OHC cellular levels (**Fig 4K**) were reduced, thus providing an explanation for the reduction in cellular CDCA, the downstream product of 27-OHC, despite upregulation of *CYP27A1* transcripts. In *MFN2* KD HepG2 cells, 27-OHC levels were also significantly reduced, suggesting reduction in 27-OHC and CDCA to be mediated by MERCs (**Fig S4**). Having observed depletion of mitochondrial cholesterol content, we next assessed the role of STAR (aka STARD1), a mitochondrial cholesterol transporter located at MERCs[136], and found that its gene expression was suppressed in *TOMM40* KD HepG2 cells (**Fig 4G**). Moreover, overexpression of *STAR* rescued the reduction of mitochondrial cholesterol content by *TOMM40* KD (**Fig 4I,J**) and increased cellular levels of 27-OHC (**Fig 4K**) and CDCA (**Fig 4L**) levels similar to those seen with NTC. Furthermore, *STAR* overexpression reversed the upregulation of *CYP27A1* gene expression by *TOMM40* KD in HepG2 cells (**Fig 4H**). These findings demonstrate that the interaction between TOMM40 and STAR at MERCs plays a role in regulating mitochondrial cholesterol content and that depletion of mitochondrial cholesterol content by *TOMM40* KD suppresses the alternative bile acid synthesis pathway.

3.3.5 Effects of *TOMM40* KD on hepatic triglyceride metabolism

In contrast to the depletion of cholesterol by *TOMM40* KD in HepG2 cells, we found that triglyceride content was significantly increased (**Fig 5A**). We therefore tested the effect of *TOMM40* KD on VLDL uptake and showed an increase that was prevented by *LDLR* suppression, similar to what was observed for LDL uptake (**Fig 5B**). We further assessed the effect of *TOMM40* KD on expression of other receptors involved in hepatic VLDL uptake and showed upregulation of *SDC1 and LRP1*, but not *VLDLR* (**Fig 5C**). Unlike the *LDLR* KD results, KD of *TOMM40* in combination with KD of either *SDC1* or *LRP1* did not reduce VLDL uptake (**Fig 5D**). Moreover, only the *TOMM40* and *LDLR* double KD cells showed a significant reduction in intracellular triglyceride levels (**Fig 5E**).

We also considered the possibility that an increase in triglyceride synthesis may contribute to its cellular accumulation with *TOMM40* KD. However, KD of the genes encoding DGAT1 (**Fig 5F**) and DGAT2 (**Fig 5G**), enzymes with key roles in triglyceride synthesis, resulted in no significant reduction in triglyceride content of *TOMM40* KD cells (**Fig 5H**). Additionally, when cultured in lipoprotein deficient media, *TOMM40* KD HepG2 cells showed no increase in intracellular triglyceride content compared to NTC, confirming that VLDL uptake from the media plays a determining role in the accumulation of cellular triglyceride in HepG2 cells (**Fig 5H**). Finally, we showed that transcript levels of *MTTP, TM6SF2*, and *PPARGC1B,* which encode genes that have critical roles in regulating VLDL assembly and secretion[137,138], were not increased by *TOMM40* KD (**Fig 5I**). We therefore conclude that increased VLDL uptake resulting from upregulation of *LDLR* is primarily responsible for the cellular triglyceride loading induced by *TOMM40* KD.

3.3.6 Plasma cholesterol and triglyceride levels are reduced in AAV8-*Tomm40* shRNA C57BL/6J mice

We suppressed *Tomm40* expression with intraperitoneal (IP) injection of AAV8-*Tomm40* shRNA, which has strong tropism to liver cells[139], in C57BL/6J male and female mice fed a western diet (0.15% cholesterol, 21% fat), achieving a KD efficiency in liver of greater than 60%. (**Fig 6A**). After 5 weeks, there were significant reductions in body weight that correlated with percent KD, however no changes were seen in food intake (**Fig S5**). TEM (transmission electron microscopy) of hepatic tissue sections from *Tomm40* KD male, but not female, mice demonstrated disruption of MERCs. (**Fig 6B-D, Fig S6**). Further results also consistent with those described above for *TOMM40* KD in HepG2 cells included reduced hepatic expression of *Mfn2* and increased expression of *Lxrb, Abca1, Cyp7a1, Srebf1c,* and *Ldlr* in both male and female mouse livers, though only males showed increased expression of *Apoe* (**Fig 6E,F**). Similar effects were observed in primary hepatocytes from 8-12-week old male mice transfected with *Tomm40* siRNAs *in vitro* (**Fig 6H**). Finally, plasma CA was higher in the *Tomm40* shRNA mice compared to controls though this was seen only in males (**Fig 6G**).

In vivo Tomm40 KD resulted in substantially lower plasma concentrations of total cholesterol, non-HDL cholesterol, triglycerides, and HDL cholesterol, albeit to a lesser extent in female than in male mice, in which levels of all these measures with scrambled shRNA treatment were significantly higher than in females. (**Fig 6I**). These findings were supported by measurements of lipoprotein particle concentrations using ion mobility methodology (**Fig S7**). Notably, we also found decreased hepatic cholesterol content (**Fig 6J-L**) in male mice, and increased triglyceride content (**Fig 6M**) in both sexes, as was seen in our *in vitro* experiments in HepG2 cells.

3.3.7 *TOMM*40 KD induces lipid droplet accumulation and metabolic-dysfunction associated steatotic liver disease (MASLD)

Consistent with the increased triglyceride content of *TOMM40* KD HepG2 cells, TEM micrographs revealed an increase in lipid droplet (LD) number and size (**Fig 7B,C**), and further cytometric examination showed greater Nile red fluorescence than in NTC treated cells (**Fig 7D,E**). With double knockdown of *TOMM40* and either *APOE* or *LDLR* in HepG2 cells, there was a significant reduction in Nile red fluorescence vs. *TOMM40* KD alone (**Fig 7E**), suggesting that the accumulation of LDs with *TOMM40* KD is in part due to lipoprotein uptake via upregulation of the APOE/LDLR pathway. Similar to the findings in HepG2 cells, Oil Red O (ORO) staining of livers from both male and female mice following *in vivo Tomm40* KD demonstrated a greater number of LDs vs. the scrambled shRNA controls (**Fig 7H-J, S8**). Consistent with these findings, significant hepatic steatosis in both sexes was confirmed by hematoxylin-eosin staining of liver sections (**Fig 7S-T**), as well as increased liver-to-bodyweight ratio (**Fig 7U**), and elevated plasma AST (**Fig 7V**), though plasma ALT was increased only in males (**Fig 7W**).

Although *Tomm40* KD in both sexes induced hepatic steatosis, the intracellular mechanisms were found to be different. Imaging the 3D morphology of LDs at MERCs by focused ion beam scanning electron microscopy (FIB-EM) (**Fig 7L**) in conjunction with TEM analysis revealed not only an increase in average LD surface area per cell (**Fig 7K**), but also increased LD-mitochondria contact sites (**Fig 7M-N**) and reduced LD-ER contact sites in the livers of male (**Fig 7O-P**), though not in female (**Fig S9), ***Tomm40* KD mice. The evidence for increased LD formation from mitochondria rather than the ER in males was supported by reduced expression of *Bscl2*, the gene encoding seipin, which is known to play a key role in LD formation from the ER at MERCs[140] (**Fig 7Q**). Moreover, in isolated hepatic mitochondria-associated membranes (MAMs) containing MERCs, we consistently observed reduced BSCL2 protein expression in males (**Fig 7R**). Having confirmed the reduction in *BSCL2* gene and protein expression (MAMs fraction) in *TOMM40* KD HepG2 cells (**Fig 7F,G**), we showed this effect to be LXR-independent by treatment with GSK2033 (**Fig S11**). In female mice livers, *Tomm40* KD did not affect BSCL2 protein expression in MAM fractions (**Fig S10**), which may explain the lack of disruption of LD-ER contact sites. No changes in cytosolic BSCL2 protein levels were found in either sex (**Fig S10**). Despite sex-differences, these results suggest that decreased BSCL2-mediated LD formation from the ER with *TOMM40* KD to play a potential auxiliary role, specifically in males, in the uptake of triglyceride-rich lipoproteins via LDLR.

3.4 Discussion & Conclusion

TOMM40 is a subunit of the TOM complex that has a key role in mediating uptake of mitochondria-targeted proteins, maintaining mitochondrial membrane potential, and reducing the mitochondrial stress response[21,22]. We show here, by KD of *TOMM40* in hepatocytes and *in vivo* in mice, that TOMM40 also has multiple effects that impact hepatic lipid and plasma lipoprotein metabolism. A primary mechanism for these effects is increased activation of LXRs as well as greater *LXRB* gene expression with *TOMM40* KD that resulted in increased transcription of multiple genes affecting cholesterol and lipoprotein metabolism. Notably, we found that LXR-mediated upregulation of both *APOE* and *LDLR* with *TOMM40* KD led to increased hepatocellular uptake of LDL as well as VLDL particles. We further demonstrated by concurrent KD of *MFN2* that disruption of MERCs was a major mediator of this LXRB-specific process, in conjunction with increased ROS and generation of oxysterols, in particular ROS-derived 7-ketocholesterol, a known ligand of LXR[141,142]. Interestingly however, *TOMM40* KD but not *MFN2* KD increased levels of oxysterols that are produced by enzymatic rather than oxidative reactions, suggesting that effects other than MERC disruption and mitochondrial dysfunction may also contribute to LXR activation by *TOMM40* KD. Other than 7-ketocholesterol, the increase in *CYP3A4* expression, the rate limiting step for 4β-OHC, in both *MFN2* KD and *TOMM40* KD HepG2 cells, could be explained by activation of pregnane X receptor (PXR), another nuclear receptor and transcriptional regulator of CYP3A4, that may be due to MERC-induced cellular stress response[143,144]. Furthermore, increased *CYP3A4* expression and thus 4β-OHC have been shown to regulate lipogenic genes, including *SREBP1c,* and liver triglyceride levels via LXR activation[145]. However, future experimentation is required to confirm the role of 4β-OHC in mediating effects of *TOMM40* KD.

Notably, despite demonstrating that *TOMM40* KD increased cellular uptake of LDL via upregulation of LDLR and APOE, intracellular cholesterol levels were reduced, a finding confirmed in male mouse livers *in vivo*. This was shown to be primarily due to increased expression of *ABCA1*, a LXR transcriptional target[146], in that KD of *ABCA1* abrogated this effect of *TOMM40* KD. Reduction in cellular cholesterol ester content could also have been impacted by the observed reduced expression of *ACAT1*, the enzyme responsible for the esterification of free cholesterol[147] that is enriched at MERCs[148].

It has been reported that LXR, specifically LXRA, can directly regulate *LDLR* gene expression in hepatoblastoma cells[149]. We have further shown that LXR can induce increased expression of *SREBF1c*[150], and our finding that KD of this gene abrogated the increase in *LDLR* expression with *TOMM40* KD points to its upregulation by LXR in mediating the *LDLR* response, likely by binding to the *LDLR* promoter region as shown from our luciferase experiment and previously in HepG2 cells[151,152]. While SREBF2 is the major transcription factor regulating increased expression of LDLR in response to reduced cellular unesterified cholesterol content[153], our finding that expression of *HMGCR*, a canonical SREBF2 target[154], is not affected by *TOMM40* KD suggests that SREBF2 activity does not play a significant role in *TOMM40* KD-induced LDLR upregulation.

Among the genes upregulated by *TOMM40* KD in HepG2 cells were *CYP7A1* and *CYP27A1*, which mediate the rate-limiting steps in the synthesis of the bile acids cholic acid (CA) and chenodeoxycholic acid (CDCA), respectively[155,156]. Consistent with the *CYP7A1* effect, we found that both intracellular levels and secretion of CA were increased by *TOMM40* KD, representing another route for disposing of cellular cholesterol. While *Tomm40* KD male mice showed increased plasma CA levels, no clear differences were detected in females. These results can be explained by previously identified sex-linked differences in not only hepatic bile acid production and secretion[157], but also composition, storage, and release of bile acids from the gallbladder[158] and bile acid metabolism in the gut microbiota[159], all known to contribute to plasma CA levels independent of CYP7A1 activity. Furthermore, it has been reported that women have lower circulating bile acid concentrations than men, which may protect from development of hepatocellular carcinoma[160]. In contrast, despite the increased expression of *CYP27A1*, independent of LXR activity (**Fig S12**), cellular CDCA content was reduced. Synthesis of the CDCA precursor 27-OHC occurs in mitochondria[161,162], separate from LXR regulation, and the interaction of TOMM40 with STAR at MERCs has been shown to promote transport of cholesterol into mitochondria[117,163]. We observed that *STAR* expression is reduced by *TOMM40* KD, and suggest that this, together with MERC disruption as shown by *MFN2* KD, leads to a decrease of mitochondrial cholesterol that is available for 27-OHC and CDCA synthesis.

In contrast to the reduction of cholesterol in HepG2 cells by *TOMM40* KD, we observed a significant increase in cellular content of triglycerides. This is likely attributable to stimulation of uptake of triglyceride-rich VLDL, which as for LDL, was shown to be mediated by upregulation of *LDLR* in conjunction with increased expression of *APOE*. While *TOMM40* KD also increased expression of genes encoding other APOE-binding proteins - *LRP* and *SDC1*[164] - KD of these genes had no effect on VLDL uptake. Moreover, there was no phenotypic effect of hepatic *TOMM40* KD on expression of genes regulating VLDL secretion or triglyceride synthesis. The increase in cellular triglyceride was manifest by greater number and size of LDs, and the dependence of their formation on *LDLR*-mediated triglyceride uptake was confirmed by demonstrating reduced lipid staining with KD of either *LDLR* or *APOE*. It has previously been shown in astrocytes that APOE can also act as a LD surface protein regulating LD size and triglyceride saturation, independent of an effect at the ER lumen[165].

Consistent with the cellular findings, *in vivo* KD of *Tomm40* resulted in increased hepatic triglyceride and reduced cholesterol content, and increased size and number of hepatic LDs. Consequently, *Tomm40* KD mice developed hepatic steatosis based on histological (H&E and ORO) assessments and quantification of plasma AST and ALT levels. Apart from LD accumulation in hepatocytes, the remodeling of LD contact sites and dynamics in response to metabolic changes in the liver is another defining characteristic of hepatic steatosis and MASLD[166]. In this regard, we have shown that *TOMM40* KD reduced LD-ER contact sites in HepG2 cells via a reduction in BSCL2 (seipin) expression in MAMs containing MERCs. Loss of BSCL2 at LD-ER interfaces has been shown to result in abnormal LDs including supersized variants, consistent with our findings[167,168]. By TEM we have shown that in conjunction with reduction of LD-ER contact sites there was an increase in LD-associated mitochondria with *TOMM40* KD, an effect that may lead to increased trafficking of triglyceride-derived fatty acids via LDs into the mitochondria[169] as well as the upregulation of fatty acid oxidation that has been associated with MASLD[170].

While the effects of *TOMM40 KD* on LD-ER and LD-mitochondria contact sites and BSCL2 (seipin) expression in HepG2 cells were replicated in liver tissue from male mice following in vivo *Tomm40* KD, these effects were not observed in females. Thus, mechanisms other than suppression of the seipin pathway are responsible for promoting LD accumulation and hepatic steatosis with *Tomm40* KD in females, and it is possible that these mechanisms are also operative in males. For example, mediators of LD formation located outside of MERCs, including FITM2, regulate the budding of LDs from ER into the cytosol[171], and coalescence of LDs is promoted by the CIDE family of proteins (aka FSP27)[172,173]. Additionally, it is notable that sex hormones including estrogen, have been reported to transcriptionally regulate genes involved in mitochondrial dynamics and mitophagy, including *MFN2* expression, which may further explain the differential effects of *Tomm40* KD on MERCs and mito-LD contact sites between male and female mouse livers[174,175].

In addition to promoting hepatic steatosis, *in vivo* KD of *Tomm40* in mice resulted in significant reductions in plasma lipid and lipoprotein levels that were greater in males. This may reflect sex differences in lipoprotein production and/or clearance[176] that resulted in higher baseline plasma lipid levels in the males[177], as well as differing age-related effects[178,179] and the use of a western diet, since, for example, female C57BL/6J mice are resistant to high fat diet-induced obesity[180].

While a strength of this study is the identification of significant effects of hepatic *TOMM40/Tomm40* KD on lipid and lipoprotein metabolism in both a human liver cell and an *in vivo* mouse model, further study will be required to replicate the findings in other hepatic cell lines and mouse strains, and to test the *in vivo* effects in conjunction with other dietary interventions, especially in light of the sex difference in lipid metabolism noted above and the report that high-fat diets promote formation of LD contact sites with mitochondria and ER[169]. Finally, kinetic studies of the effects *Tomm40* KD on lipoprotein production and clearance are needed to determine the basis for the reductions in their plasma levels and the differing effects in male and female mice. In this regard, it remains possible that extrahepatic *Tomm40* KD with our AAV8-shRNA, as we have observed in skeletal muscle[181], could have contributed to these plasma lipid changes.

Our findings suggest that identification of agents which increase hepatic TOMM40 expression, and in doing so, maintain mitochondrial function and MERCs, could provide new therapeutic opportunities for MASLD, as well as other conditions such as Alzheimer's disease in which mitochondrial pathology plays a role. Finally, our discovery that *TOMM40* KD increases expression of the adjacent *APOE* gene suggests a novel connection between mitochondrial function and lipid metabolism.

3.5 Methods

3.5.1 Mice studies

6-week old C57BL/6J male and female mice (*n=6* per group) were purchased from Jackson Laboratory (Bar Harbor, ME) and placed on a western diet (0.15% cholesterol, 21% fat, D12079Bi, Research Diets). At 8 weeks of age, mice were intraperitoneal (IP) injected with either $4\text{x}10^{11}$ GC AAV8-Tomm40 shRNA or AAV8-CMV-null as a control (VectorBuilder). Weekly bodyweight and food intake measurements were recorded. At 14-weeks old, unfasted mice were terminated and liver tissues were collected, snap frozen in liquid nitrogen, and immediately transferred to -80°C freezer. For electron microscopy, tissues were immediately fixed in 2% glutaraldehyde + 2% paraformaldehyde solution after termination. Blood was collected by cardiac puncture and plasma separated via centrifugation at 850 x g for 15 min at 4°C. All experiments were done blinded and randomized. Animal research was approved by the University of California, San Francisco, Laboratory Animal Resource Center.

3.5.2 Primary mouse hepatocytes

Hepatocytes were isolated from wild-type, 8-12 week-old C5BL/6J male mice (Jackson Laboratory) by the UCSF Liver Center according to the protocol established by Desai et al.[186] Hepatocytes were cultured in DMEM with 5% fetal calf serum (Hyclone), L-glutamine, penicillin-streptomycin antibiotic, insulin-transferrin-selenium, and HEPES (Gibco). *Tomm40* and non-targeting control (NTC) siRNAs were transfected into the primary hepatocytes using TransIT-TKO® transfection reagent (Mirus Bio) according to the manufacturer's protocol for 48 hr after hepatocyte plating at 37°C and 5% CO_2.

3.5.3 HepG2 cell culture

HepG2 human hepatoma cells were grown in EMEM (Eagle's Minimum Essential Medium; ATCC) supplemented with 10% fetal bovine serum (FBS; Thermo Fisher Scientific) or 10% lipoprotein-deficient serum (LPDS; Thermo Fisher Scientific), and 1% penicillin-streptomycin (Gibco) at 37°C and 5% CO_2. Cells were passaged every 7 days. Cells were routinely tested for mycoplasma using MycoAlert™ PLUS mycoplasma detection kit (Lonza) and only mycoplasma negative cells were used.

Knock-down (KD) of *TOMM40, MFN2, LXRA, LXRB, APOE, LDLR, DGAT1, DGAT2, LRP1, SDC1, ABCA1*, and *SREBF1*, was achieved by addition of their respective siRNAs (10 µM) using Lipofectamine RNAiMAX transfection reagent (Life Technologies) and Opti-MEM I (Gibco) according to the manufacturer's instructions for 48 hrs.

Human pCMV- expressing- TOMM40 (NM_001128916.2), STAR (NM_000349.3), and empty vector (EV; ORF_stuffer) plasmids stored in bacterial glycerol stocks were purchased from VectorBuilder Inc. Expression plasmids were cultured on Luria-Bertani

(LB) Agar plates containing ampicillin at 37°C. Single colonies were selected and grown separately in LB broth at 37°C with continuous shaking (225 rpm) overnight. DNA plasmids were extracted by ZymoPURE II Plasmid Midiprep Kit (Zymogen) according to the manufacturer's protocol. Cells were transiently transfected with purified plasmids using Lipofectamine 3000 transfection reagent (Thermo Fisher Scientific).

3.5.4 Mitochondrial respiration measurements

HepG2 cells were seeded at 2,000 per well in 96-well plates with XF assay medium (Agilent) supplemented with 2 mM sodium pyruvate (Gibco), 2 mM GlutaMAX™ (Gibco), and 10 mM glucose (Sigma), at pH 7.4. During experimentation, 1.5 μM oligomycin, 2 μM FCCP, and 2 μM Antimycin A + Rotenone (Seahorse XF Cell Mito Stress Test Kit, Agilent) were added sequentially to the Agilent Seahorse XFe96 Extracellular Flux Analyzer via injection ports to determine basal and maximum respiration, ATP production, and proton leak. Oxygen consumption rate (OCR) values were presented with non-mitochondrial oxygen consumption deducted and normalized to total protein concentration per well using BCA assay (Genesee Scientific).

3.5.5 Mitochondrial assays

Cellular reactive oxygen species (ROS) were quantified by the DFCDA/H2DCFDA – Cellular ROS Assay Kit (Abcam) according to the manufacturer's instructions. Cells were stained with DFCDA for 45 min and washed in 1X DPBS. Fluorescence intensity was measured by a fluorescence spectrophotometer with excitation/emission at 485 nm/535 nm.

3.5.6 Calcium imaging

Mag-Fluo-4AM was used to quantify free Ca2+ within the ER lumen[187]. HepG2 cells were seeded in a black clear-bottom 96-well plate and transfected with siRNAs for 48 hrs. Cells were then washed with Hank's Buffered Saline Solution (HBSS) containing 20 mM Hepes, and then incubated with 10 μM Mag-Fluo-4 AM (Thermo Fisher Scientific) for 1 hr at 37°C in HEPES-buffered saline (135 mM NaCl, 5.9 mM KCl, 11.6 mM HEPES, 1.5 mM CaCl2, 11.5 mM glucose, 1.2 mM MgCl2, pH 7.3), supplemented with BSA (1 mg/mL) and pluronic acid (2%, v/v). Excess dye was then washed off using HBSS and measured on a fluorescent spectrophotometer at a wavelength of 495/515 (Ex/Em).

3.5.7 TEM sample preparation

HepG2 cells were grown on MatTek glass bottom dishes (P35G-1.5-14-C, MatTek) and fixed in 2% glutaraldehyde + 2% paraformaldehyde solution (prepared by Electron Microscopy Lab, UC Berkeley) for 24 hrs. Cells and tissues were post-fixed in 1% osmium tetroxide in 0.1 M sodium cacodylate buffer, pH 7.2, for 1-2 hrs. Cells were dehydrated in a serial diluted ethanol solution from 30 to 100%. Liver tissues were embedded in increasing concentrations of Durcupan resin. HepG2 cells for TEM imaging were infiltrated with 50% Epon-Araldite resin (containing benzyldimethylamine (BDMA) accelerator), followed by 100% resin for 1 hr each. Cells and tissues were polymerized at 60C for 24hrs.

3.5.8 Transmission electron microscopy

The resin embedded sample blocks were trimmed, and 90 nm ultrathin sections were cut using a Leica UC6 ultramicrotome (Leica Microsystems, Vienna, Austria) and collected onto formvar-coated slot grids. Sections were imaged to find target regions using a Tecnai 12 120kV TEM (FEI, Hillsboro, OR, USA) and data recorded using an Gatan Rio16 CMOS camera and GMS3 software (Gatan Inc., Pleasanton, CA, USA).

3.5.9 Volume imaging processing for liver tissue

200 µm thick slices from previously fixed material were stained using an osmium-thiocarbohydrazide-osmium (OTO) method[188,189] in combination with microwave-assisted processing, followed by high pressure freezing and freeze substitution (HPF-FS), as previous described by Ewald et al.[190] Briefly, samples were OTO stained, incubated with 2% aqueous uranyl acetate overnight, subjected to HPF followed by super quick FS[85] with 4% osmium tetroxide, 0.1% uranyl acetate and 5% ddH2O in acetone, and embedded and polymerized in hard epon resin.

3.5.10 Focused ion beam scanning electron microscopy (FIB-SEM) imaging

The trimmed sample blocks were glued with silver paint (Ted Pella Inc.) onto Al stubs, and sputter coated (Pd/Au) with a Tousimis sputter coater on top of a Bio-Rad E5400 controller. Focused Ion Beam Scanning Electron Microscopy (FIB-SEM) imaging was performed using a Zeiss Crossbeam 550 (Carl Zeiss Microsystems GmbH, Oberkochen, Germany). The sample was tilted at 54˚ in order to be perpendicular to the ion beam. FIB milling and SEM imaging of the target area were set up using Atlas 5 3D tomography (Carl Zeiss Microsystems GmbH, Oberkochen, Germany). Slices with a thickness of 10 nm were milled from the target area using a 30 kV 300 pA ion beam. Energy-selective Backscattered (ESB) images were collected at 1.5 kV 1nA with a dwell time of 18 ns, image pixel size of 10 nm, and tilt correction angle of 36°.

3.5.11 Image processing

TEM and FIB-SEM images were analyzed using ImageJ software according to the method of Lam et al. Contact sites between organelles were identified manually from high-resolution, high-magnification TEM images, and outlined using an optical pen in ImageJ to calculate structural parameters. MERCs (and other contact sites) were identified by having a gap of 10-30 nm between the outer mitochondrial membrane, the ER, or the lipid droplet membrane, as well as having the ER be ribosome-free[191]. The collected FIB-SEM images were aligned with the Slice Registration in Dragonfly 2022.2 (Comet Technologies Canada Inc., Canada). The Dragonfly Segmentation Wizard and Deep Learning Tool were used to segment organelles (lipid droplets, mitochondria, endoplasmic reticulum (ER)).

3.5.12 Enzyme-linked immunosorbent assay (ELISA)

Cells, supernatant, and liver tissues were lysed in M Cellytic Lysis Buffer containing 1% protease inhibitor (Halt™ Protease Inhibitor Cocktail; ThermoFisher Scientific) for 15 min using a cell disruptor or homogenizer. The lysate was centrifuged at 14,000 x g for 15 min and supernatant was collected. Oxysterols, 25-, 24(S)-, and 27- OHC, were quantified by ELISA kits purchased from MyBioSource according to the manufacturer's protocol. Total bile acid, cholic acid, and chenodeoxycholic acid levels were measured in cells and cell media (supernatant), by ELISAs purchased from Cell Biolabs Inc, according to the manufacturer's protocol. In addition, cholic acid was quantified in mouse plasma samples using the same kit from Cell Biolabs Inc. Samples from each experiment were normalized to protein levels quantified by BSA assay (Genesee Scientific).

3.5.13 Fluorescence imaging

To quantify LDL and VLDL uptake, HepG2 cells were loaded with 10 μM fluorescently labelled BODIPY™ FL LDL (Thermo Fisher Scientific) or DiI-labelled VLDL (Kalen Biomedical LLC) isolated from human plasma, for 4 hrs at 37°C. Cells were washed and reconstituted in 1X PBS buffer and read on a fluorescence spectrophotometer. Fluorescence readings were normalized to total protein concentration per well by BCA assay (Genesee Scientific).

LDLR cell surface protein was quantified by fixing cells in 4% paraformaldehyde and incubated with anti-LDLR at 1:100 (Santa Cruz Biotechnology, sc18823) for 45 min, followed by goat anti-mouse IgG-FITC at 1:400 (Santa Cruz Biotechnology, sc-2010) for 30 min. Intracellular 7-ketocholesterol was measured by fixing cells in 4% paraformaldehyde and staining with 7-ketocholesterol monoclonal antibody at 1:50 (3F7, Invitrogen, MA5-27561) diluted in 1X permeabilization buffer (Invitrogen) for 1 hr, followed by goat anti-mouse IgG-FITC at 1:400 (Santa Cruz Biotechnology, sc-2010) for 30 min.

To quantify lipid droplets, cells were stained with 100 μM Nile Red (Sigma) for 30 min. Fluorescence for all experiments described in this section was quantified on a BD LSRFortessa™ Cell Analyzer flow cytometer with a median fluorescence value of 10,000 gated events. Data was analyzed using FlowJo v10.7.1.

3.5.14 Lipid extraction and quantification

Mouse liver samples were homogenized by GentleMACS™ dissociator (Miltenyi Biotec) and cells were dissociated using a cell disruptor (Bio-Rad) in a mixture of chloroform, methanol, and water (8:4:3, v/v/v) (ref) or hexane-isopropanol (3:2, v/v) for lipid and cholesterol extraction, respectively. Hepatic and intracellular triglyceride (TAG) and glycerol were quantified with EnzyChrom™ Triglyceride or Glycerol Assay Kit (BioAssay Systems) according to the manufacturer's protocol. Lipid concentrations were measured at an absorbance of 570 nm. Cholesterol samples were dried under nitrogen gas and reconstituted with buffer (0.5 M potassium phosphate, pH 7.4, 0.25 M NaCl, 25 mM cholic acid, 0.5% Triton X-100). Intracellular cholesterol levels were then quantified with the Amplex Red Cholesterol Assay Kit (Life Technologies) according to the manufacturer's protocol.

3.5.15 Isolation of mitochondria and mitochondria-associated membranes

Mitochondria-associated membranes (MAMs) were isolated from HepG2 cells and liver according to the method of Wieckowski et al.[193] Cells were rinsed in 1X PBS twice, dislodged with 0.25% Trypsin-EDTA (Gibco), washed again in 1X PBS and centrifuged at 600 x g for 5 min at 4°C. Pelleted cells and liver tissue were resuspended in MSHE + BSA buffer (210 mM mannitol, 70 mM sucrose, 5 mM HEPES, 1 mM EGTA, and 0.5% BSA, at 7.2 pH). Samples were transferred to a small glass dounce and homogenized. The homogenate was centrifuged at 600 x g for 10 min at 4°C, and the supernatant was extracted and centrifuged at 8,000 x g for 10 min at 4°C. The pellet containing the isolated crude mitochondria was used to quantify mitochondrial cholesterol content. Furthermore, the isolated crude mitochondria were resuspended in MSHE + BSA buffer and percoll medium (Gibco) and centrifuged in a Beckman Coulter Optima L-100 XP Ultracentrifuge (SW40 rotor, Beckman) for 95,000 x g for 30 min at 4°C. The white band located above the mitochondria pellet was identified as the MAM fraction and collected and diluted ten times with MSHE + BSA buffer. The fraction was centrifuged at 100,000 x g for 1 hr (70-Ti rotor, Beckman) at 4°C to isolate the MAMs for immunoblotting.

3.5.16 Immunoblotting

Cells and liver tissues were lysed in M Cellytic Lysis Buffer containing 1% protease inhibitor (Halt™ Protease Inhibitor Cocktail; ThermoFisher Scientific) for 15 min using a cell disruptor or homogenizer, respectively. The lysate was centrifuged at 14,000 x g for 15 min, supernatant was collected, and protein concentration was measured by BCA assay (Genessee Scientific). Proteins were separated on a 4-20% Tris-polyacrylamide gradient gel (Bio-Rad) and transferred onto a nitrocellulose membrane using the iBlot™ 2 Gel Transfer Device (ThermoFisher Scientific). Membranes were blocked in Tris-buffered saline with 0.1% tween (TBST) + 5% milk for 2 hrs to minimize non-specific antibody binding. Membranes were then incubated with primary antibodies diluted 1:1000 (v/v) in TBST overnight on a rotating platform at 4°C. After washing in TBST, membranes were incubated with secondary antibodies, anti-rabbit IgG (7074) and anti-mouse IgG (7076), HRP-linked antibodies (Cell Signal) at 1:2500 (v/v) dilution, for 30 min before a last series of washes. SuperSignal™ West Pico PLUS Chemiluminescent Substrate (ThermoFisher Scientific) was added to the membrane to visualize proteins. All antibodies used are listed in the key resources table.

3.5.17 RT-qPCR

RNA was extracted from liver tissue and cell samples using RNeasy Mini Qiacube Kit (Qiagen) with the Qiacube Connect (Qiagen) according to the manufacturer's protocol. cDNA synthesis from total RNA was performed using the High Capacity cDNA Reverse Transcription Kit (Applied Biosystems). Primers were designed and obtained from Elim Biopharmaceuticals and run with SYBR™ Green qPCR Master Mix (Thermo Fisher Scientific) on an ABI PRISM 7900 Sequence Detection System to quantify mRNA transcript levels. RT-qPCR primers used in this study are listed in the key resources table. The mean value of triplicates for each sample was normalized to GAPDH (human) or 18s (mouse) as the housekeeping genes.

To quantify mRNA stability, Actinomycin D (Life Technologies) at a final concentration of 1 µg/mL was added to HepG2 cells treated with siRNAs at varying time intervals between 0-240 mins. At each time point, qPCR was conducted to quantify *LDLR* mRNA transcript levels. The half-life of the *LDLR* mRNA transcript in HepG2 cells with *TOMM40* KD was compared to the NTC group.

3.5.18 Dual luciferase reporter assay

The dual luciferase assays were performed as previously described in Smith et al.[194] HepG2 cells were seeded on 96-well plates with 100 µL of low glucose EMEM + 10% FBS or 10% LPDS (lipoprotein-deficient serum). On day of seeding, cells were transfected with indicated siRNAs. After 48 hrs, cells were transfected with indicated 100 ng LDLR luciferase construct + 1 ng secreted nanoluciferase construct in a total of 10 µL OptiMEM using Lipofectamine 3000 transfection reagent (Life Technologies) according to the manufacturer's instructions. 48 hours post LDLR-luciferase transfection and treatment, 10 µL of media from each well was added to 10 µL of non-lytic 2x coelenterazine reagent (300 mM sodium ascorbate, 5 mM NaCl, 0.1% BSA, 40 µM coelenterazine (Goldbio CZ25)) in separate wells of a 384-well plate. Nanoluciferase plate was shielded from light incubated on a shaker at room temperature for 10 mins. Firefly luciferase activity was immediately evaluated in the plates containing the cells by adding 100 µL of 2x firefly lytic assay buffer (100 mM Tris-HCl pH 7.7, 50 mM NaCl, 2 mM MgCl2, 0.17% Triton X-100, 10 mM DTT, 0.4 mM coenzyme A, 0.3 mM ATP, and 0.28 mg/ml luciferin (Goldbio LUCK-1G)). Raw luminescence for all plates was measured on a plate reader with 1 second integration time. Readout of firefly luciferase in each well was normalized to the corresponding secreted nanoluciferase control.

3.5.19 Plasma lipid and lipoprotein analyses

Total cholesterol (TC), HDL-C, triglyceride, AST (aspartate aminotransferase) and ALT (alanine transaminase) levels were measure by enzymatic end-point measurements using enzyme reagent kits (Kamiya Biomedical) in an AMS Liasys 330 Clinical Chemistry Analyzer[195]. Non-HDL-C was calculated by subtracting HDL-C from TC. Lipoprotein particle concentrations were measured by gas-phase electrophoresis (ion mobility)[196] according to the method of Caulfield et al.[197]

3.5.20 Histological analyses

Frozen liver samples were embedded in Tissue-Tek optimum cutting temperature (OCT) compound on frozen blocks and sectioned on a Cryostar NX60 Cryostat Instrument (Epredia). Slides were sectioned at 10 μm thickness, stained with Oil Red O (ORO) or H&E, and scanned using a Versa 200 Automated Slide Scanner (Leica) with a 20 x air objective lens. Images were analyzed by ImageJ.

3.5.21 Statistical analysis

All data are presented as the mean ± standard error of mean (SEM). *N*-values in the figures refer to biological replicates and at least 3 replicates were conducted per condition and experiment. *P*-values were calculated using Student's t-tests for two groups. To compare more than two groups, one-way analysis of variance (ANOVA) with Tukey's post hoc test were used. Analyses were performed using GraphPad Prism 9 software (GraphPad Software, Inc.) $P<0.05$ was considered statistically significant.

3.6 Figures

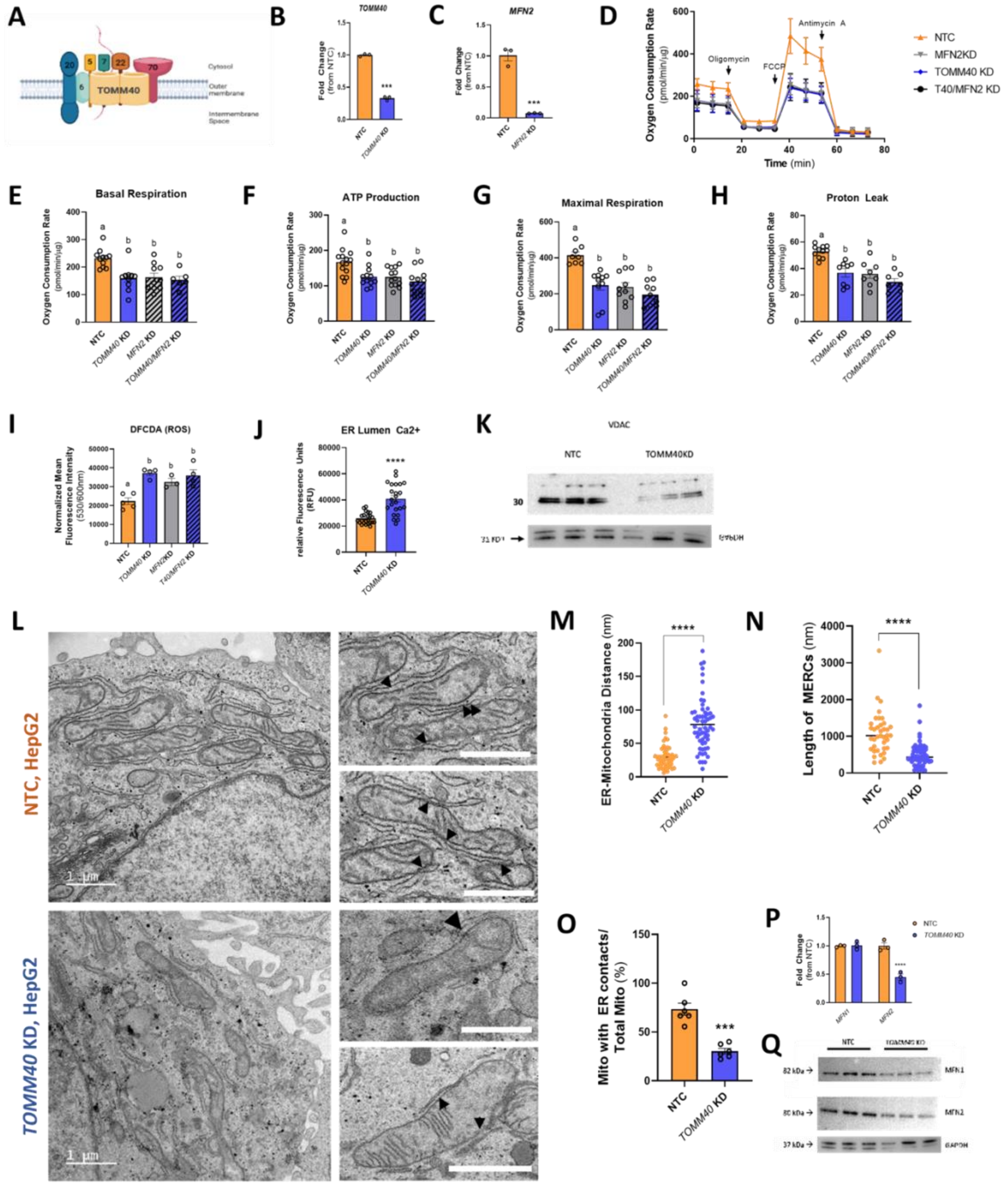

Figure 3-1. TOMM40 is essential for maintaining mitochondrial function and MERCs in hepatocytes.

(A)Schematic diagram of the mammalian TOM complex, consisting of 7 subunits, located in the outer mitochondrial membrane.

(B)Confirmation of *TOMM40* KD in HepG2 human hepatoma cells by ~75%, measured by qPCR. (*n=3* biological replicates)

(C) Confirmation of *MFN2* KD in HepG2 cells by ~90%, measured by qPCR. (*n=3*

biological replicates)
(D-H) (D) Oxygen consumption rates of HepG2 cells transfected with *TOMM40*, *MFN2*, and/or NTC siRNAs were quantified using the Seahorse 96e Extracellular Flux Analyzer. With the addition of oligomycin, FCCP, and Antimycin A + Rotenone, basal respiration (E), ATP production (F), maximal respiration (G), and proton leak (H) were quantified. (*n=10-12* biological replicates)
(I) Cellular ROS in *TOMM40* and *MFN2* KD vs. NTC HepG2 cells was quantified by DFCDA fluorescence probe. (*n=4-6* biological replicates)
(J) ER Lumen Ca2+ levels were measured by Mag-Fluo-4 AM fluorescence probe. (*n=12* biological replicates)
(K) Representative western blot of VDAC protein expression in HepG2 cells compared to GAPDH control.
(L) TEM micrographs of NTC and TOMM40 KD in HepG2 cells. Arrowheads indicate MERCs; scale bars, 1μm.
(M-O) Analysis of MERCs using ImageJ software: (M) ER-mitochondria distance (nm), (N) length of MERCs (nm), (O) percentage of mitochondria with ER contacts out of total mitochondria per cell. (*n= 12-24* cells/group)
(P) mRNA transcript levels of *MFN1* and *MFN2* in HepG2 cells quantified by qPCR. (*n=3* biological replicates)
(Q) Representative western blot of MFN1 and MFN2 protein expression in HepG2 cells compared to GAPDH control.
For all: *p<0.05, **p<0.01, ***p<0.005, ****p<0.001 vs. NTC by one-way ANOVA, with post-hoc Student's t-test to identify differences between groups. p<0.05 for *a* vs. *b* by two-way ANOVA, with Sidak's multiple comparisons test. Data are represented as mean ± SEM.

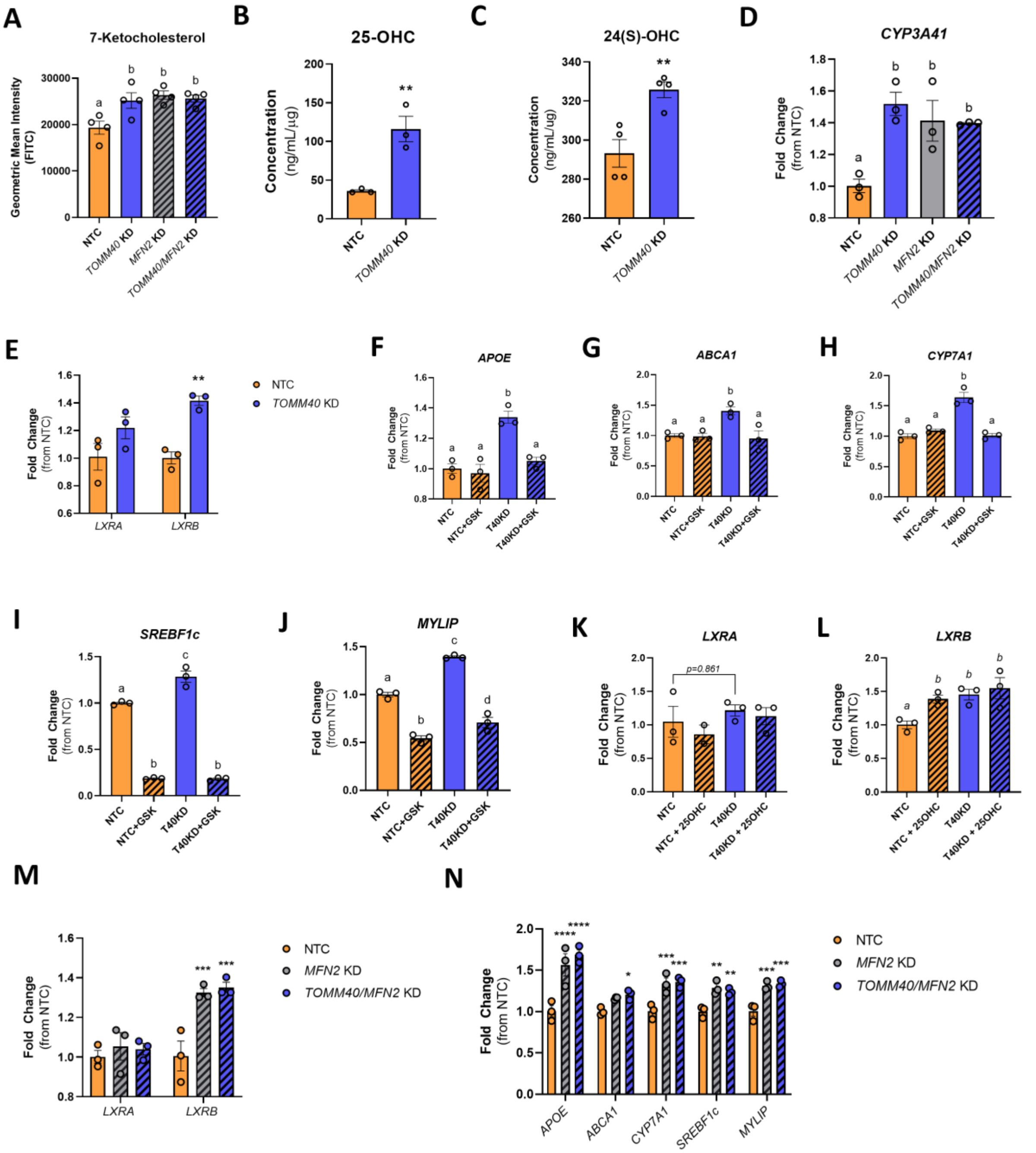

Figure 3-2. *TOMM40* KD upregulates LXRB and downstream gene targets by promoting oxysterol production.

(A) 7-ketocholesterol levels in HepG2 cells transfected with NTC vs. *TOMM40, MFN2, or TOMM40/MFN2* siRNAs by flow cytometry. (*n=4* biological replicates)

(B-C) Analysis of enzymatic-derived 25-OHC levels and 24(S)-OHC in *TOMM40* KD vs. NTC HepG2 cells by ELISAs. (*n=3* biological replicates)

(D) mRNA transcript levels of *CYP3A4*, responsible for the synthesis of 4β-OHC, in HepG2 cells, quantified by qPCR. (*n=3* biological replicates)

(E-J) (E) mRNA transcript levels of *LXRA* and *LXRB* and their downstream targets: *APOE* (F), *ABCA1* (G), *CYP7A1* (H*), SREBF1c* (I), and *MYLIP* (J), in HepG2 cells

quantified by qPCR.
(K-L) mRNA transcript levels of *LXRA* (K) and *LXRB* (L) in HepG2 cells transfected with NTC vs. TOMM40 siRNAs after the addition of 10 µM GSK2033 (LXR antagonist). (*n=3* biological replicates)
(M-N) (M) mRNA transcript levels of *LXRA* and *LXRB* and their downstream targets (N) in NTC, *TOMM40* KD, *MFN2* KD, and *TOMM40/MFN2* KD HepG2 cells, quantified by qPCR. (*n=3* biological replicates)
For all: *p<0.05, **p<0.01, ***p<0.005, ****p<0.001 vs. NTC by one-way ANOVA, with post-hoc Student's t-test to identify differences between groups. p<0.05 for *a* vs. *b* vs. *c* vs. *d* by two-way ANOVA, with Sidak's multiple comparisons test. Data are represented as mean ± SEM.

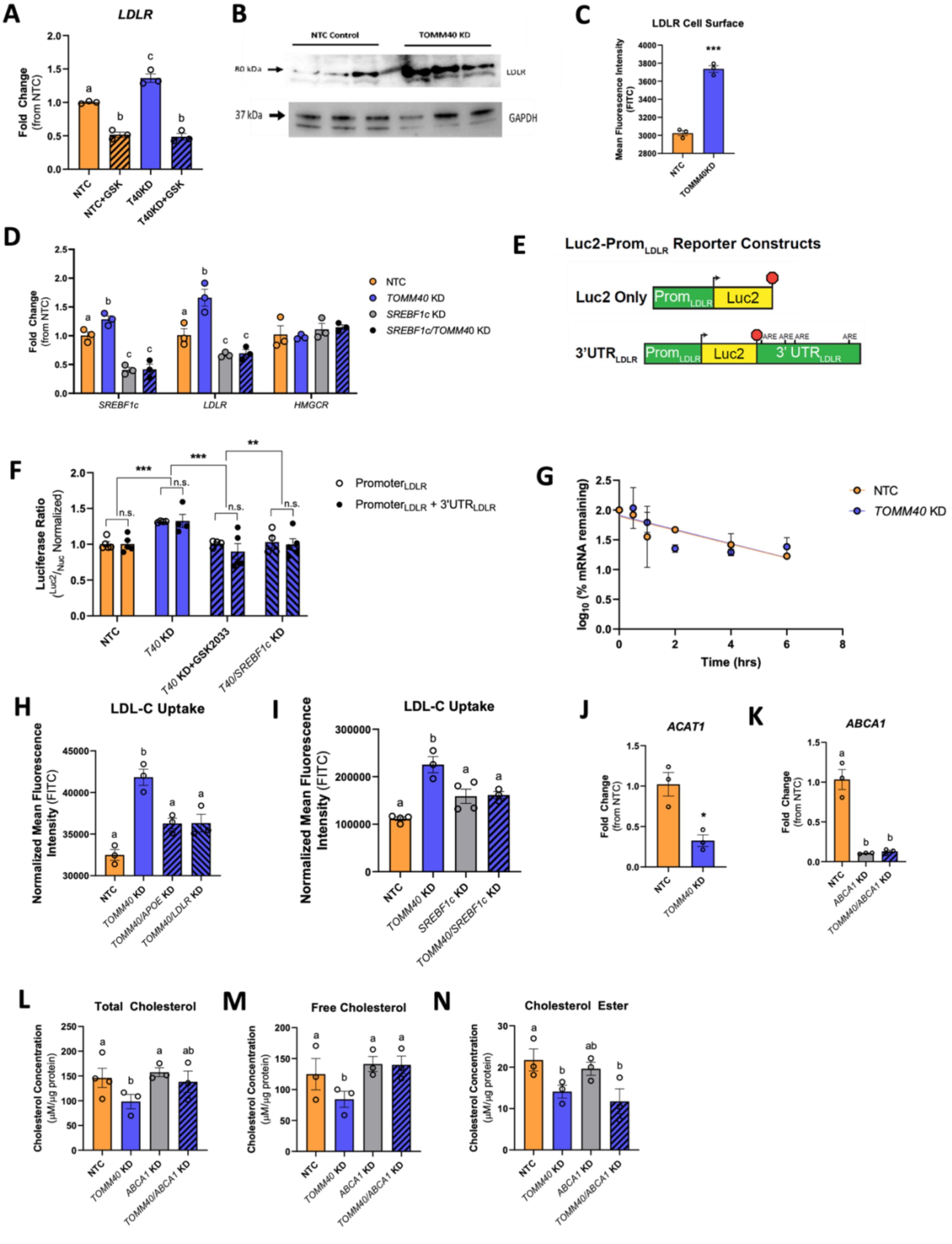

Figure 3-3. ***TOMM40*** **KD promotes LDL uptake via an LXR-mediated pathway.**
(A) *LDLR* mRNA transcripts were quantified by qPCR in HepG2 cells treated with NTC vs. *TOMM40* KD, with or without GSK2033. (*n=3* biological replicates)
(B) Representative western blot of LDLR protein expression in NTC vs. *TOMM40* KD

HepG2 cells.
(C) LDLR cell surface protein levels were stained with anti-LDLR antibody and analyzed by flow cytometry. (*n=3* biological replicates)
(D) mRNA transcripts confirming KD of *SREBF1c* and changes in expression of *LDLR* and *HMGCR* in *SREBF1*, *TOMM40*, and NTC siRNAs-treated HepG2 cells. (*n=3* biological replicates)
(E) Schematic diagram of Luc2-Prom$_{\mathrm{LDLR}}$ reporter constructs, illustrating *LDLR* promoter, start site (arrowhead), stop codon (red octagon), and 3'UTR region, containing adenylate-uridylate (AU)-rich elements (AREs) implicated in mRNA stability, of the *LDLR* gene.
(F) Ratiometric luciferase outputs of HepG2 cells transfected with indicated reporters. (*n=4-5* biological replicates) n.s. = non-significant. Two-way ANOVA, $^{**}p<0.01$, $^{***}p<0.005$ by Holm-Sidak test. Data are represented as mean ± SEM.
(G) Relative expression of *LDLR* mRNA in NTC vs. *TOMM40* KD HepG2 cells after arrest of transcription with actinomycin D. (*n=3* biological replicates)
(H-I) BODIPY-labelled LDL-C was taken up in HepG2 cells and fluorescence was quantified on a microplate fluorescence spectrophotometer. (*n=3* biological replicates)
(J-K) mRNA transcripts of *ACAT1* (J) and *ABCA1* (K) expression quantified by qPCR.
(L-N) Intracellular total cholesterol (L), free cholesterol (M), and cholesterol ester (N) levels quantified from HepG2 cells transfected with NTC, *TOMM40*, and *ABCA1* siRNAs, singly and in combination, using Amplex Red Cholesterol Assay. (*n=3-4* biological replicates)
For all (except F): $^{*}p<0.05$, $^{**}p<0.01$, $^{***}p<0.005$, $^{****}p<0.001$ vs. NTC by one-way ANOVA, with post-hoc Student's t-test to identify differences between groups. $p<0.05$ for *a* vs. *b* vs. *c* by two-way ANOVA, with Sidak's multiple comparisons test. Data are represented as mean ± SEM.

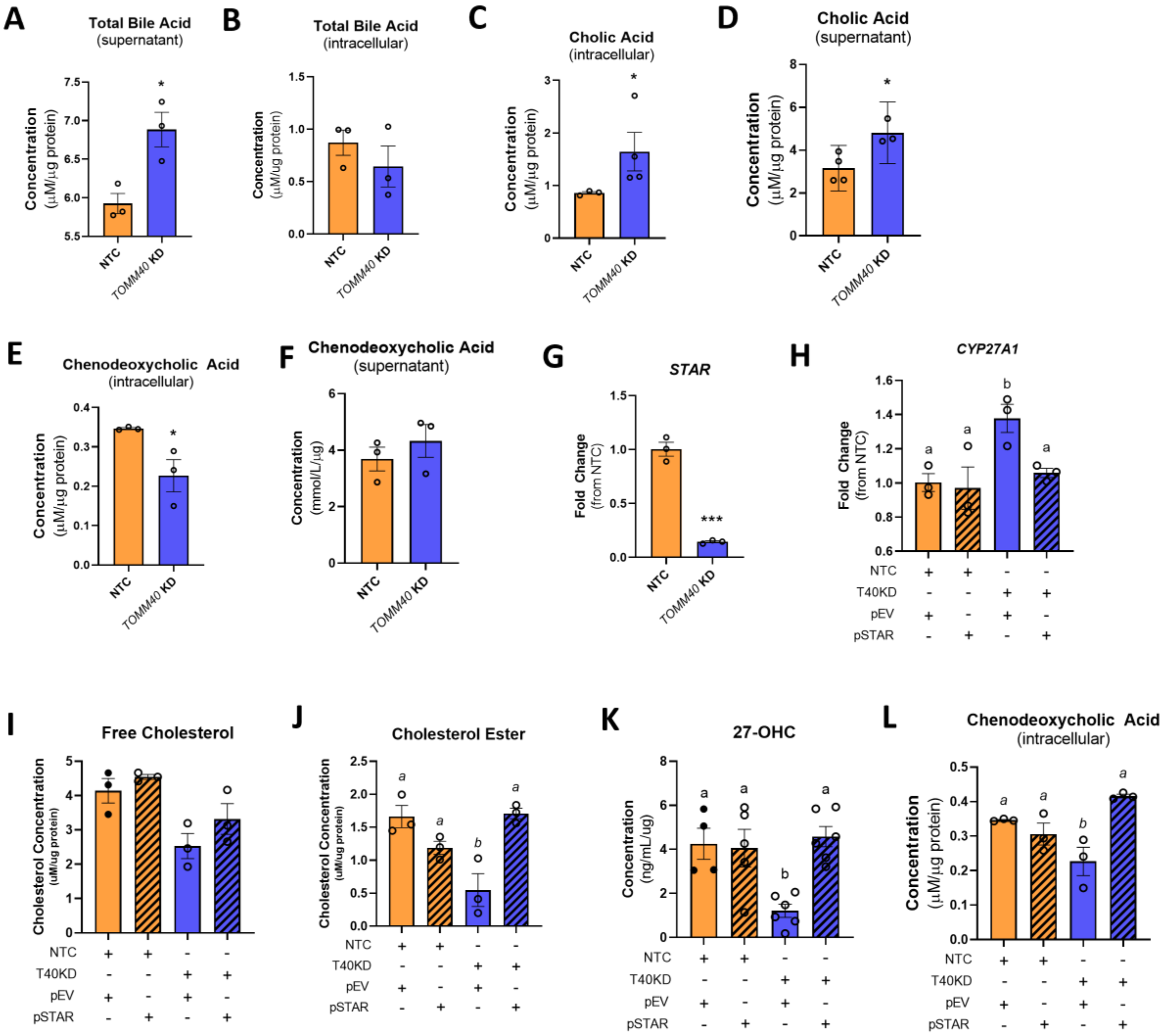

Figure 3-4. *TOMM40* KD in hepatocytes promotes classic bile acid synthesis pathway while inhibiting alternative pathway via interaction with STAR at MERCs

(A-B) Total bile acid levels in NTC vs. *TOMM40* KD HepG2 cells were measured in the supernatant (cell media; A) and intracellularly (B) by ELISA and normalized to protein concentration by BCA assay.

(C-D) Cholic acid levels were quantified intracellularly (C) and in the supernatant (D) of HepG2 cells.

(E-F) Chenodeoxycholic acid levels were measured intracellularly (E) and in the supernatant (F) in NTC vs. *TOMM40* KD HepG2 cells.

(G) mRNA transcripts of *STAR* were quantified in NTC vs. *TOMM40* KD HepG2 cells by qPCR.

(H) *CYP27A1* gene expression was measured in NTC vs. TOMM40 KD HepG2 cells with overexpression of an empty vector (pEV) or a *STAR*-expressing plasmid (pSTAR).

(I-J) Mitochondrial free cholesterol (I) and cholesterol ester (J) levels were measured

by Amplex Red Cholesterol Assay in HepG2 cells.
(K) Analysis of enzymatic-derived 27-OHC levels in *TOMM40* KD vs. NTC HepG2 cells overexpressed with pEV or pSTAR by ELISA.
(L) Analysis of intracellular chenodeoxycholic acid levels in NTC vs. *TOMM40* KD HepG2 cells overexpressing pEV or pSTAR.
For all: *p<0.05, **p<0.01, ***p<0.005, ****p<0.001 vs. NTC by one-way ANOVA, with post-hoc Student's t-test to identify differences between groups. p<0.05 for *a* vs. *b* by two-way ANOVA, with Sidak's multiple comparisons test. Data are represented as mean ± SEM. (*n=3* biological replicates)

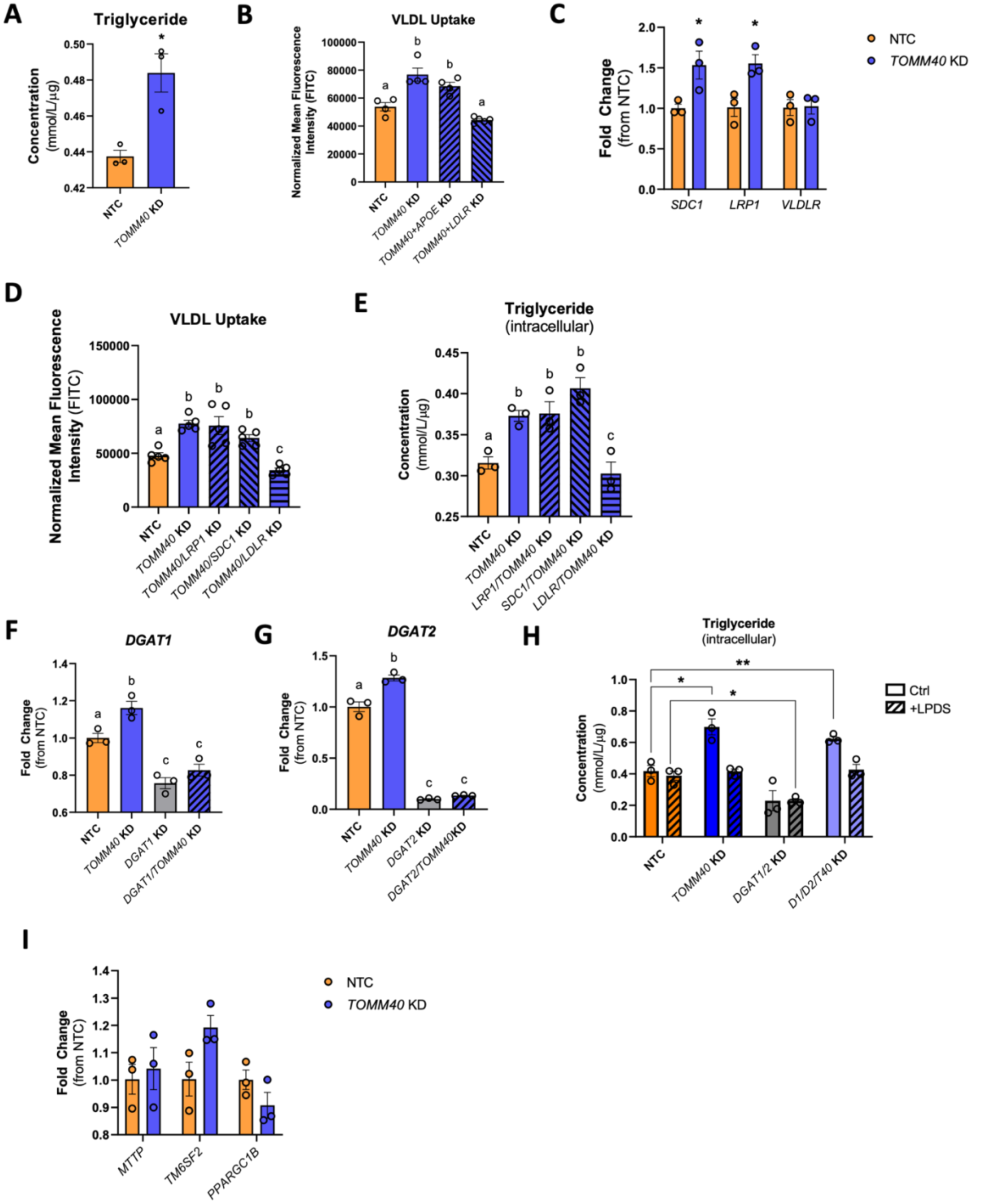

Figure 3-5. *TOMM40* KD promotes VLDL uptake and triglyceride accumulation via LDLR upregulation.

(A) Quantification of intracellular triglyceride in HepG2 cells transfected with NTC vs. *TOMM40* siRNAs.

(B) Quantification of DiI-labelled human VLDL uptake after 4 hr incubation by HepG2 cells transfected with siRNA for *TOMM40* singly and in combination with siRNAs for

APOE, and *LDLR* KD, vs. NTC, measured by fluorescence spectrophotometry.
(C) Relative *SDC1, LRP1*, and *VLDLR* mRNA levels in HepG2 cells transfected with NTC vs. *TOMM40* siRNAs, measured by qPCR.
(D) Quantification of DiI-labelled VLDL uptake after 4 hr incubation by HepG2 cells transfected with siRNA for *TOMM40* singly and in combination with siRNAs for *LRP1, SDC1*, and *LDLR*, vs. NTC, measured by fluorescence spectrophotometry
(E) Intracellular triglyceride levels quantified in HepG2 cells transfected with siRNA for *TOMM40* singly and in combination with siRNAs for *LRP1, SDC1*, and *LDLR,* vs. NTC.
(F-G) Relative mRNA transcript levels of *DGAT1* and *DGAT2* in HepG2 cells transfected with NTC vs. siRNAs for *TOMM40, DGAT1*, and *DGAT2*, singly and in combination, measured by qPCR.
(H) Quantification of intracellular triglyceride in *DGAT1/DGAT2* KD vs. *DGAT1/DGAT2/TOMM40* KD HepG2 cell incubated in 10% FBS or LPDS serum for 48 hrs.
(I) Relative *MTTP, TM6SF2*, and *PPARGC1B* mRNA levels in HepG2 cells transfected with NTC vs. *TOMM40* siRNA, as measured by qPCR.
For all: *p<0.05, **p<0.01, ***p<0.005, ****p<0.001 vs. NTC by one-way ANOVA, with post-hoc Student's t-test to identify differences between groups. p<0.05 for *a* vs. *b* vs. *c* by two-way ANOVA, with Sidak's multiple comparisons test. Data are represented as mean ± SEM. (*n=3* biological replicates)

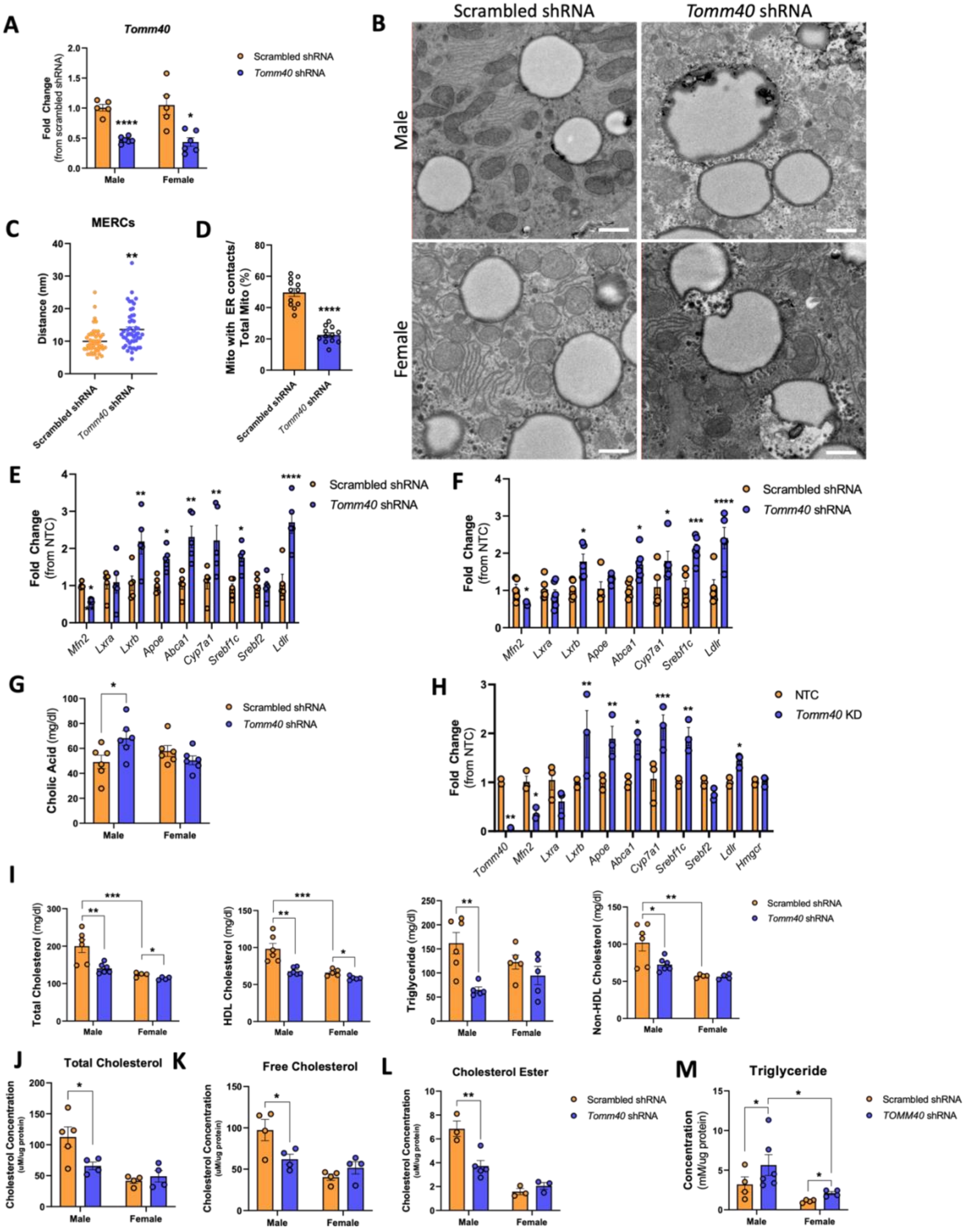

Figure 3-6. AAV8-T*omm40* shRNA injected C57BL/6J mice show reduced plasma cholesterol and triglyceride levels.

(A) Relative mRNA transcript levels of *Tomm40* confirming KD in male and female mice of ~60%, quantified by qPCR. (n=5-6 mice/sex/group)

(B) Representative TEM images of scrambled shRNA (control) vs. *Tomm40* shRNA in male and female, mice. Scale bars, 1μm.

(C-D) Analysis of MERCs using ImageJ software: (C) ER-mitochondria distance (nm), (N) length of MERCs (nm), (D) percentage of mitochondria with ER contacts out of total mitochondria per cell. (*n= 12-48* fields)
(E-F) Relative mRNA transcript levels comparing scrambled vs. *Tomm40* shRNA mice in male (E) and female (F). (*n=4-6* mice/sex/group)
(G) Quantification of plasma cholic acid levels in scrambled vs. *Tomm40* shRNA, male and female mice, measured by ELISA. (*n=4-6* mice/sex/group)
(H) Relative mRNA transcript levels comparing NTC vs. *Tomm40* siRNA transfected primary hepatocytes derived from male C57BL/6J mice, quantified by qPCR. (*n=3* male mice/group)
(I) Plasma total cholesterol, HDL-cholesterol, and triglyceride from male and female mice were quantified with AMS Liasys 330 Clinical Chemistry Analyzer, and Non-HDL-cholesterol was calculated by subtracting HDL-cholesterol from total cholesterol levels. (*n=5-6* mice/sex/group)
(J-L) Hepatic total cholesterol (J), free cholesterol (K), and cholesterol ester (L) levels quantified from male and female mice liver, using Amplex Red Cholesterol Assay. (*n=4-6* mice/sex/group)
(M)Quantification of hepatic triglyceride levels in male and female mice livers, using EnzyChrom™ Triglyceride Assay. (*n=4-6* mice/sex/group)
For all: *p<0.05, **p<0.01, ***p<0.005, ****p<0.001 vs. NTC by one-way ANOVA, with post-hoc Student’s t-test to identify differences between groups. Data are represented as mean ± SEM.

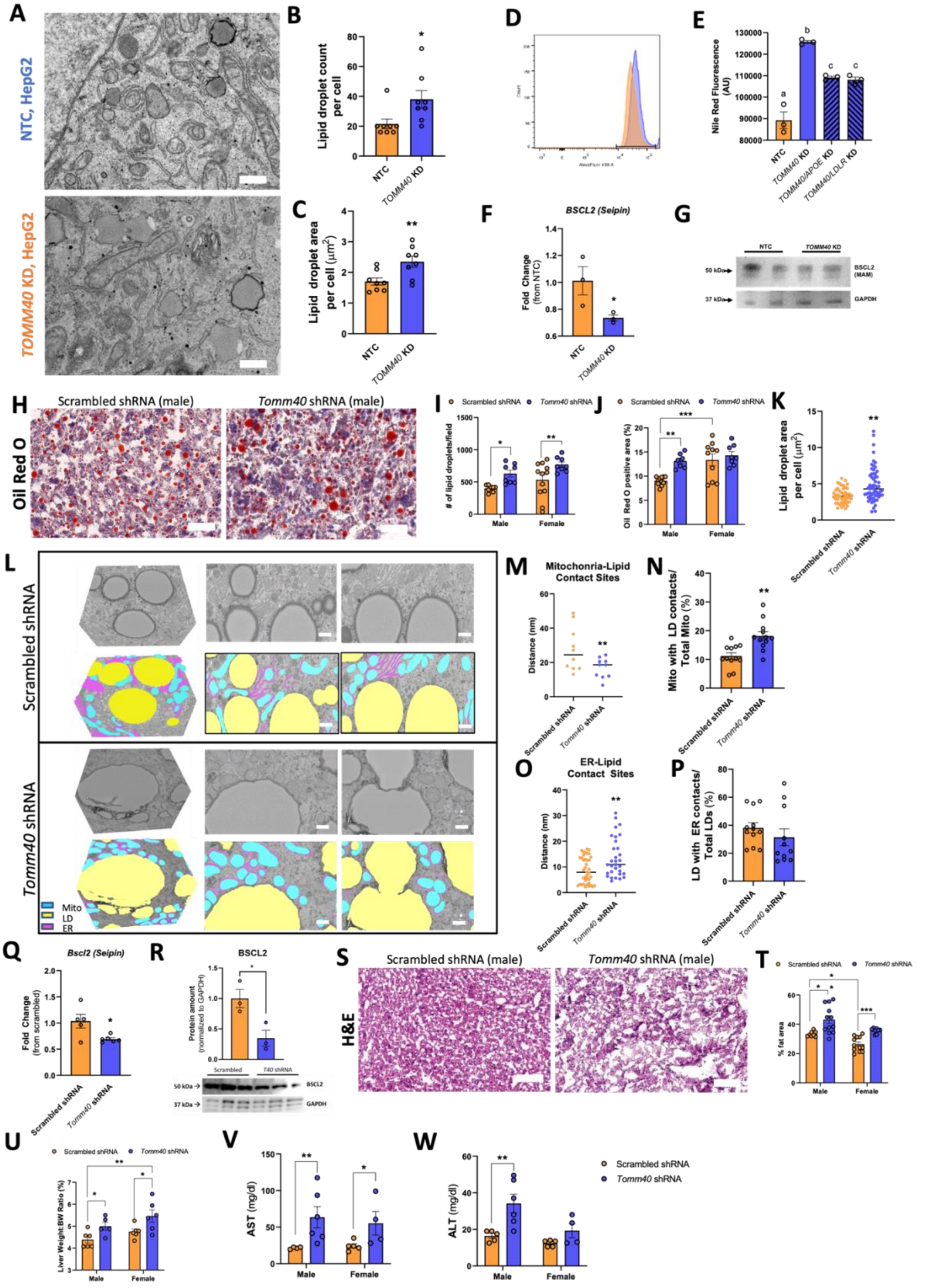

Figure 3-7. *TOMM40/Tomm40* KD induces lipid droplet accumulation and hepatic steatosis *in vivo*.

(A)Representative TEM images of lipid droplets in NTC vs. *TOMM40* KD HepG2 cells.

Scale bars, 1000 nm.
(B-C) Analysis of lipid droplets in HepG2 cells using ImageJ software: (B) lipid droplet count per cell, (C) average lipid droplet area per cell (μm^2). (*n= 8-12* cells)
(D) Representative flow cytometry histogram of NTC vs. *TOMM40* KD HepG2 cells. Neutral lipids were stained with Nile red.
(E) Analysis of flow cytometry data in NTC vs. *TOMM40* KD, singly and in combination with *APOE* and *LDLR* KD, HepG2 cells stained with Nile red. (*n=3* biological replicates)
(F) Relative mRNA transcript levels of *BSCL2* (Seipin) in NTC vs. *TOMM40* KD HepG2 cells. (*n=3* biological replicates)
(G) Representative western blot of BSCL2 protein expression in isolated MAMs of NTC vs. *TOMM40* KD HepG2 cells.
(H) Representative ORO images of scrambled vs. *Tomm40* shRNA male mouse liver (magnification x 400). Scale bars, 50 µm.
(I-J) Analysis of ORO staining using ImageJ software: (I) # of lipid droplets/field, (J) ORO positive area (%). (*n=10-15* fields/sex/group)
(K) Analysis of lipid droplet surface area (μm^2) in male mouse liver tissue using ImageJ software. (*n=24-48* fields)
(L) Representative FIB-SEM micrographs of 3D reconstructed and 2D slices from scrambled vs. *Tomm40* shRNA male mice liver. Segmentation analysis indicates mitochondria (blue), lipid droplets (yellow), and endoplasmic reticulum (purple). Scale bars, 1 µm.
(M-P) Analysis of organelle contact sites in scrambled vs. *Tomm40* shRNA male mice liver from TEM images using ImageJ software: (M) mitochondria-lipid contact site distance (nm), (N) percentage of mitochondria with lipid droplet contacts out of total mitochondria (%), (O) ER-lipid contact site distance (nm), (P) percentage of lipid droplets with an ER contact site out of total lipid droplets (%). (*n=10-40* fields)
(Q) Relative mRNA transcript levels of *Bscl2* (Seipin) in scrambled vs. *Tomm40* shRNA male mice livers. (*n=5-6* mice/group)
(R) Relative protein amount and representative western blot of BSCL2 protein expression in isolated MAMs of scrambled vs. *Tomm40* shRNA male mice livers.
(S) Representative hematoxylin-eosin stained images of scrambled vs. *Tomm40* shRNA male mouse livers (magnification x 400). Scale bars, 50 µm.
(T) Analysis of % fat area/field in hematoxylin-eosin stained liver samples using ImageJ software. (*n=10-15* fields/sex/group)
(U) Liver weight-to-body weight ratio (%) of scrambled vs. *Tomm40* shRNA mice. (*n=5-6* mice/sex/group)
(V-W) Plasma AST and ALT from male and female mice were quantified with AMS Liasys 330 Clinical Chemistry Analyzer. (*n=5-6* mice/sex/group)
For all: *$p<0.05$, **$p<0.01$, ***$p<0.005$, ****$p<0.001$ vs. NTC by one-way ANOVA, with post-hoc Student's t-test to identify differences between groups. Data are represented as mean ± SEM.

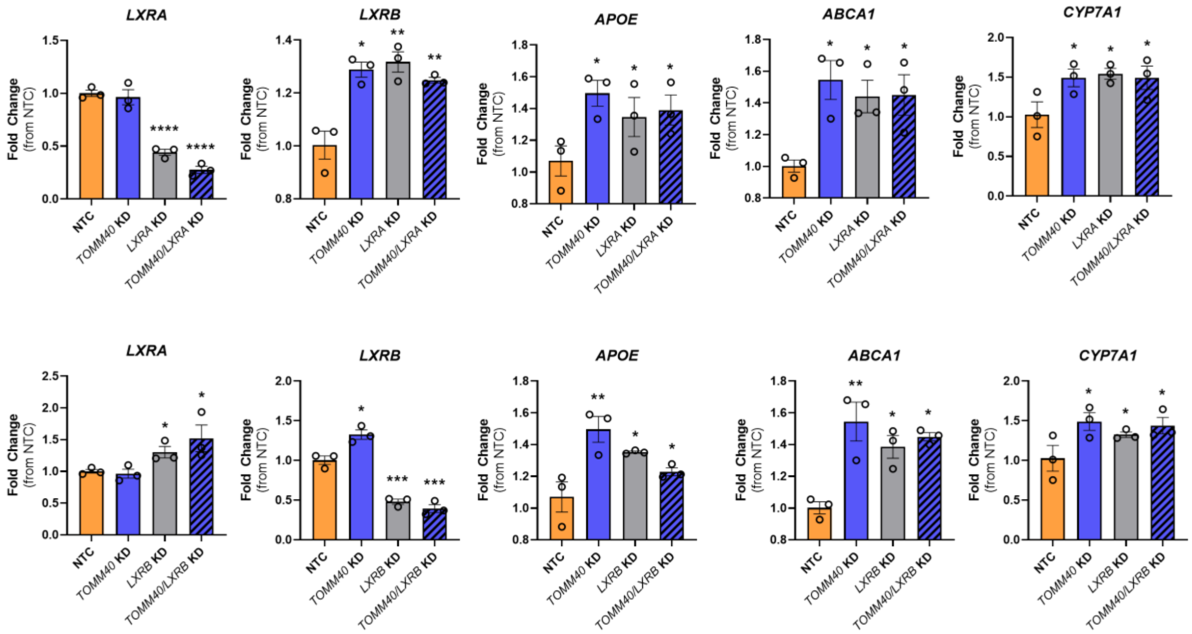

Figure 3-S1. LXRA and LXRB isoforms reciprocally maintain LXR expression and regulate downstream gene targets. Relative mRNA transcript levels *of LXRA, LXRB, APOE, ABCA1*, and *CYP7A1*, compared between NTC vs. *TOMM40, LXRA, LXRB siRNA*s, singly or in combination, in HepG2 cells. *p<0.05, **p<0.01, ***p<0.005, ****p<0.001 vs. NTC by one-way ANOVA, with post-hoc Student's t-test. (*n=3* biological replicates)

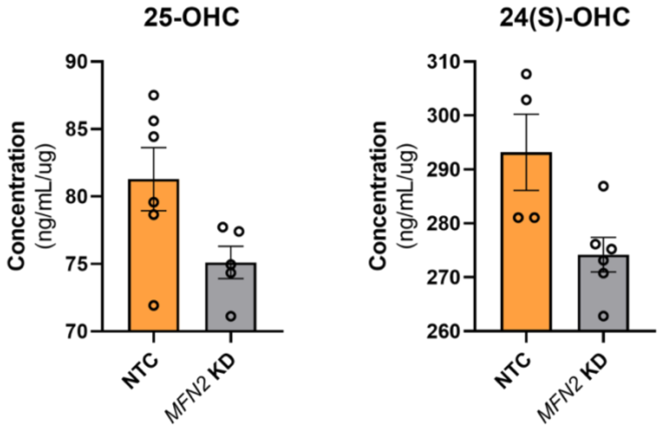

Figure 3-S2. *MFN2* KD does not affect enzymatic-derived oxysterols in HepG2 cells. Analysis of enzymatic-derived 25-OHC levels and 24(S)-OHC in *TOMM40* KD vs. NTC HepG2 cells by ELISAs. (*n=3* biological replicates)

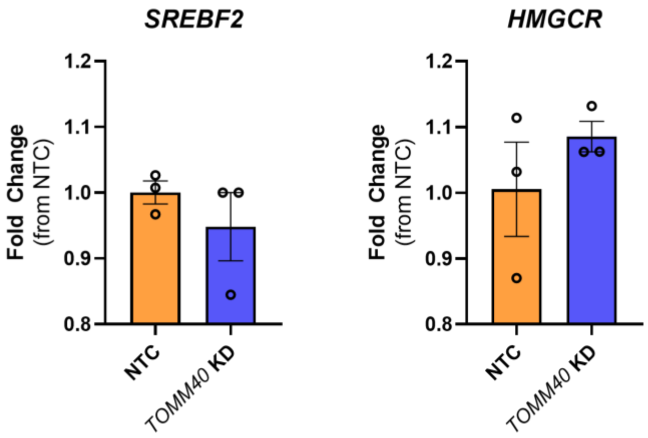

Figure 3-S3. *TOMM40* KD does not affects *SREBF2* or *HMGCR* mRNA transcript levels in HepG2 cells. (*n=3* biological replicates)

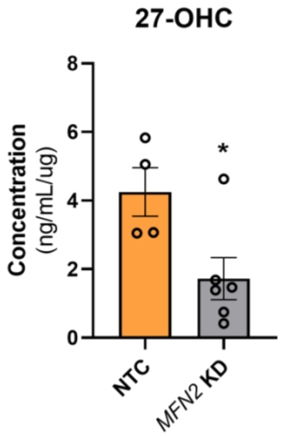

Figure 3-S4. *MFN2* KD reduces 27-OHC levels in HepG2 cells. Analysis of enzymatic-derived 27-OHC levels in NTC vs. *TOMM40* KD HepG2 cells by ELISA. *p<0.05 vs. NTC by one-way ANOVA, with post-hoc Student's t-test. (n=3 biological replicates)

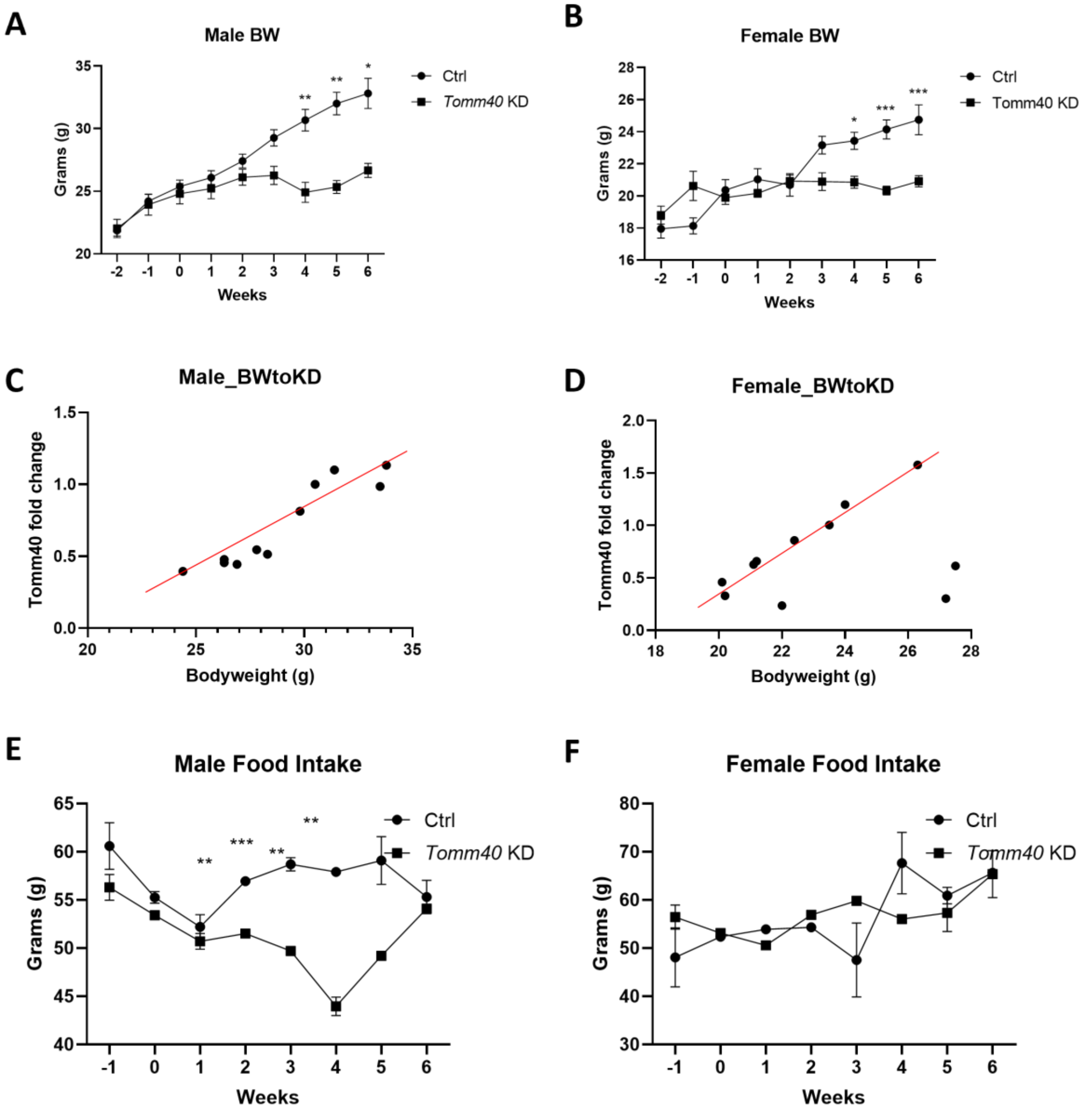

Figure 3-S5. Body weight and food intake measurements of AAV8-*Tomm40* shRNA C57BL/6J mice. (A-B) Weekly bodyweight of male (A) and female (B) scrambled vs. *Tomm40* shRNA mice. (C-D) Comparison between *Tomm40* KD: bodyweight ratio in male (C) and female (D) mice. (E-F) Weekly food intake of male (E) and female (F) mice. *p<0.05, **p<0.01, ***p<0.005, ****p<0.001 vs. NTC by one-way ANOVA, with post-hoc Student's t-test. (*n=6* mice/sex/group)

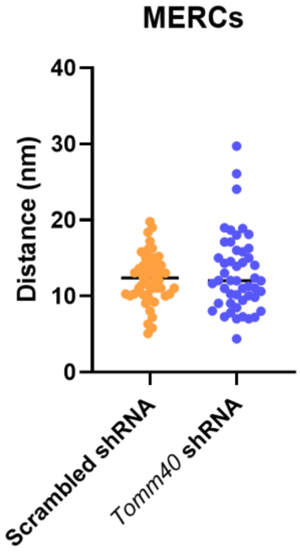

Figure 3-S6. Analysis of distance (nm) between MERCs in AAV8-*Tomm40* shRNA C57BL/6J female mice liver. TEM images were analyzed by ImageJ software. (*n= 24-48* fields)

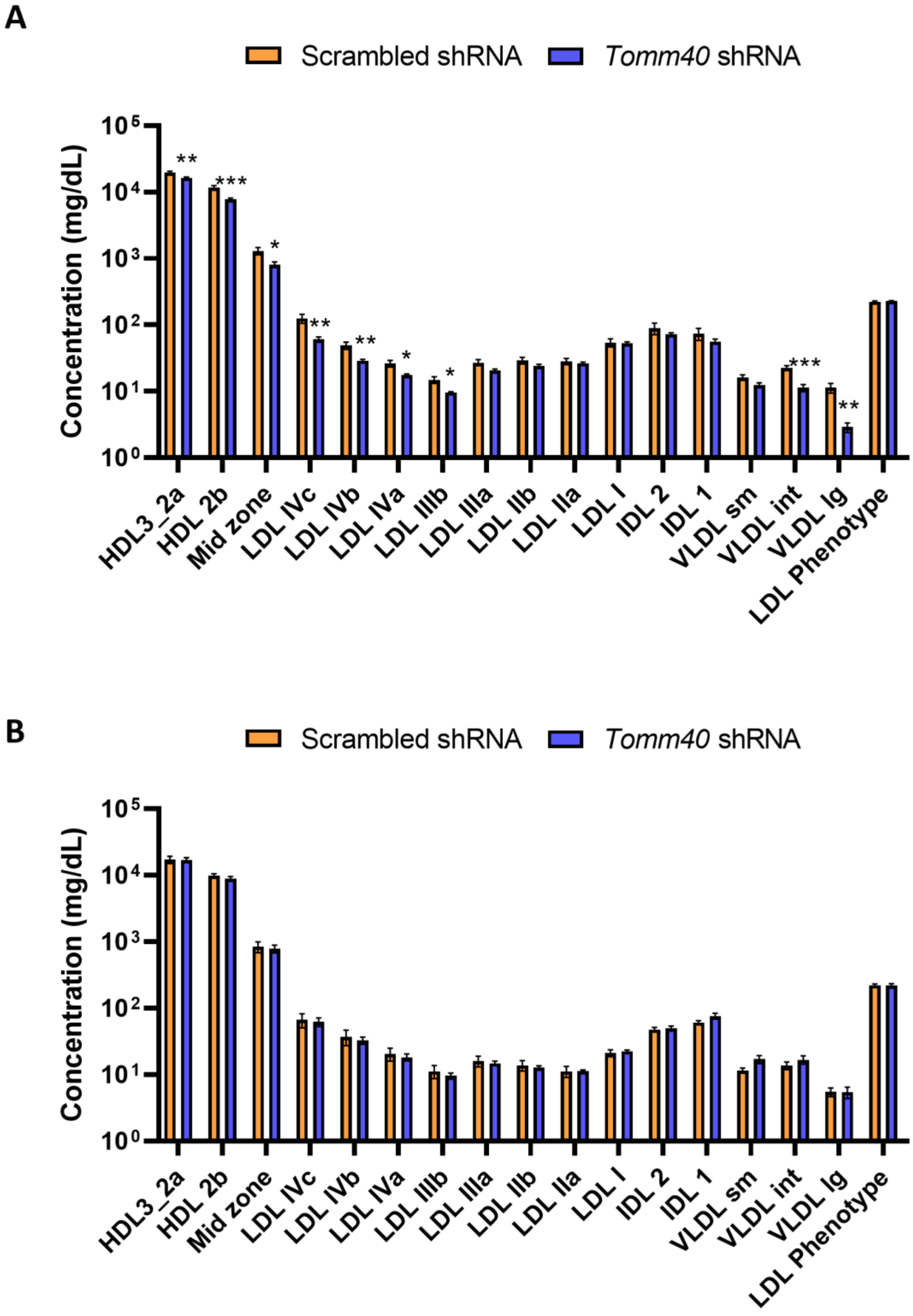

Figure 3-S7. Measurements of lipoprotein particle concentrations on mouse plasma. Lipoprotein concentrations were quantified by ion mobility in (A) male and (B) female mouse plasma in *Tomm40* KD vs. scrambled control. Mouse plasma lipoprotein subfractions were

analyzed based on human clinical lipoprotein particle classifications. *$p<0.05$, **$p<0.01$, ***$p<0.005$, ****$p<0.001$ vs. NTC by one-way ANOVA, with post-hoc Student's t-test. (n=6 mice/sex/group)

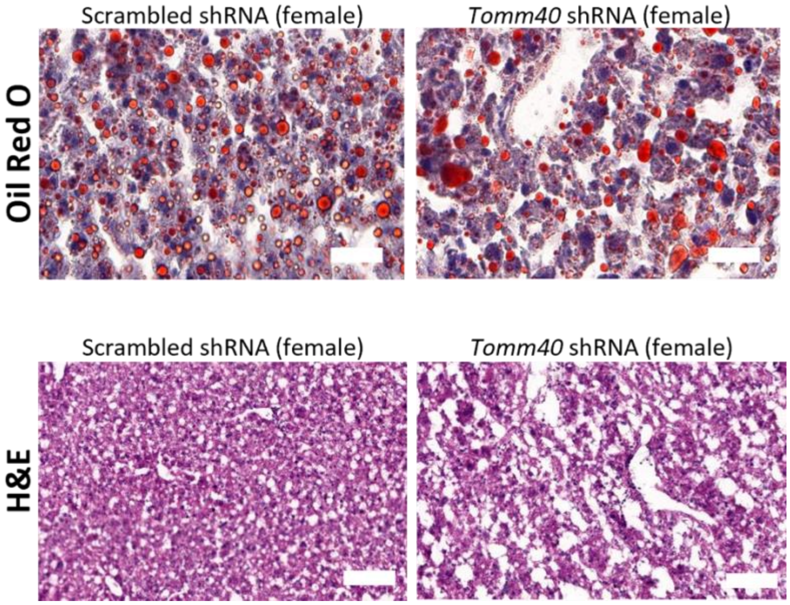

Figure 3-S8. Representative Oil Red O and Hematoxylin-Eosin stained liver samples of female mice. (400 x magnification) Scale bars, 50 µm.

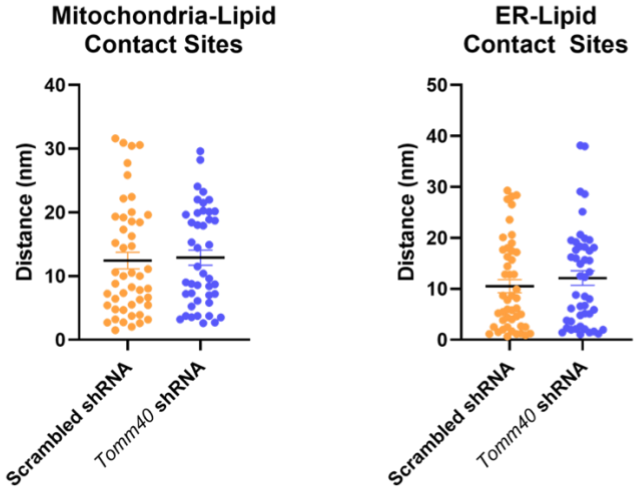

Figure 3-S9. Analysis of TEM micrographs indicating no differences in lipid droplet-ER and lipid-droplet mitochondria contact sites in female mice. (A) Distance between mitochondria and lipid contact sites (nm), (B) Distance between ER and lipid contact sites (nm). (*n=24-48* fields)

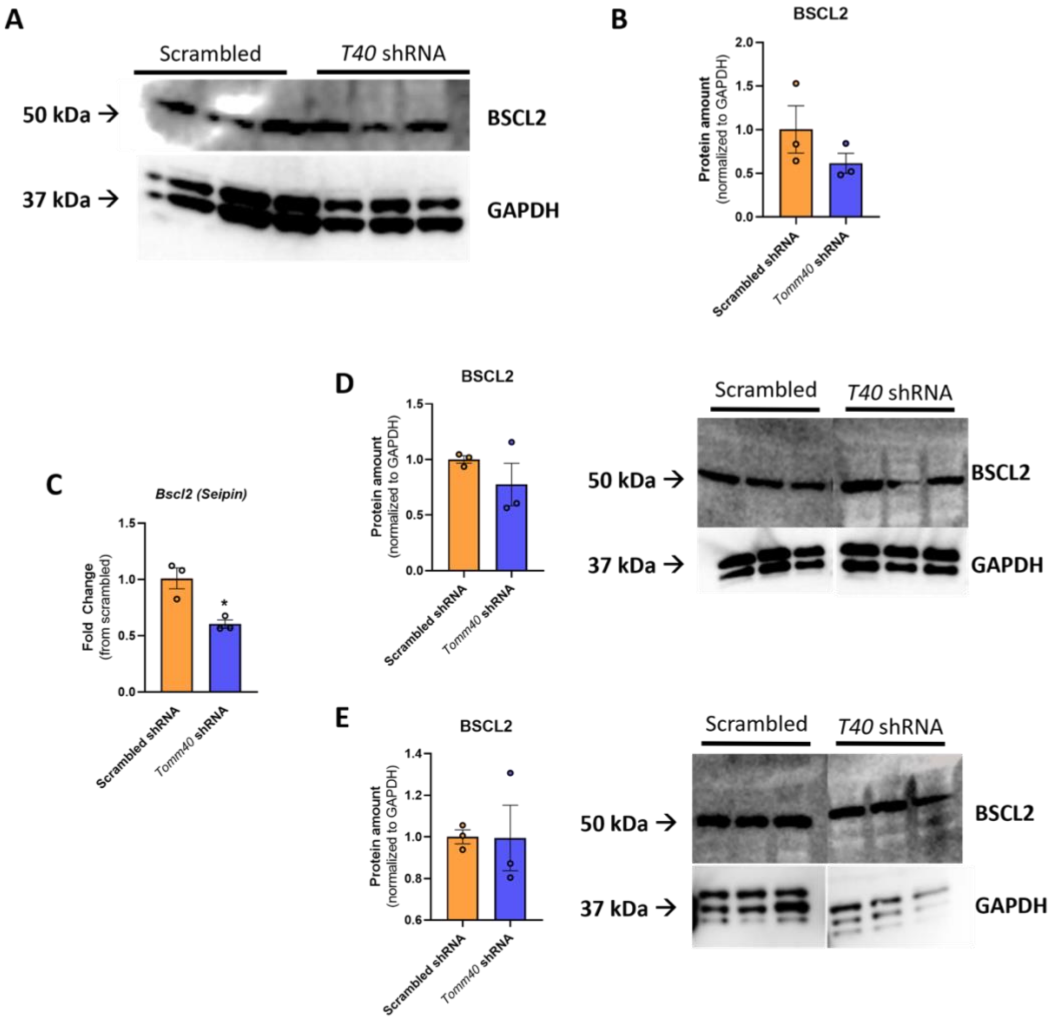

Figure 3-S10. Quantification of *Bscl2*/BSCL2 expression in mouse hepatic tissues. (A) Representative western blot and (B) relative protein amount of BSCL2 protein expression in cytosolic fractions of scrambled vs. *Tomm40* shRNA male mice liver. (C) mRNA transcript levels of Bscl2 in scrambled vs. *Tomm40* shRNA female mice liver. Relative protein amount and representative western blot of BSCL2 protein expression in (D) mitochondria-associated membranes (MAMs) and (E) cytosolic fractions in scrambled vs. *Tomm40* shRNA female mice livers. For all: *n=3* mice per group; *p<0.05, vs. scrambled shRNA by one-way ANOVA, with post-hoc Student's t-test to identify differences between groups. Data are represented as mean ± SEM.

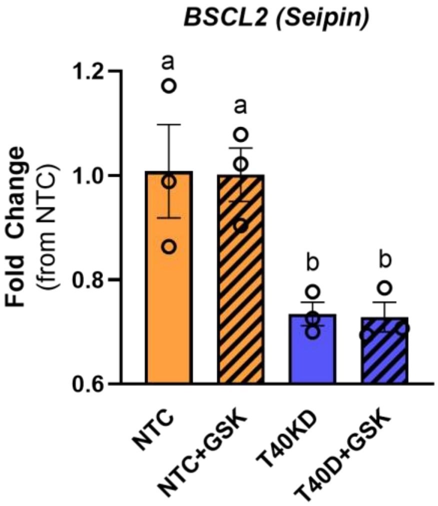

Figure 3-S11. mRNA transcript levels of *BSCL2* in HepG2 cells. mRNA transcripts of *BSCL2* from NTC vs. TOMM40 KD HepG2 cells with or without addition of GSK2033 were quantified by qPCR. p<0.05 for *a* vs. *b* vs. *c* vs. *d* by two-way ANOVA, with Sidak's multiple comparisons test. (n=3 biological replicates)

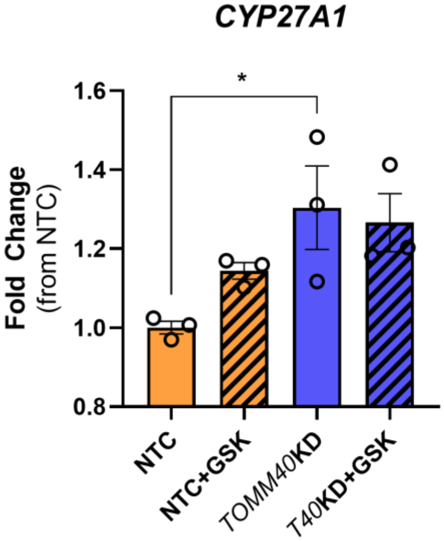

Figure 3-S12. *CYP27A1* mRNA transcript levels. mRNA transcripts of *CYP27A1* from NTC vs. TOMM40 KD HepG2 cells with or without addition of GSK2033 were quantified by qPCR. *p<0.05 vs. NTC by one-way ANOVA, with post-hoc Student's t-test. (n=3 biological replicates)

CHAPTER 4: FINAL CONCLUSION

With increasing evidence revealing mitochondrial dysfunction to play a critical role in metabolic diseases including, diabetes, obesity, and MASLD, our investigation on TOMM40 further supports a molecular mechanism linking mitochondria and lipid metabolism[198]. TOMM40 is the channel-forming subunit of the TOM complex required for importing precursor proteins into the mitochondria[199]. Moreover, TOMM40 has recently been shown to interact with key proteins located on the ER lumen and outer mitochondrial membrane that regulate mitochondria and lipid metabolism[33,39,41]. By exploring mitochondria-ER contact sites (MERCs), we have revealed two major findings in regard to TOMM40; its role in mediating statin-associated myopathy in skeletal myotubes, and in regulating lipid and cholesterol metabolism in the liver.

While highly effective and generally well-tolerated, statins can induce clinically significant myopathy, an effect that has been attributed in part to impairment of mitochondrial function, although the underlying mechanism remains unclear. In Chapter 2, we here report *TOMM40* and *TOMM22* are downregulated by simvastatin in C2C12 and human skeletal muscle cells and show for the first time that knockdown of these genes in myotubes impairs mitochondrial oxidative function, increases mitochondrial superoxide production, reduces mitochondrial cholesterol and CoQ levels, promotes increased mitochondrial fission and decreased fusion, and increases mitophagy - effects that were also observed with simvastatin exposure. Importantly, we also demonstrate that the adverse mitochondrial effects of simvastatin treatment are rescued by overexpression of *TOMM40* in conjunction with *BCAP31*, a protein that interacts with TOMM40 at MERCs whose expression is also downregulated by statin treatment. Together these findings identify down-regulation of key components of MERCs as a novel mechanism for statin-induced mitochondrial dysfunction that could contribute significantly to the development myopathy.

In addition to TOMM40's connection to cholesterol metabolism via statin therapy in skeletal muscle, TOMM40 sits adjacent to that for APOE, a protein with central functions in lipid and lipoprotein transport, and recent GWAS studies have shown that a number of SNPs in linkage disequilibrium between these two genes are significantly associated with plasma lipid levels[23,24]. While these associations have generally been attributed to *APOE*, no previous studies have addressed the possibility that TOMM40 has an independent effect on lipid metabolism. In Chapter 3, we show that knockdown of *TOMM40* in hepatocytes promotes increased expression of both the LDL receptor (LDLR) and *APOE*, and that these effects are responsible for mediating increased cellular uptake of LDL and VLDL particles. Consistent with these findings, knockdown of *TOMM40 in vivo* in mice results in substantial reductions in plasma lipid levels. Moreover, we show that in conjunction with enhanced hepatic lipoprotein uptake, *TOMM40* knockdown results in increased intracellular triglyceride content, size and number of lipid droplets, and development of hepatic steatosis.

Our investigation of molecular mechanisms underlying the effects of *TOMM40* knockdown on lipid metabolism has revealed a number of novel findings, including a key role for the LXR transcription factor due both to transcriptional upregulation and increased activation by oxysterols that are generated by mitochondria-induced reactive oxygen species. Through LXR activation, intracellular cholesterol was depleted via ABCA1-mediated cholesterol efflux and by synthesis and secretion of oxysterol-derived cholic acid. As a central theme of this dissertation, we have shown that the LXR-mediated effects described are due to the disruption of MERCs, where TOMM40 plays a key role, leading to increased lipid droplet-mitochondria contact sites in the liver *in vivo* and *in vitro*. Together these findings show for the first time that TOMM40 impacts both hepatic and plasma lipid concentrations, and, more generally, identify mechanisms that connect cellular energy and lipid metabolism via TOMM40 at MERCs.

The work presented in this dissertation provides insight into the intricacies of mitochondrial protein encoding genes, including TOMM40, and their effect on cholesterol and lipid metabolism via MERCs. While it is clear that TOMM40 plays a critical role in statin-associated myopathy and lipid metabolism, with the widespread use of statins[200] and growing attention to the role of mitochondria in multiple disease processes, requires further studies aimed at ameliorating myopathy risk by targeting this pathway. In the same way, further understanding of *TOMM40* effects on both brain lipid metabolism and *APOE* expression may yield new insights into the interrelated roles of this gene pair in the development of Alzheimer’s disease.

REFERENCES

1. Gidding, S.S. & Allen, N.B. Cholesterol and atherosclerotic cardiovascular disease: a lifelong problem. *J Am Heart Assoc* **8**(11), e012924 (2019).
2. Castelli, W.P. *et al*. Lipids and risk of coronary heart disease. The Framingham Study. *Ann Epidemiol* **2**, 23-8 (1992).
3. Goldstein, J.L. & Brown, M.S. A century of cholesterol and coronaries: From plaques to genes to statins. *Cell* **161**(1), 161-72 (2015).
4. Maxfield, F.R. & Tabas, I. Role of cholesterol and lipid organization in disease. *Nature* **438**, 612-21 (2005).
5. Van der Wulp, M.Y.M., Verkade, H.J. & Groen, A.K. Regulation of cholesterol homeostasis. *Mol Cell Endocrinol* **368**, 1-16 (2013).
6. Hajar, R. Statins: Past and present. *Heart Views* **12**(3), 121-7 (2011).
7. Ye, J. & DeBose-Boyd, R.A. Regulation of cholesterol and fatty acid synthesis. *Cold Spring Harb Perspect Biol* **3**(7), a004754 (2011).
8. Taylor, B.A. & Thompson, P.D. Statin-associated muscle disease: Advances in diagnosis and management. *Neurotherapeutics* **15**(4), 1006-17 (2018).
9. Tomaszewski, M. *et al*. Statin-induced myopathies. *Pharmacol Rep* **63**(4), 859-66 (2011).
10. Apostolopoulou, M. & Roden, M. The role of mitochondria in statin-induced myopathy. *Eur J Clin Invest* **45**(7), 745-54 (2015).
11. Stroes, E.S. *et al*. Statin-associated muscle symptoms: impact on statin therapy-European Atherosclerosis Society Consensus Panel Statement on Assessment, Aetiology and Management. *Eur Heart J* **36**(17), 1012-22 (2015).
12. Bouitbir, J. *et al*. Opposite effects of statins on mitochondria of cardiac and skeletal muscles: a 'mitohormesis' mechanism involving reactive oxygen species and PGC-1. *Eur Heart J* **33**(11), 1397-408 (2012).
13. Kauffmann, P. *et al*. Toxicity of statins on rat skeletal muscle mitochondria. *Cell Mol Life Sci* **63**, 2415-25 (2006).
14. Nakahara, K. *et al*. Myopathy induced by HMG-CoA reductase inhibitors in rabbits: a pathological, electrophysiological, and biochemical study. *Toxicol Appl Pharmacol* **152**, 99-106 (1998).
15. Vaughan, R.A. *et al*. Ubiquinol rescues simvastatin-suppression of mitochondrial content, function and metabolism: implications for statin-induced rhabdomyolysis. *Eur J Pharmacol* **711**, 1-9 (2013).
16. Parker, B.E. *et al*. Effect of statins on skeletal muscle function. *Circulation* **127**, 96-103 (2013).
17. Stringer, H.A., Sohi, G.K., Maguire, J.A., and Cote, H.C. Decreased skeletal muscle mitochondrial DNA in patients with statin-induced myopathy. *J Neurol Sci* **325**, 142-7 (2013).
18. Theusch, E. *et al*. Statin-induced expression change of *INSIG1* in lymphoblastoid cell lines correlates with plasma triglyceride statin response in a sex-specific manner. *Pharmacogenomics J* **17**, 222-9 (2017).

19. Gottzchalk, W.K. *et al*. The broad impact of TOM40 on neurodegenerative diseases in aging. *J Parkinsons Dis Alzheimers Dis* **1**(1), 12 (2014).
20. Grunwald, S.A. *et al*. Statin-induced myopathic changes in primary human muscle cells and reversal by a prostaglandin F2 alpha analogue. *Sci Reps* **10**, 3158 (2020).
21. Billing, O., Kao, G. & Naredi, P. Mitochondrial function is required for secretion of DAF-28/insulin in C. Elegans. *PloS ONE* **6**, e14507 (2011).
22. Bertolin, G. *et al*. The TOMM machinery is a molecular switch in PINK1 and PARK2/PARKIN-dependent mitochondrial clearance. *Autophagy* **9**, 1801-17 (2013).
23. Bekris, L.M., Lutz, F. & Yu, C.E. Functional analysis of APOE locus genetic variation implicates regional enhancers in the regulation of both TOMM40 and APOE. *J Human Genet* **57**, 18-25 (2012).
24. Soyal, S.M. *et al*. A TOMM40/APOE allele encoding APOE-E3 predicts high likelihood of late-onset Alzheimer's disease in autopsy cases. *Mol Genet Genomic Med* **8**(8), e1317 (2020).
25. Ferencz, C., Karlsson, S. & Kalpouzos, G. Promising genetic biomarkers of preclinical Alzheimer's disease: The influence of APOE and TOMM40 on brain integrity. *Int J Alzheimers Dis* (2012).
26. Elustondo, P., Martin, L.A. & Karten, B. Mitochondrial cholesterol import. *Biochim Biophys Acta – Mol Cell Biol Lipids* **1862**, 90-101 (2017).
27. Solsona-Vilarrasa, E. *et al*. Cholesterol enrichment in liver mitochondria impairs oxidative phosphorylation and disrupts the assembly of respiratory supercomplexes. *Redox Biol* **24** (2019).
28. Asalla, S. *et al*. Restoring mitochondrial function: A small molecule-mediated approach to enhance glucose stimulated insulin secretion in cholesterol accumulated pancreatic beta cells. *Sci Reps* **6**, 27513 (2016).
29. Brooks, S.W., Dykes, A.C. & Schreurs, B.G. A high-cholesterol diet increases 27-hydroxycholesterol and modifies estrogen receptor expression and neurodegeneration in rabbit hippocampus. *J Alzheimers Dis* **56**(1), 185-96 (2017).
30. Lange, Y. *et al*. Regulation of fibroblast mitochondrial 27-hydroxycholesterol production by active plasma membrane cholesterol. *J Lipid Res* **50**(9), 1881-8 (2009).
31. Pandak, W.M. *et al*. Transport of cholesterol into mitochondria is rate-limiting for bile acid synthesis via the alternative pathway in primary rat hepatocytes. *J Biol Chem* **227**(50), P48158-64 (2002).
32. Goicoechea, L. *et al*. Mitochondrial cholesterol: Metabolism and impact on redox biology and disease. *Redox Biol* **61**, 102643 (2023).
33. Larsen, M.C., Lee, J., Jorgensen, J.S. & Jefcoate, C.R. STARD1 functions in mitochondrial cholesterol metabolism and nascent HDL formation. Gene expression and molecular mRNA imaging show novel splicing and a 1:1 mitochondrial association. *Front Endocrinol (Lausanne)* **11**, 559674 (2020).

34. Caron, K.M. *et al*. Targeted disruption of the mouse gene encoding steroidogenic acute regulatory protein provides insights into congenital lipoid adrenal hyperplasia. *Proc Natl Acad Sci USA* **94**, 11540-45 (1997).
35. Martinvalet, D. The role of the mitochondria and the endoplasmic reticulum contact sites in the development of the immune responses. *Cell Death & Dis* **9**, 336 (2018).
36. Yang, M. *et al*. Mitochondria-associated ER membranes – the origin site of autophagy. *Front Cell Deve Biol* **8**, 595 (2020).
37. Csordas, G., Weaver, D. & Hajnoczky, G. Endoplasmic reticulum-mitochondrial contactology: structure and signaling functions. *Trends Cell Biol* **28**, 523-40 (2018).
38. Rowland, A.A. & Voletz, G.K. Endoplasmic reticulum-mitochondria contacts: Function of the junction. *Nat Rev Mol Cell Biol* **13**, 607-15 (2012).
39. Namba, T. BAP31 regulates mitochondrial function via interaction with Tom40 within ER-mitochondria contact sites. *Sci Adv* **5**(6), eaaw1386 (2019).
40. Torres, S., Garcia-Ruiz, C.M. & Fernandez-Checa, J.C. Mitochondrial cholesterol in Alzheimer's disease and Niemann-Pick Type C disease. *Front Neurol* **10**, 1168 (2019).
41. Hansson Peterson, C.A. *et*. *al*. The amyloid β-peptide is imported into mitochondria via the TOM import machinery and localized to mitochondrial cristae. *Proc Natl Acad Sci USA* **105**, 13145-50 (2008).
42. Patergnani, S. *et al*. Calcium signaling around mitochondria associated membranes (MAMs). *Cell Commun Signal* **9**, 19 (2011).
43. Camara, A.K.S. *et al*. Mitochondrial VDAC1: a key gatekeeper as potential therapeutic target. *Front Physiol* **8**, 460 (2017).
44. Martucciello S., Masullo, M., Cerulli, A. & Piacente, S. Natural products targeting ER stress, and the functional link to mitochondria. *Int J Mol Sci* **21**(6), 1905 (2022).
45. Fernandez, A. *et al*. ASMase is required for chronic alcohol induced hepatic endoplasmic reticulum stress and mitochondrial cholesterol loading. *J Hepatol* **59**, 805-13 (2013).
46. King, S.R. & Stocco, D.M. Steroidogenic acute regulatory protein expression in the central nervous system. *Front Endocrinol* **2**, 72 (2011).
47. Hedskog, L. *et al*. Modulation of the endoplasmic reticulum-mitochondria interface in Alzheimer's disease and related models. *PNAS* **110**(19), 7916-21 (2013).
48. Heinemeyer, T., Stemmet, M., Bardien, S. & Neethling, A. Underappreciated roles of the translocase of the outer and inner mitochondrial membrane protein complexes in human disease. *DNA Cell Biol* **38** (2019).

49. Zeng, Y. *et al*. Impaired mitochondrial fusion and oxidative phosphorylation triggered by high glucose is mediated by Tom22 in endothelial cells. *Oxidative Med Cell Longev* **2019**: 4508762 (2019).
50. Peng, K.Y. *et al*. Mitochondrial dysfunction-related lipid changes occur in nonalcoholic fatty liver disease progression. *J Lipid Res* **59**(10), 1977-86 (2018).
51. Koliaki, C. *et al*. Adaptation of hepatic mitochondrial function in humans with non-alcoholic fatty liver is lost in steatohepatitis. *Cell Metab* **21**, 739-46 (2015).
52. Rolo, A.O., Teodoro, J.S & Palmeira, C.M. Role of oxidative stress in the pathogenesis of nonalcoholic steatohepatitis. *Free Radic Biol Med* **52**, 59-69 (2012).
53. Moschandrea, C. *et al*. Mitochondrial dysfunction abrogates dietary lipid processing in enterocytes. *Nature* **625**, 385-92 (2024).
54. Mangravite, L.M., Wilke, R.A., Zhang, J., & Krauss, R.M. Pharmacogenomics of statin response. *Curr Opin Mol Ther* **10**(6), 555-61 (2008).
55. Ezad S, Cheema H, Collins N. Statin-induced rhabdomyolysis: a complication of a commonly overlooked drug interaction. *Oxf Med Case Reports*. **2018**(3): omx104 (2018).
56. Ramachandran, R. & Wierzbicki, A.S. Statins, muscle disease and mitochondria. *J Clin Med*. **6**(8), 75 (2018).
57. Schirris TJJ, Renkema GH, Ritschel T, Willems PHGM, Smeitink JAM, Russel FGM. Statin-induced myopathy is associated with mitochondrial complex III inhibition. *Cell Met*. **22**, 399-407 (2015).
58. Capizzi, J.A. *et al*. Effect of statins on skeletal muscle function. *Circulation*. **127**, 96-103 (2013).
59. Ballard KD, Parker BA, Thompson PD. Increases in creatine kinase with atorvastatin treatment are not associated with decreases in muscular performance. **Atherosclerosis**. 2013; 230(1): 121-124.
60. Pitt, A.S. &Buchanan, S.K. A biochemical and structural understanding of TOM complex interactions and implications for human health and disease. *Cells*. **10**(5), 1164 (2021).
61. Truscott, K.N. *et al*. A J-protein is an essential subunit of the presequence translocase-associated protein import motor of mitochondria. *J Cell Biol*. **163**, 707-713 (2003).
62. van Wilpe, S. *et al*. Tom22 is a multifunctional organizer of the mitochondrial preprotein translocase. *Nature*. **401**(6752), 485-9 (1999).
63. Ahting, U. *et al*. TOM40, the pore-forming component of the protein-conducting TOM channel in the outer membrane of mitochondria. *J Cell Biol*. **153**(6), 1151-60 (2001).
64. Lazarou, M., Jin, S.M., Kane, L.A. & Youle, R.J. Role of PINK1 binding to the TOM complex and alternate intracellular membranes in recruitment and activation of the E3 ligase Parkin. *Dev Cell*. **22**(2), 320-33 (2012).
65. Mullen, P.J. *et al*. Effect of simvastatin on cholesterol metabolism in C2C12 myotubes and HepG2 cells, and consequences for statin-induced myopathy. *Biochem Pharmacol*. **79**(8), 1200-9 (2010).

66. Martin, L.A., Kennedy, B.E. & Karten, B. Mitochondrial cholesterol: mechanisms of import and effects on mitochondrial function. *J Bioenerg Biomembr*. **48**(2), 137-51 (2016).
67. Stefely, J.A. & Pagliarini, D.J. Biochemistry of mitochondrial Coenzyme Q biosynthesis. *Trends Biochem Sci*. **42**(10), 824-843 (2017).
68. Sebastian, D., Palacin, M. & Zorzano, A. Mitochondrial dynamics: coupling mitochondrial fitness with healthy aging. *Trends Mol Med*. **23**(3), 201-215 (2017).
69. Lemasters, J.J. Variants of mitochondrial autophagy: Types 1 and 2 mitophagy and micromitophagy (Type 3). *Redox Biol*. **2**, 749-54 (2014).
70. Singh, F. *et al*. PGC-1β modulates statin-associated myotoxicity in mice. *Arch Toxicol*. **93**, 487-504 (2019).
71. Bertolini, G. *et al*. The TOMM machinery is a molecular switch in PINK1 and PARK2/PARKIN-dependent mitochondrial clearance. *Autophagy*. **9**, 1801-17 (2013).
72. Yang, W. *et al*. TOM40 inhibits ovarian cancer cell growth by modulating mitochondrial function including intracellular ATP and ROS levels. *Cancers (Basel)*. **12**(5), 1329 (2020).
73. Zeitlow, K. *et al*. The biological foundation of the genetic association of *TOMM40* with late-onset Alzheimer's disease. *Biochim Biophys Acta*. **1863**(11), 2973-86 (2017).
74. Liu, Z. *et al*. Direct activation of BAX protein for cancer therapy. *Med Res Rev*. **32**, 313-341 (2016).
75. Curado, S. *et al*. The mitochondrial import gene tomm22 is specifically required for hepatocyte survival and provides a liver regeneration model. *Dis Model Mech*. **3**, 486-495 (2010).
76. Siemen, D. *et al*. Ca^{2+}-activated K channel of the BK-type in the inner mitochondrial membrane of a human glioma cell line. *Biochem Biophys Res Commun*. **257**, 549-554 (1999).
77. Middelberg, R.P.S. *et al*. Genetic variants in LPL, OASL and TOMM40/APOE-C1-C2-C4 genes are associated with multiple cardiovascular-related traits. *BMC Med Genet*. **12**, 123 (2011).
78. Olson, R.E. *et al*. Benzoate derivatives as intermediates in the biosynthesis of coenzyme Q in the rat. *J Biol Chem*. **238**, 3146-8 (1963).
79. Tai, J. *et al*. Hem25p is a mitochondrial IPP transporter. *bioRxiv*. **2023.03.14.532620**; doi: https://doi.org/10.1101/2023/03/14/532620.
80. Kalen, A., Appelkvist, E.L., Chojnacki, T. & Dallner, G. Nonaprenyl-4-hydroxybenzoate transferase, an enzyme involved in ubiquinone biosynthesis, in the endoplasmic reticulum-Golgi system of rat liver. *J Biol Chem*. **265**(2), 1158-64 (199).
81. Guerra, R.M. & Pagliarini, D.J. Coenzyme Q biochemistry and biosynthesis. *Trends Biochem Sci*. **48**(5), 463-76 (2023).
82. Liesa, M., Palacin, M. & Zorzano, A. Mitochondrial dynamics in mammalian health and disease. *Physiol Rev*. **89**(3), 799-845 (2009).

83. Ferree, A. & Shirihai, O. Mitochondrial dynamics: the intersection of form and function. *Adv Exp Med Biol*. **748**, 13-40 (2012).
84. Caldeira, D.A.F., Weiss, D.J. & Cruz, F.F. Mitochondria in focus: from function to therapeutic strategies in chronic lung diseases. *Front Immunol*. **12**, 78074 (2021).
85. Nasca, A., Scotton, C. & Ghezzi, D. Recessive mutations in *MSTO1* cause mitochondrial dynamics impairment, leading to myopathy and ataxia. *Hum Mutat*. **38**(8), 970-977 (2017).
86. Yu, R., Lendahl, U., Nister, M. & Zhao, J. Regulation of mammalian mitochondrial dynamics: opportunities and challenges. *Front Endocrinol*. **11**, 374 (2020).
87. Zhao, J., Lendahl, U., & Nister, M. Regulation of mitochondrial dynamics: convergences and divergences between yeast and vertebrates. *Cell Mol Life Sci*. **70**, 951076 (2013).
88. Mishra, P. & Chan D.C. Mitochondrial dynamics and inheritance during cell division, development and disease. *Nat Rev Mol Cell Biol*. **15**, 634-646 (2014).
89. Roy, M., Reddy, P.H., Iijima, M. & Sesaki, H. Mitochondrial division and fusion in metabolism. *Curr Opin Cell Biol*. 33, 111-8 (2015).
90. Wai, T. & Langer, T. Mitochondrial dynamics and metabolic regulation. *Trends Endocrinol Metab*. **27**(2), 105-117 (2016).
91. Song, M. *et al*. Mitochondrial fission and fusion factors reciprocally orchestrate mitophagic culling in mouse hearts and cultured fibroblasts. *Cell Metab*. **21**(2), 273-286 (2015).
92. Herrera-Cruz, M.S. & Simmen, T. Of yeast, mice and men: MAMs come in two flavors. *Biol Direct*. **12**(3), (2017).
93. Matsuda, N. *et al*. PINK1 stabilized by mitochondrial depolarization recruits Parkin to damaged mitochondria and activate latent Parkin for mitophagy. *J Cell Biol*. **189**, 211-21 (2010).
94. Narendra, D.P. *et al*. PINK1 is selectively stabilized on impaired mitochondria to activate Parkin. *PLoS Biol*. **8**, e1000298 (2010).
95. Geisler, S. *et al*. The PINK1/Parkin-mediated mitophagy is compromised by PD-associated mutations. *Autophagy*. **6**, 871-8 (2010).
96. Tanaka, A. *et al*. Proteasome and p97 mediate mitophagy and degradation of mitofusins induced by Parkin. *J Cell Biol*. **191**, 1367-80 (2010).
97. Wu, S., Zhou, F., Zhang, Z. & Xing, D. Mitochondrial oxidative stress causes mitochondrial fragmentation via differential modulation of mitochondrial fission-fusion proteins. *FEBS J*. **278**(6), 941-54 (2011).
98. Srinivasan, S., Guha, M., Kashina, A. & Avadhani, N.G. Mitochondrial dysfunction and mitochondrial dynamics-The cancer connection. *Biochim Biophys Acta Bioenerg*. **1858**(8), 602-614 (2017).
99. Cirigliano, A. *et al*. Statins interfere with the attachment of *S. cerevisiae* mtDNA to the inner mitochondrial membrane. *J Enzyme Inhib Med Chem*. **35**(1), 129-137 (2020).

100. Broniarek, I., Dominiak, K., Galganski, L. & Jarmuszkiewicz, W. The influence of statins on the anaerobic metabolism of endothelial cells. *Int J Mol Sci*. **21**(4), e1485 (2020).
101. Mollazadeh, H. *et al*. Effects of statins on mitochondrial pathways. *J Cachexia, Sarcop, Muscle*. **12**(2), 237-251 (2021).
102. Youle, R.J. & van der Bliek, A.M. Mitochondrial fission, fusion, and stress. *Science*. **337**(6098), 1062-5 (2012).
103. Manczak, M., Calking, M.J. & Reddy, P.H. Impaired mitochondrial dynamics and abnormal interaction of amyloid beta with mitochondrial protein Drp1 in neurons from patients with Alzheimer's disease: implications for neuronal damage. *Hum Mol Genet*. **20**(130), 2495-2509 (2011).
104. Panajatovic, M.V. *et al*. PGC-1α plays a pivotal role in simvastatin-induced exercise impairment in mice. *Acta Physiol*. **228**(4), e13402 (2019).
105. Fares, K., Abd-El-Hamid, H., Youssef, A. & Rafla, M. Statin-induced myopathy in muscles of lower limb with special reference to gastrocnemius muscle in albino rats. *QJM*. **111**, hcy200.082 (2018).
106. Zaleski, A.L., Taylor, B.A. & Thompson, P.D. Coenzyme Q10 as treatment for statin-associated muscle symptoms-A good idea, but…*Adv Nutr*. **9**(4), 519S-523S (2018).
107. Yamano, K. *et al*. Tom20 and Tom22 share the common signal recognition pathway in mitochondrial protein import. *J Biol Chem*. **283**(7), 3799-807 (2008).
108. Iwasawa, R. *et al*. Fis1 and Bap31 bridge the mitochondria-ER interface to establish a platform for apoptosis induction. *EMBO J*. **30**(3), 556-68 (2011).
109. Namba, T. *et al*. CDIP1-BAP31 complex transduces apoptotic signals from endoplasmic reticulum to mitochondria under endoplasmic reticulum stress. *Cell Rep*. **5**(2), 331-9 (2013).
110. Medina, M.W., *et al*. Alternative splicing of 3-hydroxy-3-methylglutaryl coenzyme A reductase is associated with plasma low-density lipoprotein cholesterol response to simvastatin. *Circulation*. **118**(4), 355-62 (2008).
111. Kauffman, M.E. *et al*. MitoSOX-based flow cytometry for detecting mitochondrial ROS. *React Oxyg Species (Apex)*. **2**(5), 361-370 (2016).
112. Wettmarshausen, J. & Perocchi, F. Isolation of functional mitochondria from cultured cells and mouse tissues. *Methods Mol Biol*. **1567**, 15-32 (2017).
113. Reynolds, E.S. The use of lead citrate at high pH as an electron-opaque stain in electron microscopy. *J Cell Biol*. **17**(1), 208-12 (1973).
114. Lam, J. *et al*. A universal approach to analyzing transmission electron microscopy with ImageJ. *Cells*. **10**(9), 2177 (2021).
115. Shults, N.V. *et al*. Ultrastructural changes of the right ventricular myocytes in pulmonary arterial hypertension. *J Am Heart Assoc*. **8**(5), e011227 (2019).
116. Quiros, P.M., Goyal, A. & Auwerx, J. Analysis of mtDNA/nDNA ratio in mice. *Curr Protoc Mouse Biol*. **7**(1), 47-54 (2017).
117. Bose, H. S., Bose, M., & Whittal, R. M. Tom40 in cholesterol transport. *iScience*. **26**(4), 106386 (2023).

118. Mise, A., *et al*. TOMM40 and APOE Gene Expression and Cognitive Decline in Japanese Alzheimer's Disease Subjects. *Journal of Alzheimer's disease : JAD*. **60**(3), 1107–1117 (2017).

119. Miao, L. *et al*. BCL3-PVRL2-TOMM40 SNPs, gene-gene and gene-environment interactions on dyslipidemia. *Sci Reps*. **8**(1), 6189 (2018).

120. Johnson, L. A. *et al.* Apolipoprotein E-low density lipoprotein receptor interaction affects spatial memory retention and brain ApoE levels in an isoform-dependent manner. *Neurobiol Dis*. **64**, 150–162 (2014).

121. Gui, W., Qiu, C., Shao, Q., & Li, J. Associations of Vascular Risk Factors, *APOE* and *TOMM40* Polymorphisms With Cognitive Function in Dementia-Free Chinese Older Adults: A Community-Based Study. *Front Psych*. **12,** 617773 (2021).

122. Selvaraj, M. S. *et al*. Whole genome sequence analysis of blood lipid levels in >66,000 individuals. *Nat Comms*. **13**(1), 5995 (2022).

123. Saito, S., & Mori, K. Detection and Quantification of Calcium Ions in the Endoplasmic Reticulum and Cytoplasm of Cultured Cells Using Fluorescent Reporter Proteins and ImageJ Software. *Bio-protocol*. **13**(16), e4738 (2023).

124. Zaman, M., & Shutt, T. E. The Role of Impaired Mitochondrial Dynamics in MFN2-Mediated Pathology. *Front Cell Dev Bio*. **10**, 858286 (2022).

125. Dentoni, G., Naia, L., & Ankarcrona, M. Mitochondria-Endoplasmic Reticulum Interplay Regulates Exo-Cytosis in Human Neuroblastoma Cells. *Cells*. **11**(3), 514 (2022).

126. Yang, J. F. *et al*. Mitochondria-ER contact mediated by MFN2-SERCA2 interaction supports CD8$^+$ T cell metabolic fitness and function in tumors. *Sci Immun*. **8**(87), eabq2424 (2023).

127. Gottschalk, B. *et al*. MFN2 mediates ER-mitochondrial coupling during ER stress through specialized stable contact sites. *Front Cell Dev Bio*. **10,** 918691 (2022).

128. Janowski, B. A. *et al*. Structural requirements of ligands for the oxysterol liver X receptors LXRalpha and LXRbeta. *PNAS USA*. **96**(1), 266–271 (1999).

129. Kim, H., Park, C., & Kim, T. H. Targeting Liver X Receptors for the Treatment of Non-Alcoholic Fatty Liver Disease. *Cells*. **12**(9), 1292 (2023).

130. Ferré, P., & Foufelle, F. SREBP-1c transcription factor and lipid homeostasis: clinical perspective. *Hormone research*. **68**(2), 72–82 (2007).

131. Chang, T. Y., Li, B. L., Chang, C. C., & Urano, Y. Acyl-coenzyme A:cholesterol acyltransferases. *Am J Physiol Endocrin Metab*. **297**(1), E1–E9 (2009).

132. Meex, S. J., Andreo, U., Sparks, J. D., & Fisher, E. A. Huh-7 or HepG2 cells: which is the better model for studying human apolipoprotein-B100 assembly and secretion?. *J Lip Res*. **52**(1), 152–158 (2011).

133. Smith, L. P. *et al.* The bile acid synthesis pathway is present and functional in the human ovary. *PloS one*. **4**(10), e7333 (2009).

134. Chiang, J. Y. L., & Ferrell, J. M. Up to date on cholesterol 7 alpha-hydroxylase (CYP7A1) in bile acid synthesis. *Liv Res*. **4**(2), 47–63 (2020).

135. Lumbreras, S. *et al.* Gene supplementation of *CYP27A1* in the liver restores bile acid metabolism in a mouse model of cerebrotendinous xanthomatosis. *Mol Therapy. Methods & Clin Dev*. **22**, 210–221 (2021).

136. Miller W. L. Steroidogenic acute regulatory protein (StAR), a novel mitochondrial cholesterol transporter. *Biochim Biophys Acta*. **1771**(6), 663–676 (2007).

137. Newberry, E. P., Strout, G. W., Fitzpatrick, J. A. J., & Davidson, N. O. Liver-specific deletion of Mttp versus Tm6sf2 reveals distinct defects in stepwise VLDL assembly. *J Lip Res*. **62,** 100080 (2021).

138. Chen, Z., Norris, J. Y., & Finck, B. N. Peroxisome proliferator-activated receptor-gamma coactivator-1alpha (PGC-1alpha) stimulates VLDL assembly through activation of cell death-inducing DFFA-like effector B (CideB). *J Bio Chem*. **285**(34), 25996–26004 (2010).

139. Issa, S. S., Shaimardanova, A. A., Solovyeva, V. V., & Rizvanov, A. A. Various AAV Serotypes and Their Applications in Gene Therapy: An Overview. *Cells*. **12**(5), 785 (2023).

140. Combot, Y. *et al.* Seipin localizes at endoplasmic-reticulum-mitochondria contact sites to control mitochondrial calcium import and metabolism in adipocytes. *Cell Reps*. **38**(2), 110213 (2022).

141. Bellanti, F., & Vendemiale, G. The Aging Liver: Redox Biology and Liver Regeneration. *Antioxid Redox Sig*. **35**(10), 832–847 (2021).

142. Alba, G. *et al.* 7-Keto-cholesterol and 25-hydroxy-1 cholesterol rapidly enhance ROS production in human neutrophils. *Eur J Nutr*. **55**(8), 2485–2492 (2016).

143. El-Sankary, W., Bombail, V., Gibson, G. G., & Plant, N. Glucocorticoid-mediated induction of CYP3A4 is decreased by disruption of a protein: DNA interaction distinct from the pregnane X receptor response element. *Drug Metab Disp*. **30**(9), 1029–1034 (2002).

144. Vaz, R. J. *et al.* Amelioration of PXR-mediated CYP3A4 induction by mGluR2 modulators. *BMC Letters*. **28**(19), 3194–3196 (2018).

145. Moldavski, O. *et al.* 4β-Hydroxycholesterol is a prolipogenic factor that promotes SREBP1c expression and activity through the liver X receptor. *J Lip Res*. **62**, 100051 (2021).

146. Hussein, M. A. *et al*. LXR-Mediated ABCA1 Expression and Function Are Modulated by High Glucose and PRMT2. *PloS one*. **10**(8), e0135218 (2015).

147. Schiffmann, A., Ahlswede, L., & Gimpl, G. Reversible translocation of acyl-CoA:cholesterol acyltransferase (ACAT) between the endoplasmic reticulum and vesicular structures. *Front Mol Biosci*. **10**, 1258799 (2023).

148. Grespi, F. *et al.* The Interplay of Microtubules with Mitochondria-ER Contact Sites (MERCs) in Glioblastoma. *Biomolecules*. **12**(4), 567 (2022).

149. Saito, H. *et al.* Hydroxylation site-specific and production-dependent effects of endogenous oxysterols on cholesterol homeostasis: Implications for SREBP-2 and LXR. *JBC*. **299**(1), 102733 (2023).

150. Ishimoto, K. *et al.* Identification of human low-density lipoprotein receptor as a novel target gene regulated by liver X receptor alpha. *FEBS Letters*. **580**(20), 4929–4933 (2006).
151. Oberkofler, H., Schraml, E., Krempler, F., & Patsch, W. Restoration of sterol-regulatory-element-binding protein-1c gene expression in HepG2 cells by peroxisome-proliferator-activated receptor-gamma co-activator-1alpha. *Biochem J*. **381**(2), 357–363 (2004).
152. Streicher, R. *et al.* SREBP-1 mediates activation of the low density lipoprotein receptor promoter by insulin and insulin-like growth factor-I. *JBC*. **271**(12), 7128–7133 (1996).
153. Madison B. B. Srebp2: A master regulator of sterol and fatty acid synthesis. *J Lip Res*. **57**(3), 333–335 (2016).
154. Goldstein, J. L., & Brown, M. S. A century of cholesterol and coronaries: from plaques to genes to statins. *Cell*. **161**(1), 161–172 (2015).
155. Zhang, L. *et al.* Significance and mechanism of CYP7a1 gene regulation during the acute phase of liver regeneration. *Mol Endocrin*. **23**(2), 137–145 (2009).
156. Lumbreras, S. *et al.* Gene supplementation of *CYP27A1* in the liver restores bile acid metabolism in a mouse model of cerebrotendinous xanthomatosis. *Mol Therapy. Methods Clin Dev*. **22**, 210–221 (2021).
157. Mertens, K. L., Kalsbeek, A., Soeters, M. R., & Eggink, H. M. Bile Acid Signaling Pathways from the Enterohepatic Circulation to the Central Nervous System. *Front Neurosci*. **11**, 617 (2017).
158. Kuroki, S., Muramoto, S., Kuramoto, T., & Hoshita, T. Sex differences in gallbladder bile acid composition and hepatic steroid 12 alpha-hydroxylase activity in hamsters. *J Lip Res*. **24**(12), 1543–1549 (1983).
159. Osuna-Prieto, F. J. *et al.* Plasma Levels of Bile Acids Are Related to Cardiometabolic Risk Factors in Young Adults. *J Clin Endocrin Metab*. **107**(3), 715–723 (2022).
160. Patton, M.E. *et al.* Sex differences in bile acid homeostasis and excretion underlie the disparity in liver cancer incidence between males and females. Preprint at *bioRxiv : the preprint server for biology* (2020).
161. Xu, L. *et al.* Chenodeoxycholic Acid (CDCA) Promoted Intestinal Epithelial Cell Proliferation by Regulating Cell Cycle Progression and Mitochondrial Biogenesis in IPEC-J2 Cells. *Antioxidants*. **11**(11), 2285 (2022).
162. Petrack, B., & Latario, B. J. Synthesis of 27-hydroxycholesterol in rat liver mitochondria: HPLC assay and marked activation by exogenous cholesterol. *J Lip Res*. **34**(4), 643–649 (1993).
163. Reitz, J., Gehrig-Burger, K., Strauss, J. F., 3rd, & Gimpl, G. Cholesterol interaction with the related steroidogenic acute regulatory lipid-transfer (START) domains of StAR (STARD1) and MLN64 (STARD3). *FEBS J*. **275(**8), 1790–1802 (2008).
164. Wilsie, L. C., Gonzales, A. M., & Orlando, R. A. Syndecan-1 mediates internalization of apoE-VLDL through a low density lipoprotein receptor-related

protein (LRP)-independent, non-clathrin-mediated pathway. *Lip Health Dis*. **5**, 23 (2006).

165. Windham, I. A. *et al*. APOE traffics to astrocyte lipid droplets and modulates triglyceride saturation and droplet size. *J Cell Bio*. **223**(4), e202305003 (2024).

166. Herker, E. *et al*. Lipid Droplet Contact Sites in Health and Disease. *Trends Cell Bio*. **31**(5), 345–358 (2021).

167. Sui, X. *et al*. Cryo-electron microscopy structure of the lipid droplet-formation protein seipin. *J Cell Bio*. **217**(12), 4080–4091 (2018).

168. Yan, R. *et al*. Human SEIPIN Binds Anionic Phospholipids. *Dev Cell*. **47**(2), 248–256.e4 (2018).

169. Krahmer, N. *et al*. Organellar Proteomics and Phospho-Proteomics Reveal Subcellular Reorganization in Diet-Induced Hepatic Steatosis. *Dev Cell*. **47**(2), 205–221.e7 (2018).

170. Talari, N. K. *et al*. Lipid-droplet associated mitochondria promote fatty-acid oxidation through a distinct bioenergetic pattern in male Wistar rats. *Nat Comms*. **14**(1), 766 (2023).

171. Wang, H. *et al*. FITM2 deficiency results in ER lipid accumulation, ER stress, reduced apolipoprotein B lipidation, and VLDL triglyceride secretion *in vitro* and in mouse liver. Preprint at *bioRxiv : the preprint server for biology*. 2023.12.05.570183 (2023).

172. Gao, G. *et al*. Control of lipid droplet fusion and growth by CIDE family proteins. *Biochimica et biophysica acta. Mol Cell Bio Lip*. **1862**(10), 1197–1204 (2017).

173. Jambunathan, S., Yin, J., Khan, W., Tamori, Y., & Puri, V. FSP27 promotes lipid droplet clustering and then fusion to regulate triglyceride accumulation. *PloS one*, **6**(12), e28614 (2011).

174. Chen, Y. *et al*. Pan-Cancer Analysis of the Associations of TGFBI Expression With Prognosis and Immune Characteristics. *Front Mol Biosci*. **8**, 745649 (2001).

175. Luk, H. Y. *et al*. Sex-specific mitochondrial dynamics and mitophagy response to muscle damage. *Physiol Reps*. **10**(10), e15230 (2022).

176. Conlon, D. M., Welty, F. K., Reyes-Soffer, G., & Amengual, J. Sex-Specific Differences in Lipoprotein Production and Clearance. *Atheroscl Thromb Vasc Bio*. **43**(9), 1617–1625 (2023).

177. Bruell, J. H., Daroczy, A. F., & Hellerstein, H. K. Strain and sex differences in serum cholesterol levels of mice. *Science*. **135**(3508), 1071–1072 (1962).

178. Tran, T. *et al*. Male-Female Differences in the Effects of Age on Performance Measures Recorded for 23 Hours in Mice. *J Gerontol*. **76**(12), 2141–2146 (2021).

179. Heintz, M. M. *et al*. Age- and Diet-Dependent Changes in Hepatic Lipidomic Profiles of Phospholipids in Male Mice: Age Acceleration in Cyp2b-Null Mice. *J Lip*. **2022**, 7122738 (2022).

180. Casimiro, I., Stull, N. D., Tersey, S. A., & Mirmira, R. G. Phenotypic sexual dimorphism in response to dietary fat manipulation in C57BL/6J mice. *J Diab Compl.* **35**(2), 107795 (2021).

181. Yang, N. V. *et al*. TOMM40 and TOMM22 of the Translocase Outer Mitochondrial Membrane Complex rescue statin-impaired mitochondrial dynamics, morphology, and mitophagy in skeletal myotubes. Preprint at *bioRxiv : the preprint server for biology*, 2023.06.24.546411 (2023).

182. Griffett, K., & Burris, T. P. Development of LXR inverse agonists to treat MAFLD, NASH, and other metabolic diseases. *Front Med*. **10**, 1102469 (2023).

183. Ferencz, B. *et al*. The influence of APOE and TOMM40 polymorphisms on hippocampal volume and episodic memory in old age. *Front Hum Neurosci*. **7**, 198 (2013).

184. Chen, S. *et al*. TOMM40 genetic variants associated with healthy aging and longevity: a systematic review. *BMC Geriatr*. **22**(1), 667 (2022).

185. Chiba-Falek, O., Gottschalk, W. K., & Lutz, M. W. The effects of the TOMM40 poly-T alleles on Alzheimer's disease phenotypes. *Alzheim Dem*. **14**(5), 692–698 (2018).

186. Desai, M. S. *et al*. Bile acid excess induces cardiomyopathy and metabolic dysfunctions in the heart. *Hepatology*. **65**(1), 189–201 (2017).

187. Lebeau, P. F., Platko, K., Byun, J. H., & Austin, R. C. Calcium as a reliable marker for the quantitative assessment of endoplasmic reticulum stress in live cells. *JBC*. **296**, 100779 (2021).

188. Friedman, P. L., & Ellisman, M. H. Enhanced visualization of peripheral nerve and sensory receptors in the scanning electron microscope using cryofracture and osmium-thiocarbohydrazide-osmium impregnation. *J Neurocytol*. **10**(1), 111–131 (1981).

189. Willingham, M. C., & Rutherford, A. V. The use of osmium-thiocarbohydrazide-osmium (OTO) and ferrocyanide-reduced osmium methods to enhance membrane contrast and preservation in cultured cells. *J Histochem Cytochem*. **32**(4), 455–460 (1984).

190. Ewald, A. J. *et al*. Mammary collective cell migration involves transient loss of epithelial features and individual cell migration within the epithelium. *J Cell Sci*. **125**(11), 2638–2654 (2012).

191. McDonald, K. L., & Webb, R. I. Freeze substitution in 3 hours or less. *J Microscopy*. **243**(3), 227–233 (2011).

192. Giacomello, M., & Pellegrini, L. The coming of age of the mitochondria-ER contact: a matter of thickness. *Cell Death Differen*. **23**(9), 1417–1427 (2016).

193. Wieckowski, M. R. *et al*. Isolation of mitochondria-associated membranes and mitochondria from animal tissues and cells. *Nat Protoc*. **4**(11), 1582–1590 (2009).

194. Smith, G. A. *et al*. Cold shock domain-containing protein E1 is a posttranscriptional regulator of the LDL receptor. *Sci Transl Med*. **14**(662), eabj8670 (2022).

195. Chiu, S. *et al*. Comparison of the DASH (Dietary Approaches to Stop Hypertension) diet and a higher-fat DASH diet on blood pressure and lipids and lipoproteins: a randomized controlled trial. *Am J Clin Nutr*. **103**(2), 341–347 (2016).
196. Musunuru, K. *et al*. Ion mobility analysis of lipoprotein subfractions identifies three independent axes of cardiovascular risk. *Arterioscl Thromb Vasc Bio*. **29**(11), 1975–1980 (2009).
197. Caulfield, M. P. *et al*. Direct determination of lipoprotein particle sizes and concentrations by ion mobility analysis. *Clin Chem*. **54**(8), 1307–1316 (2008).
198. Su, W., Chi, Y. & Yu, A.A. Lipid droplets and mitochondria in metabolic disease. Front Physiol. **14**, 1266356 (2023).
199. Wang, W. *et al*. Atomic structure of human TOM core complex. *Cell Disc*. **6**, 67 (2020).
200. Mach, F. *et al*. Adverse effects of statin therapy: perception vs. the evidence – focus on glucose homeostasis, cognitive, renal and hepatic function, haemorrhagic stroke and cataract. *Eur Heart J*. **39**(27), 2526-39 (2018).